EVAPORATION RESIDUE CROSS SECTIONS MEASURED NEAR THE $N = 126$ SPHERICAL CLOSED SHELL IN ^{45}SC AND ^{44}CA-INDUCED REACTIONS

A Dissertation

by

TYLER ALLEN WERKE

Submitted to the Office of Graduate and Professional Studies of
Texas A&M University
in partial fulfillment of the requirements for the degree of

DOCTOR OF PHILOSOPHY

Chair of Committee,	Sherry J. Yennello
Co-Chair of Committee,	Charles M. Folden III
Committee Members,	Joseph B. Natowitz
	Gregory A. Christian
Head of Department,	Simon W. North

August 2016

Major Subject: Chemistry

ABSTRACT

Evaporation residue cross sections were measured for shell-stabilized nuclides near the $N = 126$ closed shell in ^{45}Sc- and ^{44}Ca-induced reactions on the lanthanide targets $^{156\text{-}158,\,160}$Gd, ^{159}Tb, and ^{162}Dy. The experiments were performed at the Texas A&M University Cyclotron Institute, with the K500 cyclotron providing the accelerated beam. The Momentum Achromat Recoil Separator was used to separate the desired evaporation residues from the other reactions products. The evaporation residue cross sections ranged between 2.7 mb and 1 μb for the reactions, and the effects of the shell stabilization and the relative neutron content of the compound nucleus on the cross sections were examined. The cross sections in the ^{45}Sc-induced reactions were up to four orders of magnitude smaller than ^{48}Ca-induced reactions on the same targets due to the relative neutron-deficiency of ^{45}Sc. This observation suggests that ^{45}Sc would be a poor projectile for synthesizing superheavy elements.

The experimental data were analyzed within the framework of a theoretical model aimed at elucidating the major physical factors which determined the evaporation residue cross sections. The model describes the fusion-evaporation reaction as a series of three independent steps: capture, compound nucleus formation, and deexcitation into the cold evaporation residue. The primary factor in determining the evaporation residue cross sections was found to be the difference between the fission barrier and the neutron separation energy. The nuclear level density in the model was modified to incorporate the collective motion of the nucleons. The influence of collective effects suggests that

cross sections for superheavy elements produced near the predicted $N = 184$ spherical closed shell may not be enhanced by the presence of the shell closure.

DEDICATION

For my wife Carrie

ACKNOWLEDGEMENTS

This dissertation would not be possible without the contributions of many truly wonderful people. Thank you to everyone who was involved in the project!

Firstly, I would like to thank my advisor, Prof. Cody Folden, for letting me join his research group in its early stages. I really enjoyed the hands-on experience I gained with detectors and electronics, and the beam times were a blast! Thank you for all your advice on scientific questions, paper writing, and my work-life goals.

I would also like to thank my committee members, Dr. Sherry Yennello, Dr. Joseph Natowitz, and Dr. Robert Tribble for their advice and feedback throughout my graduate career, especially on my preliminary exam and on my defense and dissertation. I also thank Dr. Gregory Christian for standing in on my defense committee on short notice.

I would like to thank my fellow graduate students for their encouragement and support, with special thanks to Dmitriy Mayorov. Dmitriy was always there to help run the experiments day and night and provided invaluable advice in interpreting the data. He knew the most about my experiments and was able to assist with whatever questions I had. Thank you Dmitriy! Thank you also to the other original graduate student of the Folden Group, Marisa Alfonso, for all your help during the experiments, for providing advice on life as a graduate student, and for keeping our group meetings lively and entertaining. Thank you also to Michael Frey, and undergraduate student who I had the pleasure of mentoring and who sat many shifts on the ^{45}Sc experiments. Finally, thank

you to Dr. Evgeny Tereshatov for sitting many shifts on my experiments and for setting a great example for our group with his professionalism and work ethic.

Thank you to the Cyclotron Institute Accelerator Group for providing stable beams intensities of the ^{45}Sc and ^{44}Ca projectiles used in the experiments and for working long hours into the night to meet our requests. We certainly had some troubles with the beams, and I thank you for your dedication to make our experiments run. Thank you also to the electrical shop and machine shop at the Cyclotron Institute for your help with making cables, fixing power supplies, and machining custom parts, typically on short notice.

Special thanks to our funding sources, the Department of Energy and the Welch Foundation for providing the grants for this research to occur. Thank you also to the Texas A&M College of Science and the Department of Chemistry for their support.

Finally, a huge, heartfelt thank you to my family and friends who helped me get through graduate school. Thank you especially to my wife Carrie for her constant love and encouragement! You helped me keep my sanity, talked with me through long nights, and supported me though all the good times and the bad times. I could not have done this without you!

NOMENCLATURE

ADC	Analog-to-Digital Converter
CELD	Collective Enhancement to the (Nuclear) Level Density
CFD	Constant Fraction Discriminator
CN	Compound Nucleus / Compound Nuclei
CoT	Center of Target
DAQ	Data Acquisition
DC	Detector Chamber
ECR	Electron Cyclotron Resonance (Ion Source)
EvR	Evaporation Residue
FC	Faraday Cup
FWHM	Full-Width at Half Maximum
GF3	A 1-D Peak Fitting Program
GSI	GSI Helmholtzzentrum für Schwerionenforschung (Germany)
LISE++	A Fragment Separator Simulation Program
MARS	Momentum Achromat Recoil Separator
MCP	Microchannel Plate (Detector)
NIM	Nuclear Instrumentation Standard
NLD	Nuclear Level Density
PEEK	PolyEther Ether Ketone
PSSD	Position-Sensitive Silicon Detector

ROI	Region of Interest
SEMF	Semi-Empirical Mass Formula
SHE	Superheavy Element
TAC	Time-to-Amplitude Converter
TC	Target Chamber

TABLE OF CONTENTS

Page

LIST OF FIGURES

Page

LIST OF TABLES

Page

1. INTRODUCTION

This dissertation is primarily concerned with the experimental studies of complete fusion-evaporation reactions and the study of the reaction mechanism within the framework of a theoretical model. The fusion of two nuclei and subsequent decay of the excited compound nucleus into the ground state of the final product has been the primary method for synthesizing new superheavy elements (SHEs, elements with 104 protons or more in the nucleus, also called transactinides). Additionally, this type of reaction has been used to study astrophysical processes [1], fission processes [2, 3], nuclear structure properties [4, 5], and to produce radioactive isotopes for medical treatments [6] or for chemistry studies [7]. The fusion of an accelerated projectile with an enriched target has been used to discover the 18 heaviest known elements, starting with the bombardment of einsteinium (Z = 99) with helium nuclei (Z = 2) to make mendelevium (Z = 101) [8]. The current heaviest element on the periodic table has 118 protons and was created through the bombardment of ^{249}Cf (Z = 98) with ^{48}Ca (Z = 20) [9]. In fact, all of the transactinide elements are man-made via some type of nuclear reaction at a particle accelerator.

Fig. 1.1 shows the superheavy region of the chart of the nuclides and the reactions which first produced those elements. Although great progress has been made in the synthesis of new SHEs, the production of SHE is still quite challenging task; cross sections for the production of the heaviest SHEs on the order of a single picobarn [10].

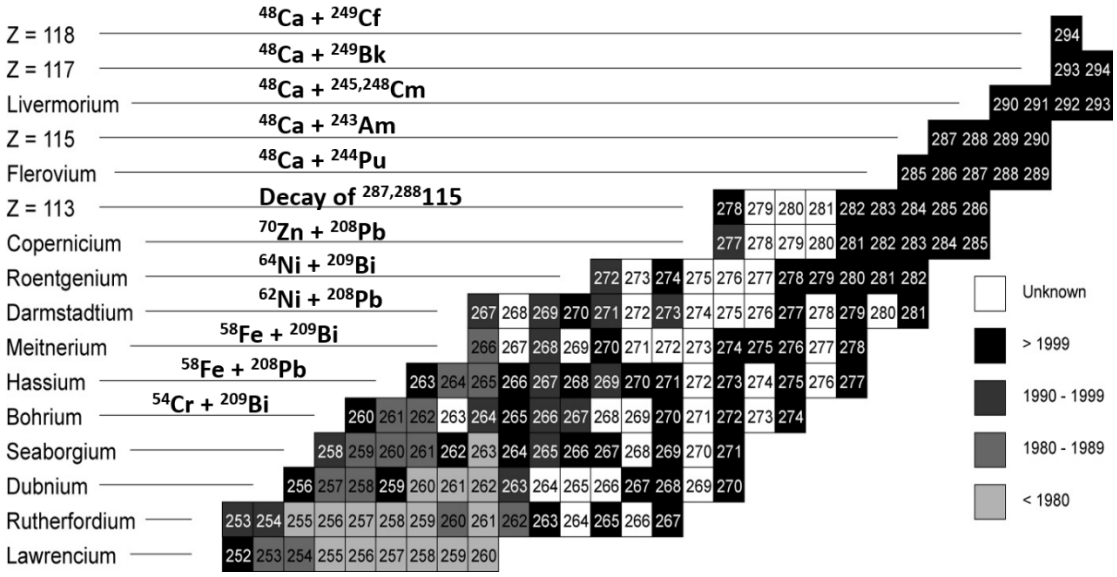

Figure 1.1. Superheavy region of the chart of the nuclides. The associated reaction used to discover each SHE is given for every element with starting with Bh (Z = 107). The legend denotes in which decade each isotope was discovered. Figure reproduced from [11] © IOP Publishing. Reproduced with permission. All rights reserved.

Even with the large beam intensities of stable isotopes that are now available at modern accelerator facilities, the tiny cross sections mean that the experiments to produce the heaviest SHEs require extremely long beam irradiations. For example, the reaction of ^{70}Zr + ^{209}Bi to produce element 113 was studied using 553 days of beam time at the RIKEN Linear Accelerator Facility in Japan, and only 3 decay chains were observed [12, 13]! Therefore, it was desirable to study a series of reactions which produce compound nuclei (CN) with similar physical properties to SHEs, but have much larger production cross sections so that more data can be collected in a shorter time span. The work presented in this dissertation focuses on compound nuclei produced in hot fusion-evaporation reactions using ^{45}Sc and ^{44}Ca projectiles. The studied CN were near

to the N = 126 spherical closed shell; these reactions were chosen to serve as an analog for SHEs, which are produced near the predicted N = 184 spherical closed shell.

1.1 A Brief History of Heavy and Superheavy Elements

The modern version of the periodic table of the elements took its final shape in the 1940's and 1950's after American chemist Glenn Seaborg hypothesized that the actinide elements belonged in their own separate row below the lanthanide elements. The modern periodic table as of March 2016 is shown in Fig. 1.2. Radioactivity was first discovered in 1896, and by the 1950's, the radioactive elements Tc (Z = 43) and Pm (Z = 61) had been placed on the periodic table in the main body and lanthanide series, respectively. The heaviest element with any stable isotopes is Po (Z = 82), and every isotope of every element starting with Bi (Z = 83) is radioactive. Some of these isotopes are extremely long-lived (e.g. ^{238}U, $t_{1/2}$ = 4.468 x 10^9 years, almost as long as the Earth has existed), and elements as heavy as Pu (Z = 94) can be found in nature [14]. Artificial methods are required to produce an element heavier than Pu, and the most straightforward way to produce a heavier element is to bombard an element such as Pu with neutrons and allow the neutron-rich isotopes to β^- decay into a nucleus with a higher atomic number. Such a process occurs in a nuclear reactor and can produce elements as heavy as Fm (Z = 100) [15]; however, Fm is the heaviest element able to be produced in this method. To circumvent this problem, He nuclei (Z = 2, also called α particles) were accelerated to high enough energies that they could fuse together with Es

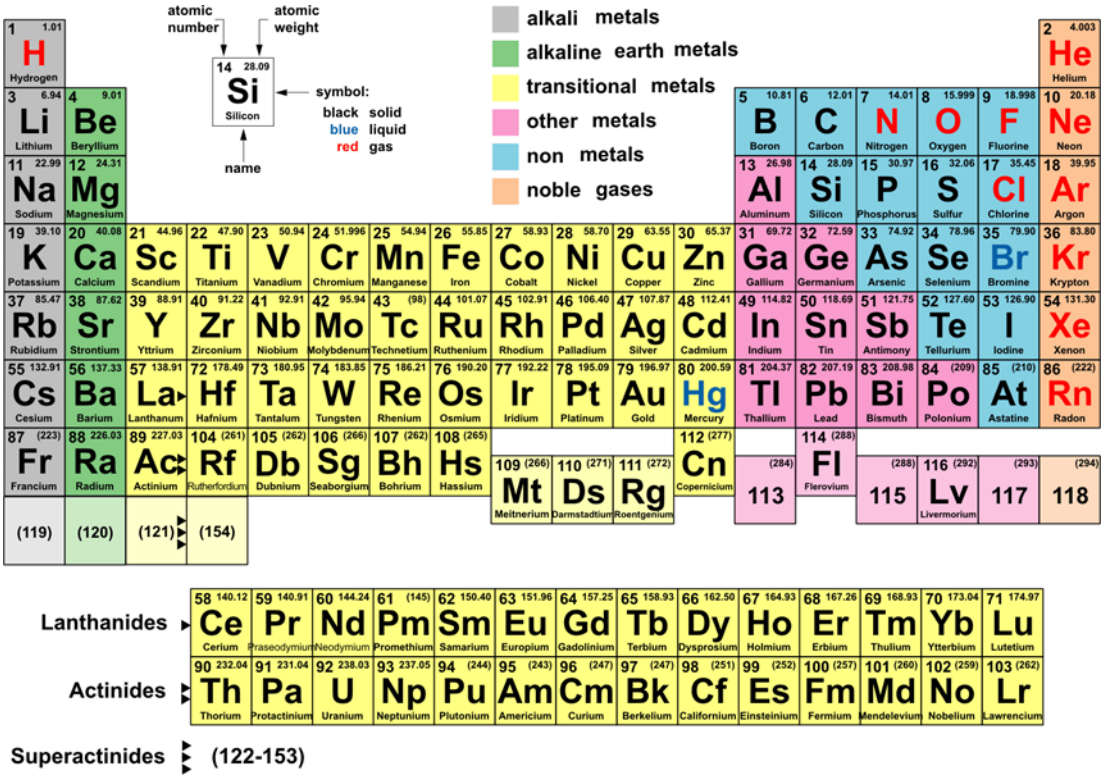

Figure 1.2. The periodic table as of March 2016. All elements heavier than Pu are not naturally occurring and must be synthesized in a nuclear reaction. Figure adapted from [17].

(Z = 99) nuclei to produce Md (Z = 101). As beam intensities and experimental technology (such as the invention of the gas-filled separator) improved, better experimental sensitivities were attained, and even heavy nuclei such as ^{70}Zn were used as projectiles in fusion reactions to make superheavy elements [16].

Two notable campaigns have produced SHEs over the course of the last 40 years. The first campaign produced elements with Z = 107-112 in "cold fusion" reactions, a name which reflects the relatively small excitation energies of the CN (~10-20 MeV). These SHEs were discovered at the GSI Helmholtzzentrum für Schwerionenforschung

(GSI) in Darmstadt, Germany using the Separator for Heavy-Ion Reaction Products. The defining features of these reactions were that the projectiles had an energy near to or below the Coulomb barrier, and the target was either ^{208}Pb (Z = 82) or ^{209}Bi (Z = 83) (both of these nuclides are on the N = 126 closed shell). Projectiles of ^{54}Cr (Z = 24), ^{58}Fe (Z = 26), ^{62}Ni, ^{64}Ni (Z = 28), and ^{70}Zn (Z = 30) were used to produce these SHE's. The results from these cold fusion reactions are summarized in Refs. [18] and [19]. As a result of the low bombarding energies and very negative Q-values (a quantity that describes the mass difference between the reactants and products), typically only 1 or 2 neutrons were emitted from the CN. The production cross sections for these SHEs ranged from 530 pb for the production of Bh (Z = 107) [19] to 0.22 pb for the production of Z = 113 [16]. The *barn*, b, is the standard unit for reporting cross sections. For reference, 1 b is approximately the size of the cross-sectional area of a U (Z = 92) nucleus (1 b = 10^{-28} m^2 = 10^{-24} cm^2, 1 mb = 10^{-27} cm^2). As shown on the left-hand side of Fig. 1.3, there is a sharp decrease in the cold fusion cross sections as the atomic number increases due to an increasing repulsion in the projectile-target system. The cold fusion reactions also lead to extremely neutron-deficient compound nuclei, and the probability that the system survives against fission is extremely small.

In response to the sharply decreasing cross sections in the cold fusion reactions, the heavy elements group at the Joint Institute for Nuclear Research (JINR) in Dubna, Russia bombarded actinide targets with ^{48}Ca (Z = 20) projectiles to successfully synthesize elements 113-118 [20]. The ^{48}Ca projectiles were accelerated to energies above the Coulomb barrier for the reactions, and the CN commonly had excitation

energies of ~30-50 MeV. As such, these reactions were dubbed “hot fusion” reactions. These hot fusion reactions used in SHE synthesis exhibit a smaller Coulomb repulsion between the projectile and target than the cold fusion reactions and somewhat alleviate the problem of the sharply decreasing cross sections. The CN typically emitted 3-5 neutrons in these reactions, and the typical cross sections were relatively constant at approximately 1 pb, as shown in the right-hand side of Fig. 1.3. Due to the large neutron excess of ^{48}Ca, the CN produced in these hot fusion reactions were closer to the line of β-stability than those produced in the cold fusion reactions.

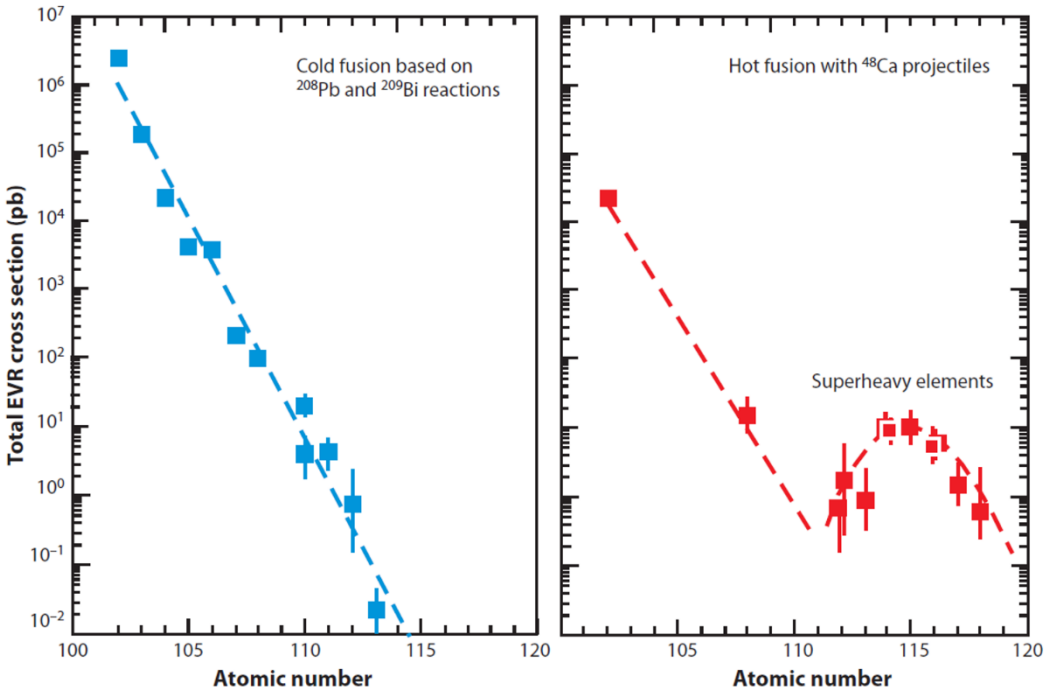

Figure 1.3. Comparison of maximum cross sections for heavy and superheavy elements produced in a) cold fusion and b) hot fusion reactions. The cold fusion cross sections decrease exponentially with increasing atomic number due to the rapid increase of the Coulomb repulsion between projectile and target. The hot fusion reaction cross sections are relatively constant for the production of Z = 112-118. Figure used with permission from [10].

The study of heavy and superheavy elements have both physical and chemical importance. Physical studies reveal the limits of nuclear stability and the properties of the heavy and superheavy elements, such as the half-life, decay properties, particle separation energies, shape and structure properties, and production cross sections, just to name a few. These studies lead to a better understanding of the chart of the nuclides and the various reaction mechanisms which produce these nuclei. While this work does not discuss the chemical properties of heavy and superheavy elements as much as the physical properties, the importance of doing chemical studies on the elements still should be mentioned. Chemical studies of SHEs reveal information about the periodicity of the elements, electronic structures, and the stability of compounds containing SHEs, amongst other properties. Several notable chemical experiments have been done on SHEs. The enthalpy of adsorption of Cn (Z = 112) [21] and Fl (Z = 114) [22] have been measured in experiments using gold-plated Si detectors with an applied temperature gradient. The chemical properties of Sg (Z = 106) have been explored by complexing it with carbon monoxide to form $Sg(CO)_6$ [23]. However, experimental data on the chemistry of SHEs are generally sparse, and most of the knowledge on the chemical properties of SHEs come from theoretical predictions. An excellent, comprehensive review can be found in [24].

1.2 The Fusion-Evaporation Reaction

The type of nuclear reaction that was used to produce SHEs and that was studied in this work is called a fusion-evaporation reaction, and a simplified schematic of the reaction is presented in Fig. 1.4. In a typical fusion-evaporation reaction, an accelerated projectile bombards a stationary target with an energy that is comparable to the Coulomb repulsion between the two nuclei (the "Coulomb barrier"). The projectile is typically a

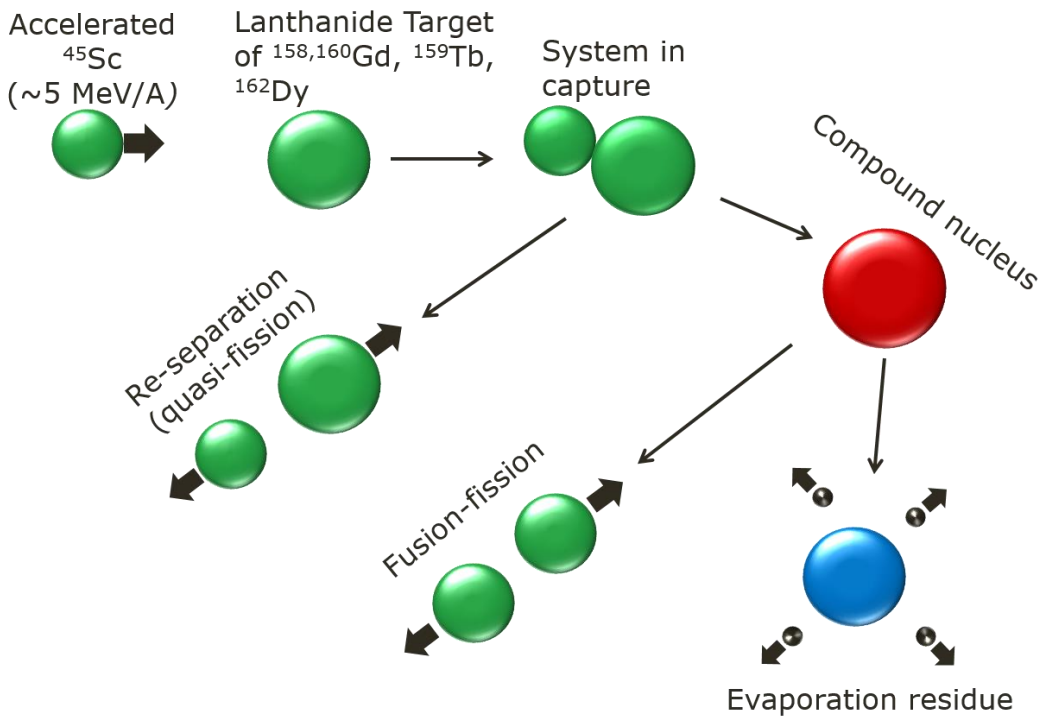

Figure 1.4. Schematic of the fusion-evaporation reaction. The projectile is captured by the target in a collision that imparts angular momentum into the system in capture and eventually the compound nucleus (CN, represented by the large red sphere). The system in capture can either form the CN or re-separate into two fragments (this is called quasifission). Once the CN is formed, it can decay by fission (this is called fusion-fission) or by evaporating particles (small black spheres) such as neutron or protons to form the cold evaporation residue (large blue sphere).

stable isotope that has been isotopically enriched, such as ^{48}Ca. Facilities such as ReA3 at the National Superconducting Cyclotron Laboratory at Michigan State University [25] can produce radioactive isotope beams, but the beam intensities of radioactive beams are still many orders of magnitude smaller than the beam intensities of stable beams. The target is also typically an enriched isotope and can be either stable or radioactive. In the hot fusion campaign to synthesize elements 113-118, for example, radioactive actinide targets such as ^{245}Cm and ^{249}Cf were employed [9]. In this work, all the targets were stable isotopes.

In a fusion-evaporation reaction, the protons and neutrons of the projectile nucleus mix together with the protons and neutron of the target nucleus and then equilibrate, forming an excited compound nucleus; this is the "fusion" stage. This CN then deexcites by the emission of neutrons, protons, α particles, and ultimately γ rays until the system reaches the ground state of the final evaporation residue (EvR); this is the "evaporation" stage.

The fusion stage of the process involves the projectile and target overcoming the Coulomb barrier and forming the di-nuclear system in a "touching spheres" configuration (see Fig. 1.4). This is known as the "system in capture" and is described by the capture cross section, σ_{capt}. The system in capture then undergoes shape and energy equilibration as the individual nucleons collide with each other and thermalize. It is possible at this stage that the system re-separates into a projectile-like fragment and a target-like fragment. This process is known as 'quasifission', and it hinders the formation of the CN. The excited CN is formed with probability P_{CN}, and $P_{CN} \leq 1$ due to

the presence of quasifission. The capture process is relatively well-understood, and σ_{capt} can be calculated with a code such as CCFULL [26] or a semi-empirical formula [27]. The stage of the compound nucleus formation, however, is the least well understood and least precise term in Eq. (1.1), and the uncertainty associated with P_{CN} can be up to one order of magnitude [28]. Fig. 1.5 shows various model calculations which reproduce EvR cross sections in cold fusion reactions. Within the models, the variance of P_{CN} is two orders of magnitude.

The probability of the CN deexciting via particle and γ ray emission to reach the final evaporation residue is described by the survival probability W_{sur}. During the early stages of the deexcitation process, the excitation energy of the CN is above the fission threshold, and there is a significant probability that the CN fissions into two fragments. This process is known as "fusion-fission", and $W_{sur} \leq 1$ due to the presence of fusion-fission. Due to the large level density of the CN (30-60 MeV of excitation energy distributed among ~200 nucleons), the deexcitation of the compound nucleus can be described within the framework of a statistical model. The statistical treatment of the decay of the CN is relatively well understood, and the uncertainty on W_{sur} is approximately a factor of 3. To determine the overall EvR production cross section, the three quantities which represent the three independent stage of EvR formation are multiplied together as such:

$$\sigma_{EvR} = \sigma_{capt} P_{CN} W_{sur} \ . \qquad (1.1)$$

Full details of the model calculations performed in this work, as well as more discussion on all three factors in Eq. (1.1), are presented in Section 3 of this dissertation.

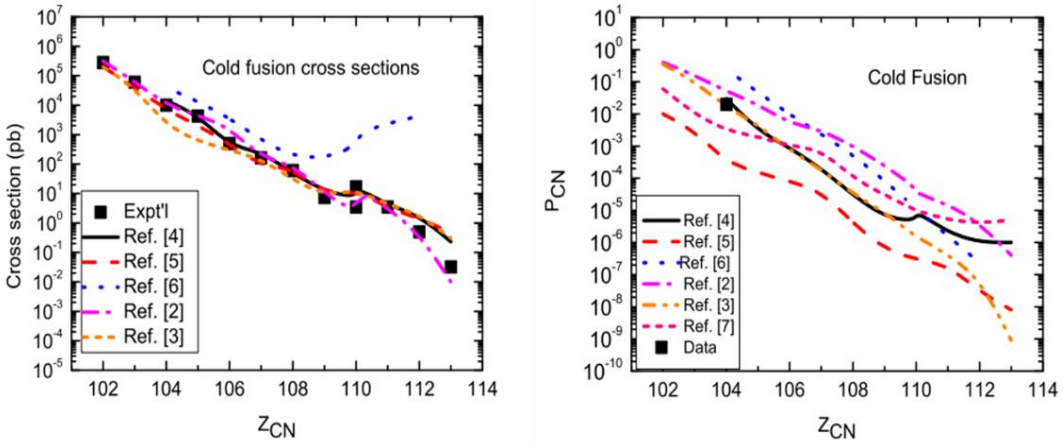

Figure 1.5. Model calculations for P_{CN} in cold fusion reactions. Various models have been able to calculate EvR cross sections with good accuracy, as shown in the left-hand panel, but the calculations of P_{CN} within these models (right-hand panel) can vary by as much as two orders of magnitude. Figure reproduced from [28] under Creative Commons license BY-NC-SA, available at [LINK].

1.3 Nucleon Shell Closures

The nucleon shell closures are known to increase the binding energy of nuclides on or near the closed shells, making them more stable against radioactive decay. For example, the doubly magic nuclide ^{132}Sn (Z = 50, N = 82) has a half-life of 39.7 ± 0.8 s [29], even though it is very far from any stable nuclides and many surrounding nuclides have half-lives of < 1 s. The nucleon shell closures have a variety of other important consequences for nuclear reactions and nuclear structure. In the context of this dissertation, the most important consequence of the nuclear shell closures is that the shell correction increases the fission barrier for a given nuclide, thus making the CN more likely to decay via emission of particles instead of fission (this is the desired result

when trying to produce heavy elements). Calculations using the liquid drop model of the nucleus *without* shell effects have suggested that nuclei with $Z \geq 104$ (Rf) would have spontaneous fission half-lives of $\leq 10^{-14}$ s (see [30] and references therein). Indeed, the existence of SHEs is made possible through shell effects!

1.3.1 The Liquid Drop Model of the Nucleus

The study of nuclear properties, such as nuclear decay (half-lives, decay energies, decay modes) and nuclear reactions (excitation energies, cross sections), depend strongly on the masses of the reactants and products. An argument could be made that knowledge the mass of a nucleus is the most important piece of information to understand its decay properties. Therefore, many models exist to calculate the masses of various nuclides, and the nuclear mass is still an active area of research today. Until the end of the 1940s, the liquid drop model was the most successful model for calculating the properties of a given nucleus. By approximating the nucleus using the forces typically found in a droplet of liquid, this model was able to accurately predict the nuclear binding energy, and therefore many other properties, for many nuclei. The German physicist Carl Friedrich von Weizsäcker proposed a "semi-empirical mass formula" (SEMF) to predict the binding energy and other nuclear properties [31]. A modern version of the SEMF is given in Eq.(1.2):

$$B_{tot}(N,Z) = a_v A - a_s A^{2/3} - a_c \frac{Z^2}{A^{1/3}} - a_a \frac{(N-Z)^2}{A} + \Delta(N,Z). \qquad (1.2)$$

In Eq. (1.2), a_v is the volume term which represents the attractive nuclear force between nucleons, a_s is the surface energy term which accounts for the reduced binding for nucleons on the edge of the nucleus, and a_c is the Coulomb term which accounts for the repulsion between protons in the nucleus. The a_a term accounts for the de-stabilization of the nucleus due to the difference between the number of protons and neutrons in a given nucleus; the a_a term is zero when $N = Z$. The fifth term describes the energy due to the pairing of protons with protons and neutrons with neutrons. Each nuclear orbital can hold two nucleons, and the lowest energy configuration (most bound) is obtained when the highest energy proton and neutron shells are filled. The highest energy configuration occurs when the valence orbitals for both protons and neutrons are unpaired. The pairing energy is commonly calculated as [32]:

$$\Delta(N,Z) = \begin{cases} 22 \text{ MeV} / \sqrt{A} & , \text{ even-even} \\ 11 \text{ MeV} / \sqrt{A} & , \text{ even-odd or odd-even} \\ 0 & , \text{ odd-odd} \end{cases}. \tag{1.3}$$

The values for the five physical parameters in Eq. (1.2) are determined by fitting to experimental data, and the effect of each parameter on the binding energy is depicted in Fig. 1.6. Once the binding energy of a nucleus has been calculated, the mass of the nucleus can be calculated using Eq. (1.4)

$$M = N(m_n) + Z(m_p) - B_{tot}(N,Z)/c^2. \tag{1.4}$$

In Eq. (1.4), N and Z are the number of protons and neutrons, respectively, while m_n and m_p are the neutron and proton mass, respectively.

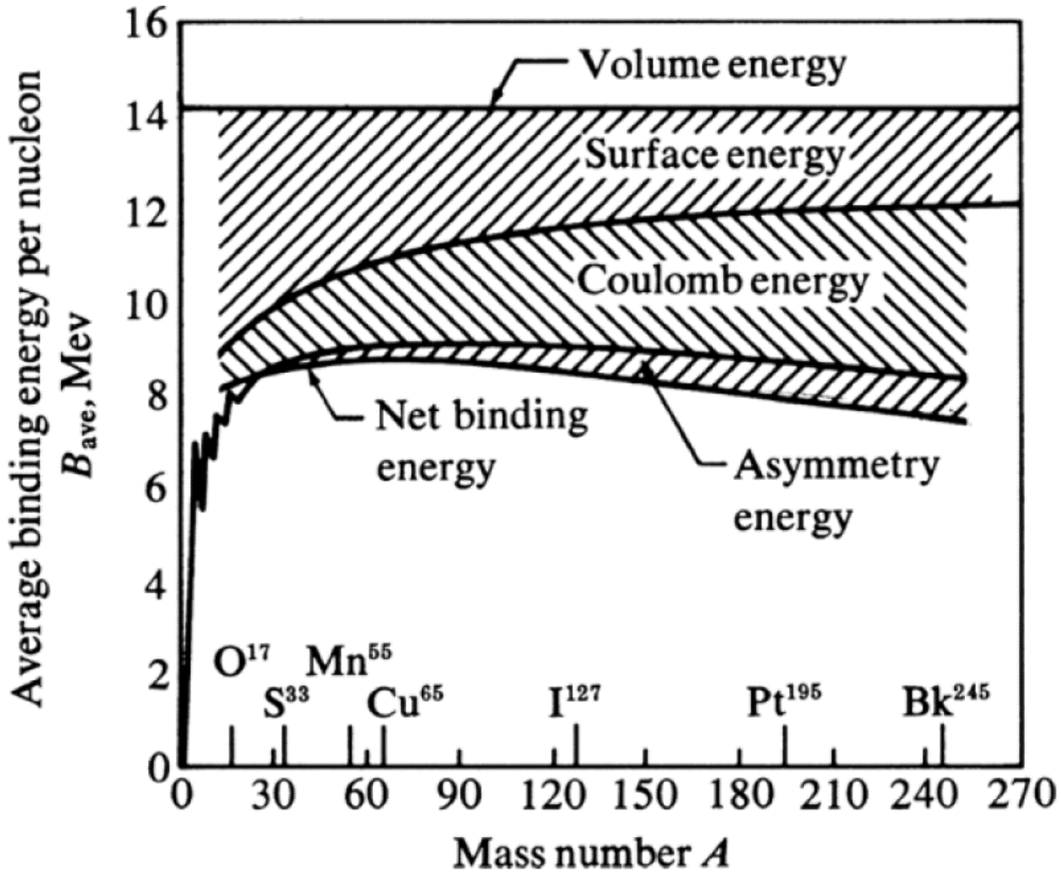

Figure 1.6. Effects of the five parameters in the SEMF on the average binding energy per nucleon. The volume term is attractive and grows linearly with *A*. The other terms are repulsive and lower the binding energy. The effect of nucleon pairing is qualitatively shown by the zig-zag on the left side of the plot. Figure reproduced with permission from [32] © 2006 John Wiley & Sons, Inc.

1.3.2 The Shell Model

The SEMF does well in predicting the masses and binding energies of most nuclides; however, there are notable trends of significant deviations where the SEMF does not agree with the experimental values. This phenomenon is depicted in Fig. 1.7. These regions where the SEMF diverges from the experimental data are centered on the "shell closures", where the shell effect is the strongest. These nucleon shell closures are analogous to the shell closures for atomic electrons, which give rise to the noble gas elements and lead to enhanced stability for these atoms. The strongest shell closures for nucleons occur for both neutrons and protons at 2, 8, 20, 28, 50, and 82 nucleons. A neutron shell closure is also known at $N = 126$. The nuclides on and near these shells generally have a spherical shape; however, in recent years it was discovered that there also exist nucleon shell closures where the nucleons on and near the shell are deformed (for example, the shell closure at $Z = 108$, $N = 162$ [33]). If a nuclide is on either a neutron or proton closed shell, it is often referred to as a "singly magic" nucleus (e.g. ^{44}Ca, $Z = 20$, $N = 24$). If a nuclide is on both a proton and neutron closed shell, it is often referred to as a "doubly magic" nucleus (e.g. ^{48}Ca, $Z = 20$, $N = 28$).

When the liquid drop model of the nucleus failed to account for the experimental observations of nuclear shells, a new approach was needed. After various models failed to reproduce the correct location of the closed shells, the physicist Maria Göppert Mayer coupled the nucleon spin to its motion within a modified square well nuclear potential and published her breakthrough work in 1950 [34, 35]. Mayer's work accurately

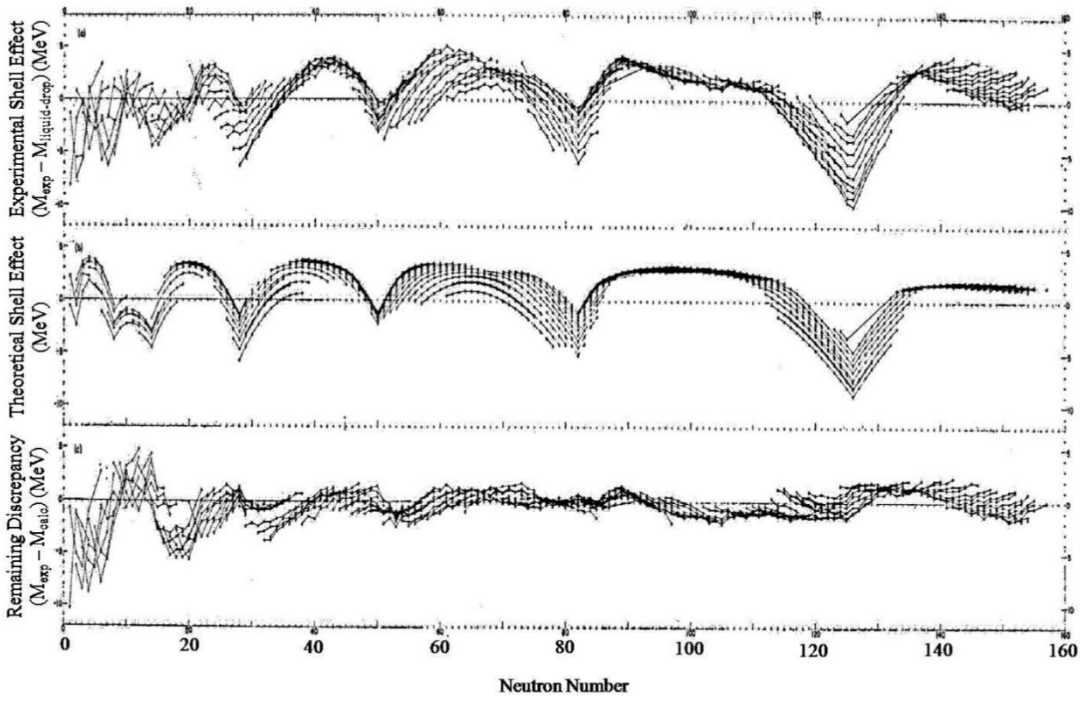

Figure 1.7. Evidence for shell effects as a function of the neutron number. Top: Difference in experimental masses and liquid-drop model calculations. Middle: Theoretical calculations for shell effects. Bottom: Difference in the experimental masses and the theoretical calculations. Figure used with permission from [37].

reproduced the spherical closed shells, but work was still left to be done. The Swedish physicist Sven Gösta Nilsson extended the shell model to deformed nuclei by using a deformed nuclear potential and considering all of the single-particle energy levels within a nucleus [36].

The basic formulation of the shell model does not account for the stabilizing effects for nuclides *near* the closed shells. The corrections that need to be made to correctly account for the increased stability for nuclides which are near (and also directly on) the closed shells are appropriately called “shell corrections.” Strutinsky was the first to demonstrate that the shell correction could be determined by calculating the energies

of all of the single-particle states [38, 39]. The nuclear shells occur in the regions where there are the fewest single particle levels; in other words, the closed shells reduce the level density of the nuclei on and near them. The magnitude of the shell correction (the "shell correction energy", denoted by the symbol Δ_{shell}) can be calculated by subtracting the single-particle energy of a continuous distribution of states from the sum of the single-particle energies of a discrete distribution as such:

$$\Delta_{shell} = U(\beta) - \tilde{U}(\beta) \ , \tag{1.5}$$

where the parameter β describes the shape of the nucleus. The quantity $U(\beta)$ represents the single particle energy of a nucleus and can be calculated by summing the single-particle energies E_i for i discrete levels at a given deformation β:

$$U(\beta) = \sum_i 2E_i n_i \ . \tag{1.6}$$

The quantity n_i is the "occupation number" of a given state i; $n_i = 1$ if the state is populated, and $n_i = 0$ if the state is not populated. The $\tilde{U}(\beta)$ term in Eq. (1.5) represents the energy of a "non-shell-stabilized" nucleus and can be calculated by summing of all the energy states in a nucleus with a "uniform distribution of energy states":

$$\tilde{U}(\beta) = 2\int_{-\infty}^{\lambda} Eg(E)dE \ . \tag{1.7}$$

In Eq. (1.7) – the "non-shell-stabilized" nucleus – the discrete level density is replaced by the uniform level density function $g(E)$, and λ is the Fermi energy of the system. In a system with N particles, λ can be calculated by solving the following expression:

$$N = 2\int_{-\infty}^{\lambda} g(E)dE\,. \tag{1.8}$$

The factor of 2 in front of the above equations represents the number of particles that can occupy each degenerate energy level. To model the non-zero widths of the energy states, Strutinsky introduced the level density function shown in Eq. (1.9) below. In this equation, *g(E)* is calculated as a sum of Gaussian-shaped states, where each state is centered on its energy E_i.

$$g(E) = \frac{1}{\gamma\sqrt{\pi}}\sum_i \exp[-(E-E_i)^2/\gamma^2]\,. \tag{1.9}$$

The parameter γ defines the width of the energy range for which the continuous distribution is calculated. Once the appropriate energy states and the deformation are known, the shell correction energy can be calculated from Eq. (1.5)

Once the shell correction energy has been calculated, it can be used to modify the height of the fission barrier. A large table with predicted shell corrections for thousands of nuclides can be found in [40]. These are the shell corrections which will be used in this work. When considering Eq. (1.5), a negative value of Δ_{shell} represents a stabilization of the nucleus and would result in a larger fission barrier. As the excitation energy of a nucleus increases, the level density increases and levels overlap. As such, the shell correction energy is "washed-out" at higher excitation energies. The influence of shell effects on the fission barrier and their "wash-out" are fully discussed in Section 3 of this dissertation.

1.4 Survey of Previous Research

Although the understanding of the fusion-evaporation reaction came together when the compound nucleus was proposed as an intermediate stage by Niels Bohr in 1936 [41], there is still much debate about the influential factors which determine EvR cross sections. The fusion-evaporation reaction is still a commonly-used tool in experimental nuclear physics and chemistry, and different experiments have been aimed at studying the three steps of the reaction. The fusion process and σ_{capt} is still being investigated with stable and radioactive ion beams at energies near and below the Coulomb barrier ([42-44] and references therein). Several research groups are trying to better understand and quantify P_{CN} primarily by measuring mass distributions, angular distributions, or mass-angle distributions of fragments from quasifission (e.g. see [45] or [46] and references therein). Attempts to quantify W_{sur} have been focused on measuring the probability of emitting the first neutron from the excited CN [47]. Although many fascinating literature data exist on fusion-evaporation reactions, a few selected topics which have the most relevance to the reactions studied in this dissertation are presented below.

1.4.1 Fusion-Evaporation Reactions near the N = 126 shell

In this work, EvR cross sections were measured in ^{45}Sc- and ^{44}Ca-induced reactions that produced CN near the N = 126 spherical closed shell. One of the first

works that investigated the magnitudes of heavy-ion EvR cross sections near the $N = 126$ spherical closed shell was published in 1984 by Vermeulen *et al.* [48]. In this work, ^{40}Ar projectiles bombarded isotopes of Ho, Tm, Yb, Lu, Hf, and Ta to produce CN with $Z =$ 85-91 near and on the $N = 126$ spherical closed shell. The same research group published another paper in 1985 [49] which studied ^{48}Ca-, ^{86}Kr-, and ^{124}Sn-induced reactions to make CN which again were on and near the $N = 126$ spherical closed shell. The major results are presented in Fig. 1.8, which shows the cross-sectional data compared to standard statistical model calculations with and without shell effects. At the $N = 126$ spherical shell closure, the model calculations with shell effects grossly over-predicted the data, which was a rather surprising result. In the statistical model of the deexcitation of the excited CN, a larger total fission barrier means that fission is inhibited and particle emission is favored, which leads to larger EvR cross sections. As discussed in Section 1.3, a larger shell correction results in a larger total fission barrier. Thus, the $N = 126$ shell closure was expected to inhibit fission and promote particle emission for the excited EvRs studied in these works. However, no cross section enhancement was observed in the data. It was also shown that the influence of the shell effects on the nuclear level density faded out at surprisingly low excitation energies for these reactions.

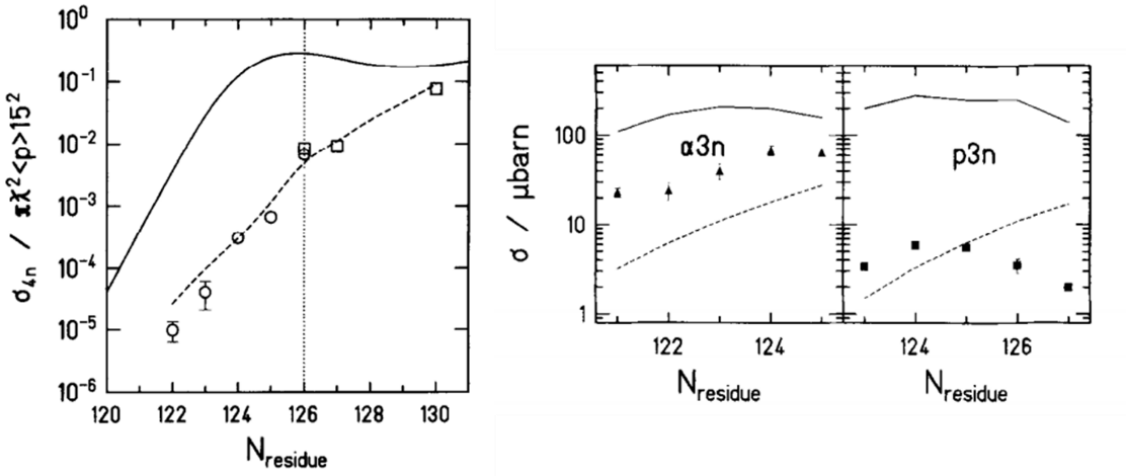

Figure 1.8. EvR cross sections near the N = 126 closed shell. Left: Reduced cross sections for heavy-ion-induced reactions to produce CN near the N = 126 spherical closed shell. The open symbols are experimental data points, the solid line is a standard fusion-evaporation calculation with shell effects, and the dashed line is a calculation without shell effects. The factor of $\left(1/\pi\lambda\!\!\!^{-2} < p > 15^2\right)$ makes the ordinate approximately equal to the survival probability times the transmission coefficient of the fusion barrier. Right: Maximum cross sections for selected EvR channels in the reactions in ^{40}Ar-induced reactions on various Yb targets. The left-hand figure was used with permission from [49], and the right-hand figure was used with permission from [48].

Other studies of fusion-evaporation reaction near the N = 126 shell have shown the importance of the relative values of the fission barrier, B_f, and neutron separation energies, S_n, of the CN in determining the EvR cross sections. The recent work of Mayorov *et al.* studied ^{48}Ca-, ^{50}Ti- and ^{54}Cr-induced reactions on lanthanide targets to produce CN with Z = 84-90 [50, 51]. As the projectiles increased in atomic number, the relative neutron-richness of the CN decreased; the less neutron-rich CN lead to smaller values of B_f and larger values of S_n, both of which are detrimental to the survival probability. A plot of the maximum *4n* (or *4n + 5n*, if the EvRs were not uniquely identifiable) cross sections against the average difference in B_f and S_n across the

deexcitation cascade is presented in Fig. 1.9. The quantity $\overline{B_f - S_n}$ represents the average difference in B_f and S_n across the deexcitation cascade. As $\overline{B_f - S_n}$ goes to zero, the maximum 4*n* cross sections decrease by many orders of magnitude.

Additional investigations into EvR cross sections with very neutron-deficient systems were done by Andreyev *et al.* Their work studied the production of many neutron-deficient isotopes of Bi, Po, At, and Ra which are north and west of the $N = 126$

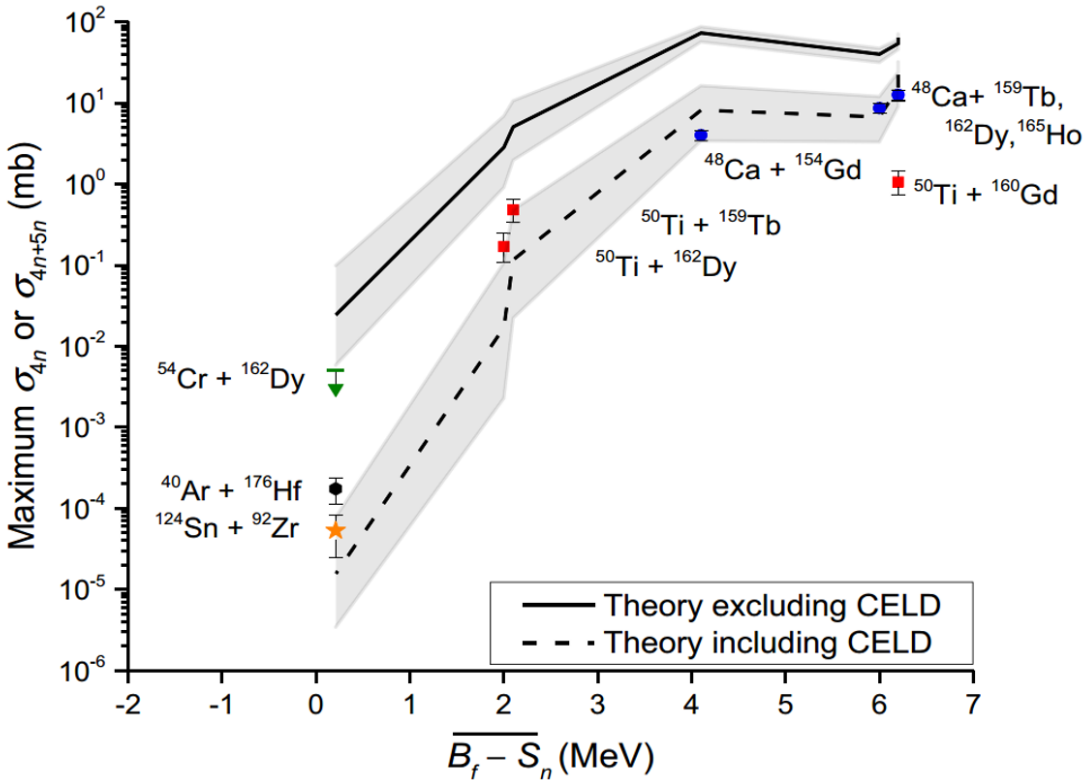

Figure 1.9. Maximum 4n cross sections in ^{48}Ca-, ^{50}Ti-, and ^{54}Cr-induced reactions as a function of $\overline{B_f - S_n}$. Note the rapid decrease in $\sigma_{4n,\,max}$ as $\overline{B_f - S_n}$ decreases. The dashed lines represent the results of the theoretical model described in [50]. The gray band around the dashed line shows the effect of changing the fission barrier by ±0.5 MeV. This will be fully discussed in Section 4.4.3. Figure used with permission from [51].

on the chart of the nuclides [52-54]. The data were analyzed using common fusion-evaporation codes such as HIVAP [55, 56] and ALICE [57], and it was found that the liquid-drop component of the fission barrier had to be reduced by an empirical scaling factor (≈30-35%) for the calculations to reproduce the data. These results implied that the experimental fission barriers were much smaller than the theoretically predicted ones for these neutron-deficient nuclei. Additionally, Andreev *et. al.* studied the ^{40}Ca + ^{159}Tb reaction [54]; it will be useful to compare this reaction to the ^{48}Ca, ^{50}Ti + ^{159}Tb reactions studied by Mayorov *et. al*, and the ^{44}Ca, ^{45}Sc + ^{159}Tb reactions which are studied in this dissertation. A comparison of the ^{40}Ca- and ^{48}Ca-induced reactions is presented in Fig. 1.10. Many of the reactions studied in this work are aimed at studying changes in the EvR cross sections as neutron number of the target changes. Additionally, the effects of changing the projectile were examined by studying the EvR cross sections of different projectiles on the same targets as has been done in these previous works.

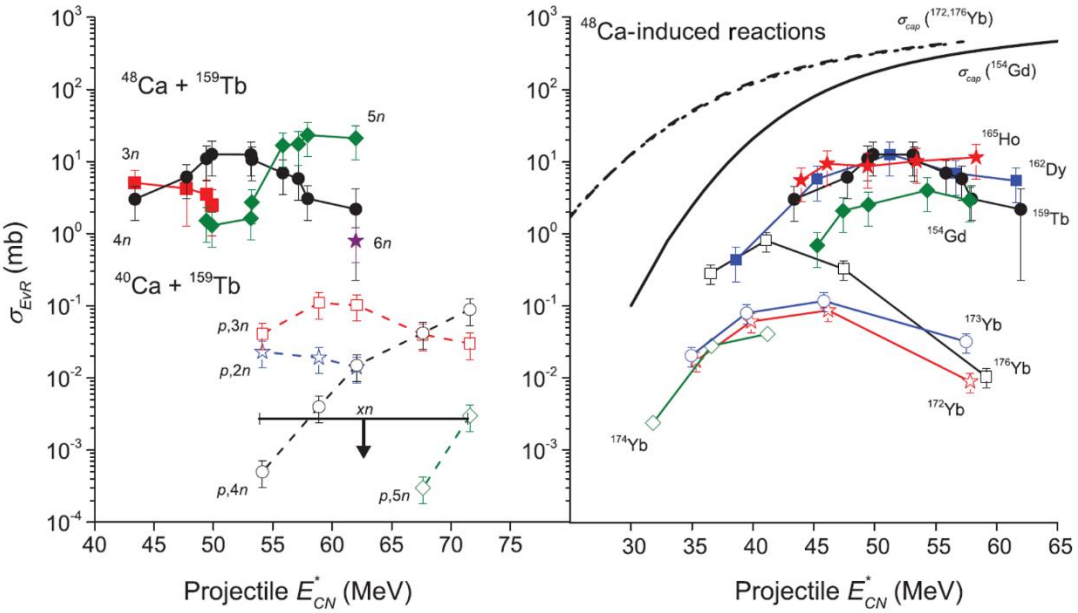

Figure 1.10. Data showing the effects of the neutron-richness of the reaction system on the EvR cross sections. Left: Comparison of the ^{48}Ca + ^{159}Tb reaction [50] (solid points and lines) and the ^{40}Ca + ^{159}Tb reaction [54] (Open points and dashed lines). The exit channels are denoted for each reaction. The arrow denotes the upper limit for the *xn* exit channels in the ^{40}Ca- induced reaction. Right: Comparisons of ^{48}Ca projectiles reacting with various lanthanide targets. The ^{165}Ho, ^{162}Dy, ^{159}Tb, and ^{154}Gd data are taken from [50]. The data on the Yb targets are taken from [49]. Calculated values of the capture cross section, σ_{capt}, are presented for the ^{154}Gd, ^{172}Yb, and ^{176}Yb targets in the solid, dashed, and short-dashed curves, respectively. The trend shows that the more neutron-deficient reaction systems have smaller cross sections. Figure used with permission from [50].

1.4.2. Collective Enhancement to the Level Density

The discrepancy between the shell-model calculations and experimental data for reactions near the $N = 126$ shell is most clearly shown by the left panel in Fig. 1.8. To explain the discrepancy, Junghans *et al.* [58] proposed that the collective motion of the nucleus may bring rotational and vibrational excitation states from the high-energy

continuum down into lower energies, thus increasing the level density in the low-energy regime (this phenomenon will be called collective effects to the nuclear level density, CELD, and will also be called collective effects). As the CN deexcites, the nuclear level density (NLD), and thus the strength of CELD, depends on the initial and final shapes of the system.

In the particle emission process, the shape of the excited nucleus undergoing emission is essentially the same before and after the particle is emitted (e.g. see the values of β_2 as calculated by [40]). Due to the small shape change in the particle emission process, the initial and final states have very similar NLDs. However, a nucleus undergoing fission experiences a great shape change until the nucleus ultimately fragments into two pieces. For a spherical CN, which initially has no rotational levels, the fission process will introduce many rotational levels and greatly enhance the level density. For a deformed CN, the initial state already has many rotational levels, and the strength of CELD will not be as great. The end result of the CELD phenomenon is that the fission probability is greatly enhanced for spherical CN. This effect will not be as strong for a CN which is deformed. Thus, CELD could explain why cross-sectional enhancement is not observed for the CN produced near the N = 126 spherical closed shell.

The collective enhancement factor directly multiplies the level density as such:

$$\rho(E) = \rho_{\text{int}}(E) K_{coll}(E), \tag{1.10}$$

$$K_{coll}(U, \beta_2) = K_{rot}\varphi(\beta_2) f(U) + K_{vib}[1-\varphi(\beta_2)] f(U), \tag{1.11}$$

where in Eq. (1.10), ρ_{int} is the intrinsic level density (mainly rotational and vibrational levels) of a nucleus at a given excitation energy E, and K_{coll} is the CELD factor which multiplies the level density [59]. In Eq. (1.11), K_{rot} and K_{vib} are the respective collective enhancement factors for rotational and vibrational levels, $\varphi(\beta_2)$ is a smoothing function that weights K_{rot} and K_{vib} by the initial deformation of the deexciting nucleus, and $f(U)$ is a Fermi function that fades out the strength of CELD with increasing excitation energy. Full details of the CELD calculations are presented in Section 3 of this dissertation.

The nature of CELD and its importance is a topic of debate and current investigation. Good agreement of theoretical calculations with experimental data has been achieved for models both with and without CELD included. Because CELD directly affects the nuclear level density, the most direct way to study its effect is to either directly count low-energy levels or study neutron resonance data. Other experimental observables which may be affected by CELD include the level density parameter (this will be defined in Section 3.3), cross sections, energies of emitted particles from excited nuclei, fission fragment probabilities, or other observables which can be related to the level density.

Various experimental data support the importance of the CELD phenomenon. The measurement of fusion-evaporation cross sections in ^{48}Ca-, ^{50}Ti-, and ^{54}Cr-induced reactions and analysis with a theoretical model concluded that the inclusion of CELD was necessary to reproduce the data [50, 51]. The results of theoretical calculations in these works were approximately one order of magnitude above the data when CELD was not included as shown in Fig. 1.11. The reactions studied in these works are very similar to the ^{45}Sc- and ^{44}Ca-induced reactions presented in this work, and the conclusions

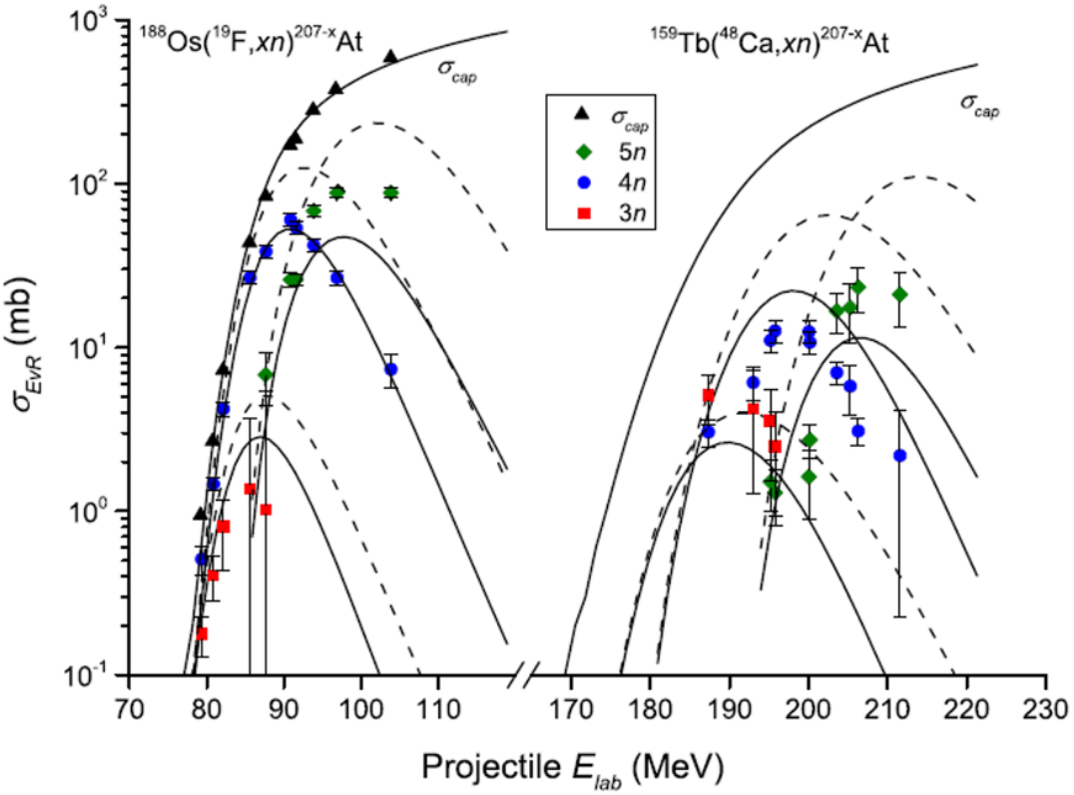

Figure 1.11. Evaporation residue cross sections for the ^{19}F + ^{188}Os (left) and ^{48}Ca + ^{159}Tb (right) reactions. Solid points indicate experimental data. The solid lines are cross section calculations with CELD, and the dashed lines are calculations without CELD. The ^{19}F + ^{188}Os data are taken from [60], and the ^{48}Ca + ^{159}Tb data are taken from [50]. Figure used with permission from [50].

drawn about CELD in this work will be discussed in the context of the conclusions drawn from this previous work. In addition to the excitation function measurements, other experimental observables have been used to examine the potential effects of CELD. The measurement of fission fragment probabilities from electromagnetically excited nuclei near the $N = 126$ shell suggested that CELD may augment the total fission probability [61]. Fig. 1.12 shows measured fission cross sections as a function of neutron number. The results show that the presence of the shell does not appear to inhibit the fission probability. The CELD phenomenon should increase the level density at low excitation energies, an effect which was studied by Roy *et al.* by measuring evaporated neutron spectra from both deformed and spherical excited CN produced in ^{4}He-induced reactions [62]. It was found that for the deformed nuclei, the level density parameter was increased as the CN excitation energy, E^*, decreased from 35 MeV to 25 MeV. The same effect was not observed from the spherical CN. The increase in level density parameter for the deformed nuclei at $E^* = 25$ MeV was tied to CELD, and it showed that the fade-out of CELD with increasing E^* had not yet occurred. Other work has not explicitly stated the influence of CELD, but has suggested that CELD may be important when a discrepancy between experimental data and a theoretical calculation is observed. For example, excitation functions of ^{19}F-induced reactions were measured by Singh *et al.* and fit with a statistical model [63]. When the statistical model analysis needed an energy-dependent scaling factor to reproduce the data, it was suggested that the neglect of CELD could have caused the initial discrepancy.

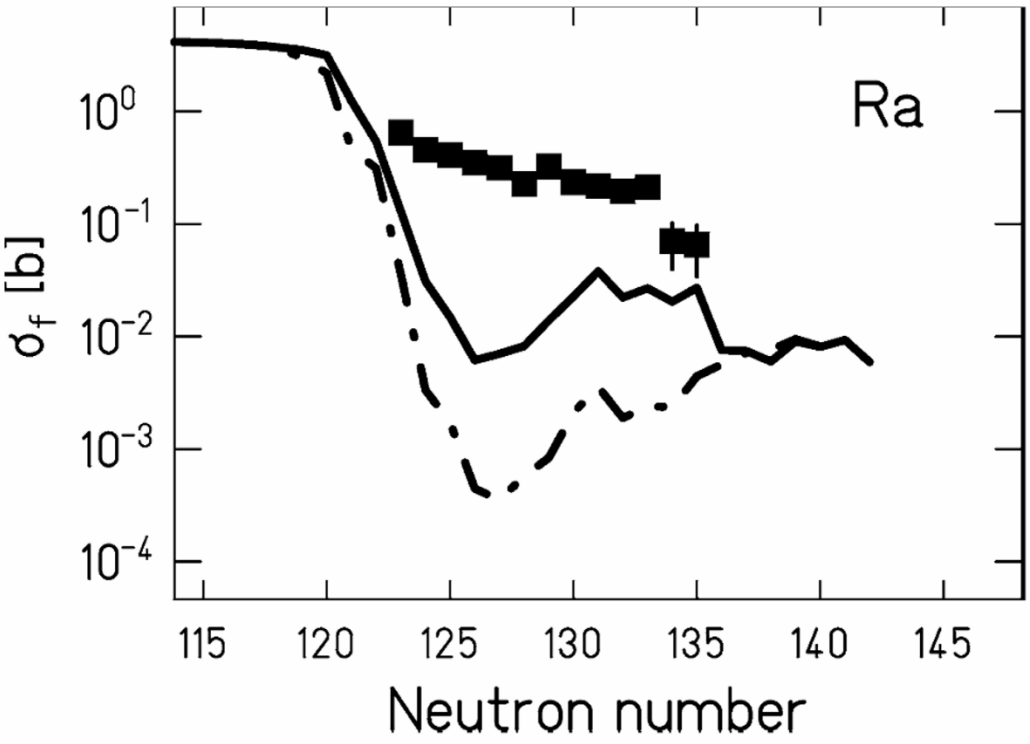

Figure 1.12. Fission fragment cross sections of Ra isotopes near the N = 126 shell from electromagnetically excited nuclei. The solid points are experimental data, the dashed–dot line is a theoretical calculation including shell and pairing effects. The solid line has the shell and pairing effects plus CELD. Figure adapted used with permission from [61].

Despite the seemingly strong evidence that CELD is an important effect in calculating the level density, the results are model dependent, and many works have concluded that CELD is not necessary using a variety of techniques. Siwek-Wilczyńska *et al.* tested their calculations with measured excitation functions for ^{224}Th and ^{248}Cf and concluded that CELD was not necessary to fit the experimental data [64]. It should be noted that the CN studied in that work were deformed and not close to any closed shells, which makes the CN less sensitive to the influence of CELD because they were deformed. Other authors have suggested that commonly used models to calculate the

fission barrier over-predict the actual fission barrier [65]. In these cases, the fission barriers needed to be reduced by a variable scaling factor. Decreasing the fission barrier would increase the fission probability and reduce EvR cross section; CELD also has this effect, and distinguishing between the two effects is quite challenging. This challenge is augmented by the uncertainly in the theoretical fission barrier, which is estimated to be ±0.5 MeV [66]. Komarov *et al.* measured of the angular and energy spectra of α particles emitted from ^{178}Hf as well as EvR cross sections at many different energies [67]. It was expected that they would observe a noticeable fadeout of CELD with increasing E^*, but instead they did not see any influence of CELD whatsoever. A summary of important experiments which investigated CELD is presented in Table 1.1. Based on all the evidence presented above, more investigation into the importance of CELD is clearly warranted.

Table 1.1. Summary of selected campaigns to investigate CELD sorted from newest to oldest.

Reference	Year(s) Published	Measured Observable	CELD reported?
[68]	2014, 2015	EvR cross sections	Yes
[62]	2013	Evaporated neutron energy spectra	Yes
[67]	2007	α-particle energy spectra	No
[64]	2005	EvR cross sections	No
[61]	2003	Fission fragment cross sections	Yes

1.4.3 Other Phenomena that May Influence the Measured Cross Sections

Other phenomena aside from CELD may affect the EvR cross sections and deserve brief mention here. One such effect is the delay of fission due to the viscosity of the hot, rotating nuclear system. This is an extension of Kramers' Principle, which was first proposed for the explanation of Brownian motion [69]. As discussed, the nucleus can be modelled as a hot, rotating liquid drop, and calculating the viscosity of that drop is a natural extension of this model. When considering the fission of a nucleus, the viscosity of the nucleus slows the motion of the two separating fragments. The viscous effect causes fission to happen on a longer timescale and allows more time for particles to be emitted instead. The viscosity is higher at higher excitation energies, and this effect can increase the cross sections for exit channels where large numbers of particles are emitted (e.g. the *6n* or *p5n* exit channels). The dissipation effects are incorporated by modifying the statistical fission decay width [47]:

$$\Gamma_f^{Kramers} = \Gamma_f \left(\sqrt{1+\gamma^2} - \gamma\right), \tag{1.12}$$

where Γ_f is the fission decay width (described in Section 3) and γ is the nuclear viscosity parameter. Typical values of γ range from 1-20 (see [47] and references therein).

In addition to fission dissipation, it is possible that some particles are emitted before the CN has fully equilibrated in temperature and shape. As the nucleons mix and the whole system travels toward equilibrium, the energy of each individual nucleon is governed by local two-body collisions. There exists a finite possibility that one particle or a cluster of particles will gain enough energy to overcome the attractive nuclear forces

and escape the di-nuclear system before equilibration has occurred. This "pre-equilibrium emission" has been shown to compete effectively with emission from an equilibrated CN for a variety of reactions even at low energies [70]. Some common properties of pre-equilibrium emission include a broadening of the excitation function at high energies, and a large number of forward-focused particles emitted at high energies. Unfortunately, our experiments are not sensitive to either fission dissipation or pre-equilibrium emission, so we cannot quantitatively comment on them in this dissertation. However, we do recognize that these phenomena may affect the excitation functions that we measure, especially at the higher energies.

1.5 Scope and Significance of the Current Work

This work is part of a systematic study of fusion-evaporation reactions with $Z \geq 20$ projectiles. Excitation functions for the reactions ^{45}Sc + $^{156\text{-}158}$Gd, ^{160}Gd, ^{159}Tb, and ^{162}Dy, and ^{44}Ca + ^{158}Gd, ^{159}Tb, and ^{162}Dy were measured and are presented in this dissertation. ^{45}Sc is significant because it has one more proton than ^{48}Ca, which has been extensively used for the production of superheavy elements with Z = 112-118. After the synthesis of element 118 in the ^{48}Ca + ^{249}Cf reaction, the best reaction to produce element 119 would be the ^{48}Ca + ^{254}Es reaction; in fact, this reaction was attempted in 1985 and an upper limit of 300 nanobarns was set [71]. However, there is not a sufficient quantity of ^{254}Es (or any other isotope of Es) available in the world to produce a target for such a beam experiment. Therefore, the next route to synthesizing elements with Z >

118 is to start using projectiles with Z > 20, and ^{45}Sc could be suitable for this purpose. Very few complete fusion experiments have been done with ^{45}Sc projectiles, and, to the best of our knowledge, these are the first reported data of hot fusion reactions with ^{45}Sc reactions aimed at studying the fusion-evaporation reaction mechanism and commenting on the applicability toward SHE synthesis. The use of ^{44}Ca as a projectile is interesting because ^{44}Ca is only one proton removed from ^{45}Sc, but the differences in the properties of the CN, such as B_f and S_n, are quite different even in reactions on the same targets. The ^{44}Ca-induced reactions can also be compared to the ^{48}Ca-induced reactions on the same targets.

These reactions studied in this work produce CN near the N = 126 spherical closed shell. Due to the proximity to the shell closure, the CN have significant enhancement to the fission barrier that should increase the EvR cross sections. Shell corrections to the fission barrier range between 2 and 5 MeV as shown in Table 1.2.

Table 1.2. Important properties of the CN studied in this dissertation. The shell correction energies are taken from [40]. The negative shell correction corresponds to an increase in the fission barrier. The ground state deformation is taken from [40] and the deformation at the saddle point is taken from [72].

Projectile	Target	CN	N_{CN}	Δ_{shell} (MeV)	$\beta_{2,\,GS}$	$\beta_{2,\,saddle}$
^{45}Sc	^{156}Gd	^{201}At	116	-2.14	0.071	1.347
	^{157}Gd	^{202}At	117	-2.87	0.062	1.385
	^{158}Gd	^{203}At	118	-3.59	0.045	1.423
	^{160}Gd	^{205}At	120	-5.07	0.035	1.498
	^{159}Tb	^{204}Rn	118	-2.90	-0.087	1.287
	^{162}Dy	^{207}Fr	120	-3.66	-0.104	1.235
^{44}Ca	^{158}Gd	^{202}Po	118	-4.64	0.009	1.575
	^{159}Tb	^{203}At	118	-3.59	0.045	1.423
	^{162}Dy	^{206}Rn	120	-4.26	-0.044	1.356

However, the CN are spherical in the ground state (and are assumed to remain spherical in the excited state). The quadrupole deformation parameter, β_2, is a parameter commonly used to describe the shape of the nucleus. Values of deformation parameter $\beta_{2,\,GS}$ and $\beta_{2,\,saddle}$ are given in Table 1.2 for the ground state of the CN and at the fission saddle point, respectively. As shown, there is a large change in deformation that occurs as the CN fission, which suggests that these CN are good candidates for studying the CELD effect.

These reactions are also good candidates for studying the effects of the relative neutron content on the EvR cross sections. The CN produced in these reactions are

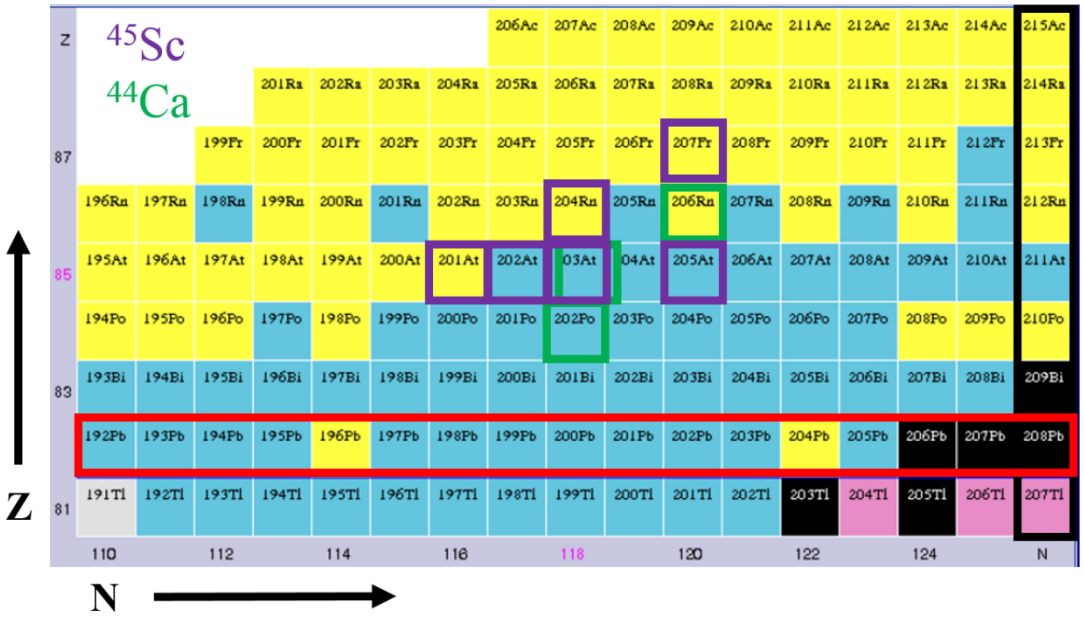

Figure 1.13. Region of the chart of the nuclides highlighting the CN studied in this work. The red and black boxes are the Z = 82 and N = 126 spherical shell closures. The purple boxes indicate the ^{45}Sc-induced reactions and the green boxes indicate the ^{44}Ca-induced reactions. The ^{203}At CN was studied in both ^{45}Sc- and ^{44}Ca-induced reactions. The chart of the nuclides is adapted from [29].

highlighted in the chart of the nuclides presented in Fig. 1.13. The ^{45}Sc projectiles bombarded four different isotopes of Gd in order to quantify how the EvR cross sections change with the changing neutron number of the compound nucleus. ^{44}Ca has four fewer neutrons than ^{48}Ca, and by bombarding the same targets with these two projectiles we can again study the effects of the neutron content on the EvR cross sections. Additionally, the ^{45}Sc + ^{158}Gd and ^{44}Ca + ^{159}Tb reactions are cross-bombardments; both reactions produce the same CN. The cross bombardment was crucial to understand how the projectile influenced the final EvR cross sections.

These reaction systems were chosen to be analogs of reactions which produce CN near the predicted N = 184 spherical closed shell. In addition to producing spherical nuclides near a closed neutron shell, the CN in this work are produced with excitation energies of ≈ 30-60 MeV, similar to the CN produced in the hot fusion reactions which synthesized elements with Z = 113-118. Because projectiles with Z > 20 are going to be used to synthesize these next SHEs, studying reactions with these projectiles is useful to understand how the cross sections of the SHEs may change. In addition to the ^{45}Sc and ^{44}Ca-induced reactions studied in this work, reactions with ^{48}Ca, ^{50}Ti, and ^{54}Cr were presented in previous papers and a dissertation [73]. The study of the fusion-evaporation mechanism in this work can hopefully be extended to help select the most favorable reaction in trying to synthesize the next SHEs with Z > 118.

2. EXPERIMENTAL METHODS

The experiments described in this dissertation were performed at the Texas A&M University Cyclotron Institute in four temporally separated experiments. The ^{45}Sc and ^{44}Ca projectiles were accelerated with the K500 superconducting cyclotron and bombarded stationary targets. The Momentum Achromat Recoil Spectrometer (MARS) was used to physically separate the unreacted beam particles and other unwanted reaction products from the desired EvRs. MARS has been previously described in detail [74] and used in nuclear astrophysical experiments, but has also been characterized for heavy-ion induced ($Z \geq 18$) fusion-evaporation reactions with projectile energies just above the Coulomb barrier [75]. The important features of the experimental equipment, methods, and data analysis techniques are comprehensively covered in this section.

2.1. Production of Beams and Targets

2.1.1 Beam Preparation

To perform the nuclear reactions studied in this work, an accelerated beam of projectiles from the cyclotron was required. Gas-phase atoms of ^{45}Sc were produced by sputtering atoms off a solid piece of ^{nat}Sc metal, while gas-phase atoms of ^{44}Ca were produced by heating ^{44}CaO powder in a high temperature oven. The ^{45}Sc starting material was simply a solid chunk of ^{nat}Sc metal, as ^{45}Sc is the only stable isotope. The

material for the ^{44}Ca beam was purchased from Isoflex (> 95.90% ^{44}CaO, San Francisco, CA, USA) in the powder form. In both cases, the ions were then transported into a 6.4 GHz electron cyclotron resonance (ECR) ion source, where they were bombarded by high-energy microwaves that knocked off electrons and created positively charged ions. This newly created plasma was contained and shaped by a strong magnetic field which "squeezed" some of the ions out of the end of the ECR source. These ions were then steered into the K500 cyclotron and accelerated to the requested energy. The cyclotron also served as selector based on the charge-to-mass ratio, *Q/M*, of the ions and helped to eliminate unwanted contaminants such as oxygen. The charge states of the ^{45}Sc and ^{44}Ca projectiles discussed in this work were both 6^{+}.

The beam energies from the cyclotron for these experiments ranged between 4.8–5.1 MeV/nucleon; these energies were just above the Coulomb barrier between the projectile and target nuclei. These energies were also carefully selected to account for energy loss through the degrader described in Section 2.1.2 below. The beam energy which represents the maximum 4*n* EvR cross section was estimated for each reaction using the theoretical model described in Section 3 and with the fusion-evaporation codes available from the theory group at the Joint Institute for Nuclear Research in Dubna, Russia [76, 77]. The values obtained from these two methods were always within a few MeV, and the average was used to estimate the energy for maximizing the 4*n* EvR. These beam energies were standard for 'hot fusion' reactions, in which the beam energy is above the Coulomb barrier, and three to six particles are typically evaporated from the

compound nucleus. To achieve the requested energy, the K500 cyclotron was operated in third harmonic mode.

The beam energy for each experiment was determined experimentally by passing the accelerated ions through a ~ 0.05 mg/cm^2 ^{nat}C foil and measuring the magnetic rigidities of the resultant charge states. The estimated uncertainty in the beam energy measurement was ≈ 1%. The beam intensities were monitored using two Faraday cups (FCs). Each FC was a piece of metal which was bombarded by the charged projectiles and measured their current, which was then be converted into a number of particles per second. The first FC was located shortly downstream of the extraction point of the K500 cyclotron (FCO2) and one located in the Target Chamber of MARS (TC FC). The TC FC had a biased electron suppression ring to more accurately determine the beam intensity. Typically, the TC FC read ≈ 30-40% of the value of FC02, indicating that FC02 reads high due to the lack of an electron suppression system. The average beam intensities on the target ranged from 1.8-3.2 particle nanoamperes (pnA; 1 pnA = 6.24 x 10^9 particles per second) for the ^{45}Sc experiments, and was 0.8 pnA for the ^{44}Ca experiment.

2.1.2 Target Preparation

The targets used in all the experiments were all thin foils of the lanthanide elements Gd (Z = 64), Tb (Z = 65), and Dy (Z = 66). The Gd targets, $^{156}Gd_2O_3$ (479 μg/cm^2 on a 2 μm Ti backing), $^{157}Gd_2O_3$ (405 μg/cm^2 on 2 μm Ti), $^{158}Gd_2O_3$ (see below), and $^{160}Gd_2O_3$ (655 μg/cm^2 on 2 μm Ti) were all in the oxide form and were prepared on-site using the molecular plating technique. The ^{45}Sc experiments used a (680 μg/cm^2 on 2 μm Ti) $^{158}Gd_2O_3$ target, while the ^{44}Ca experiment used a (334 μg/cm^2 on 2 μm Ti) $^{158}Gd_2O_3$ target. The ^{159}Tb target (497 μg/cm^2, self-supporting) was purchased from Microfoils Co. (Arlington, WA, USA). The ^{162}Dy target (403 μg/cm^2 on

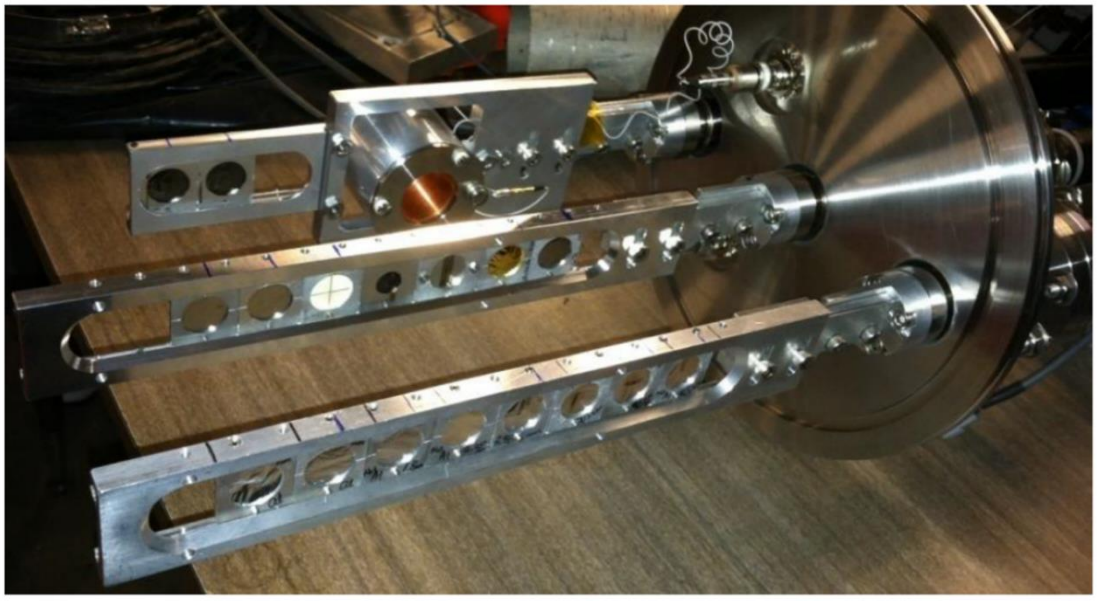

Figure 2.1. Target ladder assembly used in the experimental work. The first ladder (nearest to the bottom of the figure) held the Al degraders to vary the beam energy. The middle ladder held the various targets for calibrations and for the reactions studied in this work. The last ladder held the TC FC and the two ^{nat}C charge equilibration foils.

75 μg/cm^2 ^{nat}C) was provided by Heavy Element and Radiochemistry Group at Lawrence Berkeley National Laboratory. Additionally, targets of ^{118}Sn (various thicknesses, used in the ^{45}Sc experiments) and ^{116}Sn (640 μg/cm^2, self-supporting, used in the ^{44}Ca experiment) were irradiated in order to calibrate the focal plane silicon detector for the energy of the recoiling daughter nucleus in an EvR α-decay event. This procedure will be described in Section 2.4.

The targets were mounted on a "target ladder" and inserted into the target chamber for the beam irradiations. The ladder was made of Al and had the capability of holding up to 8 targets. A photograph of the target ladder with targets in place is shown in Fig. 2.1. In addition to the targets, a thin piece of Al painted with a fluorescent ZnCdS coating was mounted on the target ladder. When irradiated by the accelerated beam, this "viewer" emits visible light, which enabled visual alignment of the beam on the center of the target. Also shown in Fig. 2.1 is an identical ladder (nearest to the bottom of the figure) located just in front of the target ladder that held ^{nat}Al foils of various thicknesses. These foils served as "degraders" which reduced the energy of the beam particles before they bombard the target. The thicknesses for the degraders ranged between 1.2-8.5 μm of ^{nat}Al, which corresponded to a reduction in the beam energy of ≈ 5-40 MeV, depending on the mass and initial energy of the beam projectiles. There was also a blank slot on the degrader ladder, allowing the full beam energy from the cyclotron to be used if desired. The beam energies from the cyclotron were carefully selected so that the maximum 4*n* EvR cross section was obtained with a degrader of intermediate thickness. Immediately behind the target ladder in Fig 2.1 is a third ladder

which held two ~50 μm/cm^2 ^{nat}C foils and the TC FC. The ^{nat}C foils served to equilibrate the charge state distribution of the EvRs after they were produced in the target and are thus called “charge equilibration foils”. The TC FC served to directly measure the primary beam intensity in the target chamber and was checked periodically throughout the experiments. All three ladders were remotely controllable through a custom LabView [78] interface which communicated to the linear actuators on the ladders. The positions of the targets, degraders, ^{nat}C foils, and the Faraday Cup were aligned using a transit prior to the beginning of the experiment and the positions were saved in the LabView software.

2.1.3 Molecular Deposition of Gd_2O_3

As stated above, all of the Gd_2O_3 targets were prepared using the molecular deposition technique [79, 80]. Molecular deposition was chosen because it is highly efficient and only requires a simple experimental setup (as opposed to vapor deposition or rolling techniques, which are either inefficient, require expensive equipment to perform, or both). A 50 mg quantity of $^{156}Gd_2O_3$ (95.40% enrichment, powder form) was purchased from Isoflex Inc. (San Francisco, CA, USA), while the other isotopes of Gd were obtained from the previous target-making group at the Cyclotron Institute. To begin the molecular deposition process, a small quantity (~1-2 mg) of the Gd isotope was dissolved in excess dilute nitric acid (0.1 M or 2 M) and evaporated to dryness under Ar gas to drive off any excess water. The sample was then reconstituted in 5-10

μL of 0.1 M HNO_3 and ≈ 12 mL of pure, anhydrous isopropanol and added into the electrodeposition cell. The material for the 2 μm ^{nat}Ti backing foil was purchased from Hamilton Precision Metals (Lancaster, PA, USA). The 2 μm ^{nat}Ti foil was cut with a circular punch to a 1.9 cm diameter, and it was cleaned in acetone, 2 M HNO_3, water, and anhydrous isopropanol before being placed into the electrodeposition cell. The electrodeposition cell is depicted in Fig. 2.2. The main body of the cell was made of the plastic polymer polyether ether ketone (PEEK). The PEEK polymer is mechanically strong, thermally stable, and resistant to chemical attack. The base of the cell was constructed from solid Al and served as the grounded cathode. The 2 μm Ti backing foils were placed onto the center of the Al base. The total volume of the cell was ~15 mL, and the typical volume of the deposition solution was ~ 12 mL. A high voltage power supply applied a bias of 400-700V to the Pt anode and created the electric field to drive the molecular deposition in the cell. The deposition voltage was varied to keep the current at ≈2 mA/cm^2 to get the best deposition quality [81, 82], and the voltage was applied for 30-60 min. A high-speed stirring rod was used to evenly mix the solution during the deposition process. Chemically, the deposited material was $Gd(NO_3)_3$, so the targets were baked at 200°C under atmospheric conditions after the deposition occurred to convert the material to the oxide form. The resultant thin Gd_2O_3 layer had a diameter of 1.6 cm and an area of 2.275 cm^2. The electrodeposition process typically had an overall efficiency of 50-100%.

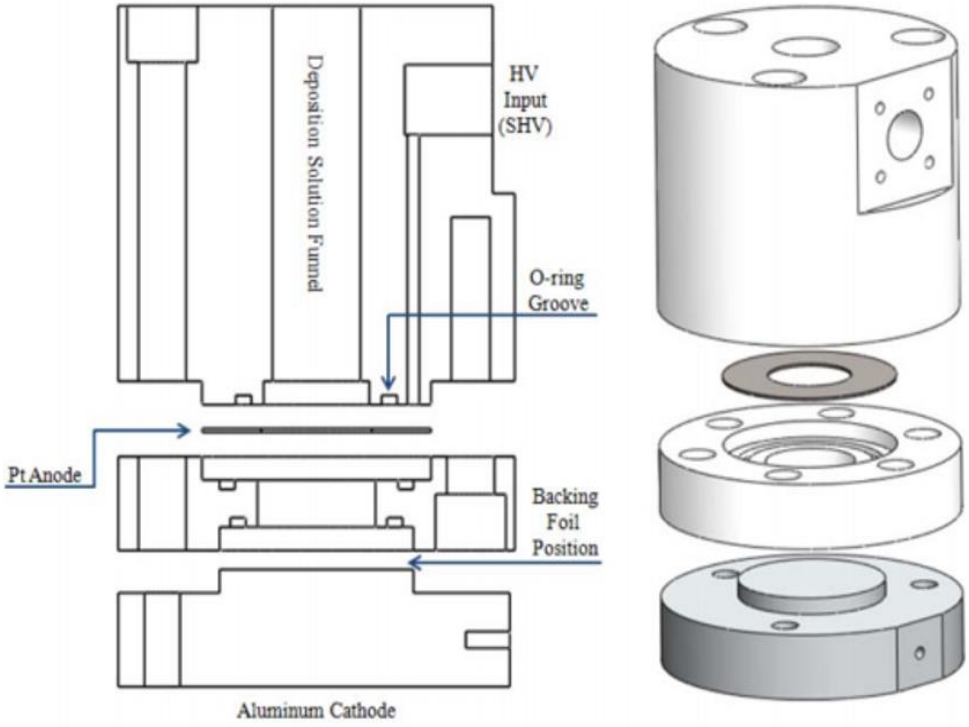

Figure 2.2. Schematic of the electrodeposition cell used to produce lanthanide targets. The left side shows a cross sectional view of the key components of the cell. The cell holds ~ 15 mL of liquid. The right side shown a 3-dimensional picture of the cell assembly. The main body of the cell (two pieces shown in white) was constructed from PEEK, the gray disk in the center was the Pt anode, and the bottom gray piece was the Al cathode.

The Texas A&M University Materials Characterization Facility analyzed the Gd_2O_3 targets using secondary-ion mass spectroscopy (SIMS). In the SIMS analysis, heavy ions were accelerated in an electric field and bombarded the sample of interest to knock off secondary ions from the sample surface. The secondary ions were focused and analyzed by a mass spectrometer. In addition to measuring the masses of the secondary ions, other detectors within the instrument measured the current and the spatial distribution of the ions. The mass spectrometer could resolve mass differences down to a

singular atomic mass unit, and this technique was used to measure the isotopic enrichment of the each isotope of Gd within the targets. The main isotopic enrichments of the $^{157, 158, 160}Gd_2O_3$ targets were 88%, 92%, and 91%, respectively. The isotopic enrichment of the $^{156}Gd_2O_3$ target was not measured, but was assumed to be (90 ± 2)%, the average of the three values above.

2.2 The MARS Physical Separator

2.2.1 MARS Operation

The experiments described in this dissertation were performed using the Momentum Achromat Recoil Spectrometer (MARS) at the Texas A&M University Cyclotron Institute. A schematic of MARS is given in Fig. 2.3. MARS separated the desired EvRs from unreacted primary beam and other reaction products via a two-stage selection system. The first stage was the achromatic section defined by the first two dipole magnets D1 and D2, which both bend with an angle of 35°. This section of MARS separated ions based on their magnetic rigidities, $B\rho$, where B is the magnetic field and ρ is the physical radius of the magnet. The magnetic rigidity equal to the linear momentum of an ion divided by its charge state, q, as shown in Eq. (2.1)

$$\beta\rho = mv / q \ . \qquad (2.1)$$

The unreacted primary beam particles had similar charge states but much higher momenta than the EvRs, and as such had higher magnetic rigidities. The magnetic fields

in D1 and D2 were tuned to steer the EvRs through the separator, while the unreacted beam was stopped by a tungsten block "beam dump" section of MARS. The second stage of MARS is the "Wien Filter" which selected particles based on their velocities. The Wien Filter employed perpendicular electric and magnet fields to create forces on the charged particles passing through it. Based on the opposing forces in the Wien Filter, particles with a certain velocity traversed the filter with a straight path, while other velocities were steered into the walls. The force equations are given in Eq. (2.2), while the velocity which will experience a zero net force is shown in Eq. (2.3)

$$F = qE = qvB \ , \tag{2.2}$$

$$\Rightarrow v = E / B \ . \tag{2.3}$$

In the equations above, E and B are the strengths of the electric and magnetic fields, respectively, and v is the velocity at which particles travelled straight through the Wien Filter. After the two-stage separation, the desired EvR were steered through the final dipole magnet, D3. The D3 magnet rests on a moveable platform and steers the products upward with an angle that varies between 0° and 25°. For the experiments in this work, D3 was held at a constant 5° angle. Finally, the EvRs were focused into the detector chamber (DC) where they were identified by their characteristic α-particle energies. The detection system is described in Section 2.4. Overall, MARS has a background separation factor that is > 10^{15} for unreacted beam particles [75]. MARS has a geometric solid angle of 9 msr and the maximum energy acceptance is $\Delta E/E$ = 9%. This distribution of the EvRs is limited by the four sets of slits denoted by the "SL" labels in

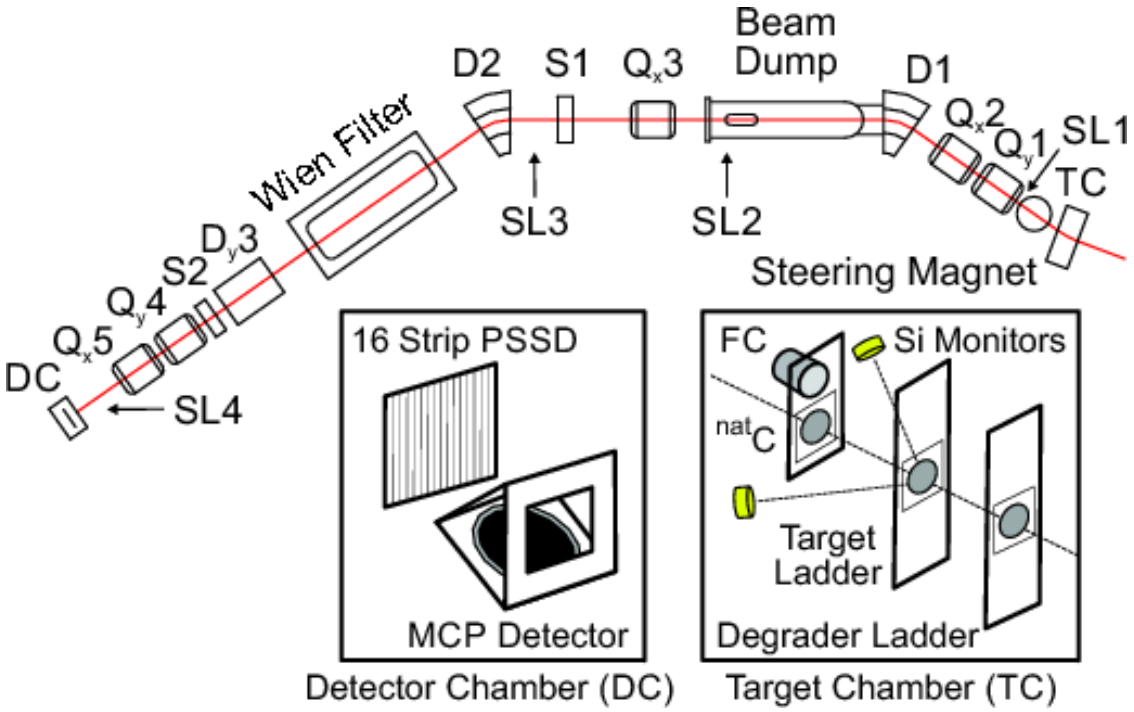

Figure 2.3. Schematic of the Momentum Achromat Recoil Separator. The beam entered the experimental area from the right-hand side of the diagram and was steered into the target chamber (TC). After the evaporation residues were produced, they were focused by the quadrupole magnets (Q1 through Q5) and steered by dipole magnets (D1 through D3). The subscripts on each of the quadrupole magnets indicated the focusing plane of the magnet. The unreacted beam and undesired reaction products were filtered by the dipole magnets and Wien Filter. The sextupole magnets S1 and S2 refocused the beam particles near the edges of the pipe. The slits SL2 defined the momentum acceptance of the separator. The EvRs were steered into the detector chamber (DC) where the implant energy and subsequent decay energy were used to identify the EvR. See the various parts of this section for a full description of all the components of MARS.

Fig. 2.3. The maximum energy acceptance is specifically limited by SL2. The maximum magnetic rigidity that MARS can steer is $B\rho$ = 2.0 T m.

The MARS separator consists of the Wien Filter, three dipole magnets, five quadrupole magnets, and two sextupole magnets. During the experiments, the fields in the Wien Filter and the currents in the magnets were manually adjusted to properly steer the desired EvRs into the focal plane of the detector chamber. To determine the proper

MARS settings, the kinematics of the reaction were calculated using the Windows-based computer program LISE++ [83]. The LISE++ program is designed to simulate all aspects of the production, transportation, and collection of fragments in any spectrometer, and a model of MARS has been implemented in LISE++ through a collaborative effort between the creators of the program at Michigan State University and staff scientists at the Cyclotron Institute. During the experiment, the beam identity, beam energy, target thickness, charge equilibration foil thickness, the *4n* EvR identity, and expected EvR charge state were entered into LISE++, and a value for $B\rho$ was calculated. Once $B\rho$ and the charge state of EvR were known (see below for more information about the charge states), the velocity and energy of the EvR could be calculated. The EvR energy, mass, and charge were then input into an Excel spreadsheet with MARS magnet calibrations. The magnet calibrations and Wien Filter calibration in this "MARS Calibrator" spreadsheet were done using α particles and are described in previous works [73, 75]. The values from the MARS calibrator were then used to set the MARS magnets and Wien Filter. Examples of the LISE++ interface and the MARS calibrator are shown in Fig. 2.4.

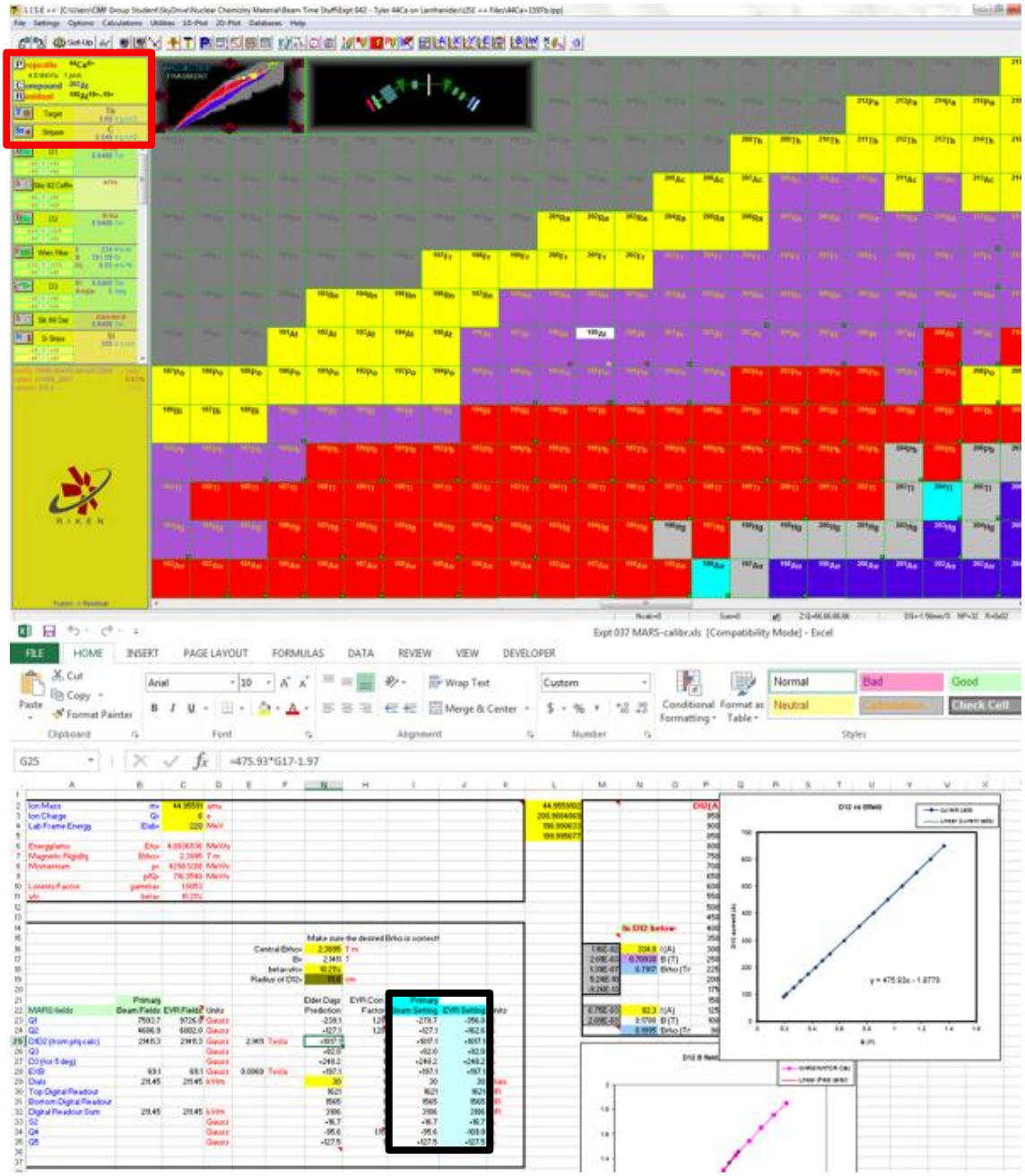

Figure 2.4. Commonly used interfaces during the beam experiments. Top: Standard LISE++ interface configured for MARS. The red box on the left-hand side indicates the input values to determine the reaction kinematics. Bottom: The MARS calibrator spreadsheet. The values in the black box are the MARS settings that were used to tune the primary beam (left column within the box) or the EvRs (right column)

2.2.2 Charge States and MARS Efficiency

MARS is a vacuum separator with typical operating pressures of 10^{-5} – 10^{-7} torr. The EvRs that were produced in the fusion-evaporation reactions have numerous charge states, and the distribution of EvR charge states produced by the reaction was fairly broad due to the kinematics of the reaction. However, due to the large separation in βp of the individual charge states, only one charge state may be efficiently transmitted through MARS at a time. The efficiency of MARS, ε_{MARS}, was thus fairly low for these fusion-evaporation reactions. LISE++ is an extremely versatile program which has numerous useful capabilities and equations embedded into it. One such quantity that LISE++ can calculate is the charge state distribution of the EvRs after they pass through the target and the charge equilibration foil. LISE++ has multiple methods to calculate the charge-state distribution, but the semi-empirical formulas of Schiwietz and Grande [84] were chosen to do that calculation. The formulas are based an experimental fit to 850 data points for reactions on solid targets with Z = 4-83. The average charge state, q_{mean}, of the EvRs was estimated to be

$$q_{mean} = Z_p \frac{12x + x^4}{0.07/x + 6 + 0.3x^{0.5} + 10.37x + x^4} \ , \tag{2.4}$$

where Z_p is the atomic number of the projectile. The parameter x is defined as

$$x = \left(\frac{v_{EvR}}{1.68 v_0 Z_p^{-0.52} Z_t^{-0.019 Z_p^{-0.52} v_p / v_0}} \right)^{1+1.8/Z_p} , \tag{2.5}$$

where Z_t is the atomic number of the target, v_{EvR} and v_p are the velocities of the EvR and the projectile respectively, and v_0 is the Bohr velocity, $v_0 = 2.19 \times 10^6$ m/s. Experimental data on the charge state abundances were collected for several reactions in this work and compared to these calculations. Plots of calculated and experimental charge state abundances for the $^{45}Sc + ^{160}Gd$ reaction and $^{44}Ca + ^{159}Tb$ reaction are presented in Fig. 2.5. Although the units in Fig. 2.5 are arbitrary, the shape of the theoretical calculations matches well with the experimental data. The peak of the EvR charge state distribution varies with energy, and MARS was frequently tuned to select the 19^+ and 20^+ charge states, depending on the reaction and beam energy. However, many of the reactions showed contamination of the α-energy spectra due to the $B\rho$ of the unreacted beam being close to the $B\rho$ of the EvRs. This increased the background in the α-particle energy spectra and made the EvR identification more difficult. For these reactions, MARS was tuned to select one charge state above the peak of the distribution to reduce the background in the α-energy spectra. For these reactions, a correction factor was introduced to account for the fraction of EvRs lost because the peak charge state was not selected:

$$\varepsilon_{MARS} = \varepsilon_{MARS,peak}\varepsilon_{charge} \ , \tag{2.6}$$

$$\varepsilon_{charge} = \frac{N_{EvR}}{N_{EvR,peak}} \tag{2.7}$$

where $\varepsilon_{MARS,peak}$ represents the efficiency of MARS when the peak of the charge state distribution was tuned (discussed below), and ε_{charge} represents the "charge state loss factor", the fraction of EvRs that were lost when the higher charge state was tuned. The

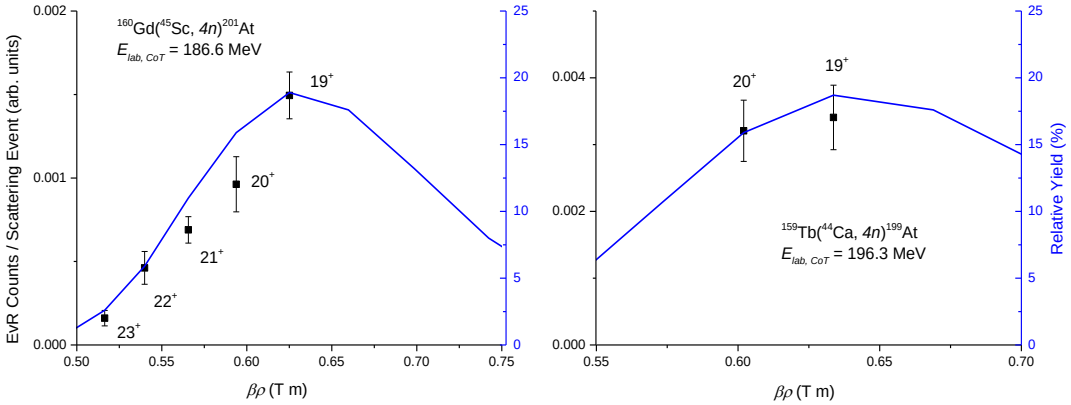

Figure 2.5. Experimental measurements (black points) and theoretical calculations (blue lines) for the charge state distributions measured in this work. The theoretical calculations were performed using the formulas of Schiwietz and Grande [84] as implemented in LISE++ [83]. Left: Results for the ^{160}Gd(^{45}Sc, *4n*)^{201}At reaction. Right: Results for the ^{159}Tb(^{44}Ca, *4n*)^{199}At reaction.

quantity ε_{charge} was easily calculated both experimentally and theoretically by comparing the number of EvRs observed at a given charge state, N_{EvR}, to the number of EvRs observed at the peak charge state, $N_{EvR,\,peak}$. The experimental data collected for ^{199}At ($E_{Lab,\,CoT}$ = 196.3 MeV) are shown on the right-hand side of Fig. 2.5. The charge state loss factor was calculated using the ^{199}At^{19+} (the most probable charge state) and the ^{199}At^{20+} charge state. The experimental yield ratio of ^{199}At^{19+}/^{199}At^{20+} was ε_{charge} = 0.94 ± 0.19, while the theoretical ratio was ε_{charge} = 0.91. This gave us confidence that the theoretical method for predicting the charge state distribution was giving reasonable results. For all of the other cases where the correction factor ε_{charge} was necessary, only the theoretical calculations were used. The tuning of EvRs with one higher charge state than the peak was done for some of the ^{45}Sc-induced reactions and all of the ^{44}Ca-induced reactions in this work.

The peak efficiency of MARS, $\varepsilon_{MARS,\,peak}$, for the EvRs was determined by studying the EvR production rates for the ^{40}Ar + ^{165}Ho and ^{40}Ar + ^{118}Sn reactions and comparing them to known literature data [54, 75]. The efficiencies for the two ^{40}Ar-induced reactions were determined to be (2.2 ± 0.5)% and (3.5 ± 0.7)%, respectively. The ^{40}Ar + ^{165}Ho reaction has much larger mass asymmetry parameter, η, than the ^{40}Ar + ^{118}Sn, where η represents the relative mass difference between the target and projectile

$$\eta = \frac{\left|A_p - A_t\right|}{A_p + A_t} \quad . \tag{2.8}$$

A_p and A_t are the atomic numbers of the projectile and target, respectively. For reactions where the projectile is lighter than the target, a larger value of η means that the projectile is much lighter in mass than the target, and the resultant angular distribution of the EvRs will be more dispersed. This results in fewer of the EvRs entering MARS and a lower efficiency. In contrast, a smaller value of η results in a higher efficiency. The reactions studied in this dissertation had values of η in between those of the ^{40}Ar + ^{165}Ho and ^{40}Ar + ^{118}Sn reactions, and $\varepsilon_{MARS,\,peak}$ was also in between those measured in the two ^{40}Ar-induced reactions. The value of η was calculated for all the ^{45}Sc and ^{44}Ca-induced reactions studied in this work, and the MARS efficiency was calculated using a linear interpolation between the efficiency values measured in the ^{40}Ar + ^{118}Sn and ^{40}Ar + ^{165}Ho reactions. The efficiencies for all nine reactions are presented in Table 2.1.

Table 2.1 MARS efficiencies and experimental charge states for all nine reactions studied in this work.

Reaction	η	$\varepsilon_{MARS,\,peak}$	Peak $4n$ Charge State	Experimental Charge State
$^{45}Sc + {}^{156}Gd$	0.55	2.8	19^+	20^+
$^{45}Sc + {}^{157}Gd$	0.55	2.8	19^+	20^+
$^{45}Sc + {}^{158}Gd$	0.56	2.8	19^+	20^+
$^{45}Sc + {}^{160}Gd$	0.56	2.7	19^+	19^+
$^{45}Sc + {}^{159}Tb$	0.56	2.8	20^+	21^+
$^{45}Sc + {}^{162}Dy$	0.57	2.7	20^+	21^+
$^{44}Ca + {}^{158}Gd$	0.56	2.7	19^+	20^+
$^{44}Ca + {}^{159}Tb$	0.57	2.7	19^+	20^+
$^{44}Ca + {}^{162}Dy$	0.57	2.6	19^+	20^+

2.3 Beam Monitoring and Cross Section Calculations

The number of beam particles bombarding the target was monitored using a pair of circular silicon "monitor" detectors (ORTEC, Oak Ridge, TN, USA, Model TU-015-150-300) located in the TC at ±30° from the beam axis and at a distance of 241 mm from the target position (see Fig. 2.3 for a depiction of these detectors). The majority of the beam particles impinging on the target did not induce a nuclear reaction; some scattered elastically due to the strong Coulomb repulsion between the projectile and target nuclei.

A fraction of the scattered beam particles were ejected with the correct angle to enter these silicon monitors. These events are called "Rutherford scattering" events, and the detectors were appropriately called "Rutherford detectors". The angles of ±30° were chosen to be small enough so that the scattering cross section was large enough to observe many events, yet large enough to avoid contamination from inelastically scattered particles, products of transfer reactions, and other unwanted reaction products. The detection efficiency of the Rutherford detectors was ≈100%. In addition to the Rutherford detectors, the beam intensity on target was monitored by taking the ratio of the TC FC current to the FC02 current. This ratio gave an idea of the error in the FC02 reading. This ratio was not used to calculate the cross sections, but was an important diagnostic tool to monitor the beam during the experiment.

The Rutherford detectors were able to accurately monitor the beam dose because the differential cross section with respect to the solid angle Ω for these scattering events is well defined [85]:

$$\frac{d\sigma_{Ruth}}{d\Omega} = \left(\frac{e^2 Z_p Z_t}{4\pi\varepsilon_0 m_p {v_{lab}}^2} \right)^2 \frac{1}{\sin^4\theta} \frac{\left\{ \cos\theta \pm \left[1 - (m_p / m_t)^2 \sin^2\theta \right]^{1/2} \right\}^2}{\left[1 - \left(m_p / m_t \right)^2 \sin^2\theta \right]^{1/2}} \ . \qquad (2.9)$$

In Eq. (2.9) above, Z_p and Z_t are the atomic numbers of the projectile and target, respectively, v_{lab} is the velocity of the projectile in the lab frame, m_p and m_t are the mass of the projectile and target, respectively, and θ is the scattering angle relative to the beam axis. If $m_p < m_t$, as is the case for every reaction studied in this work, then only the positive sign that is before the radical should be used. If $m_p > m_t$, then the sum of both the positive and negative terms (calculated separately) should be added together. All the

terms in Eq. (2.9) are known and $d\sigma_{Ruth}/d\Omega$ can be easily calculated. The two Rutherford scattering detectors were labelled "East" and "West" relative to the direction of the beam, which generally travels in a cardinal south direction.

A cylindrical plastic blocker was mounted in front of each of the Rutherford detectors to reduce the number of unwanted reaction products (from proton knockout reactions, e.g.) from entering the detectors and creating an unwanted background. Each of these "pre-collimators" was 21.6 mm in length and 6.1 mm in diameter. A second, smaller, circular collimator was positioned directly at the end of the pre-collimator to further reduce the amount of scattered beam entering each detector. This second collimator was 1 mm in diameter for the ^{45}Sc + ^{159}Tb and ^{162}Dy experiments, and it was 2 mm in diameter for all of the other experiments in this work. In practice, the solid angle that was "seen" by each Rutherford detector needed to be calibrated before each experiment. This was done by measuring the scattering of beam particles off of some combination of the following targets: $^{116, 118}$Sn (Z = 50), ^{159}Tb (Z = 65), ^{165}Ho (Z = 67), ^{181}Ta (Z = 73), and ^{197}Au (Z = 79). The effective solid angle was determined by the following equation:

$$\Omega_{eff} = \frac{N_{Ruth}}{(d\sigma_{Ruth}/d\Omega)N_t \int I(t)dt} \quad . \tag{2.10}$$

All of the terms on the right-hand side of Eq. (2.10) were known during the experiments. N_{Ruth} was the number of observed Rutherford scattering counts and was obtained by integrating the appropriate region of the Rutherford scattering energy spectrum, $d\sigma_{Ruth}/d\Omega$ was calculated using Eq. (2.9), N_t was the areal atom density of the target

(which was assumed to be constant), and I_t, the beam intensity, was obtained from the average beam current on FC02. The irradiations to determine Ω_{eff} were short, and the beam intensity was relatively constant during the runs. The average of the beginning and ending current readings on FC02 was used to determine Ω_{eff}. This was the only time that either FC was actually used to calculate a beam dose – once Ω_{eff} was determined at the beginning of an experiment, all of the subsequent beam doses were determined using the Rutherford detectors. Although FC02 was known to read high due to the lack of an electron suppression system, it was still used to determine Ω_{eff} for all the experiments presented in this work. The correction introduced by the TC FC was applied later in the analysis process when the cross sections were being calculated. It is interesting to note that Ω_{eff} comes into good agreement with the true value of Ω (calculated based on the size of the collimator and the distance from the target to the collimator) once the TC FC correction was applied.

The number of EvR *produced* in a given irradiation, N_{EvR}, can be calculated using the following equation:

$$N_{EvR} = \sigma_{EvR} N_t \int I(t)dt \ . \tag{2.11}$$

This equation is valid only for "thin" targets, but the thin targets used in these experiments justify the approximation. Rearranging Eq. (2.10) to solve for $N_t \int I(t)dt$ (this quantity is called the "luminosity") and solving Eq. (2.11) for the cross section results in the following expression:

$$\sigma_{EvR,ideal} = \frac{N_{EvR}\Omega_{eff}\left(d\sigma_{Ruth}/d\Omega\right)}{N_{Ruth}} \ . \tag{2.12}$$

This cross section is labelled as the "ideal" cross section because in an ideal world, every single EvR which was produced would also be detected. Instead, corrections need to be made for the efficiencies of MARS, ε_{MARS}, the detectors, ε_{detect}, and the α-branching ratio, ε_{α}. The experimentally measured cross sections were finally calculated as

$$\sigma_{EvR} = \frac{N_{EvR,detect}}{N_{Ruth}} \Omega_{eff} \left(d\sigma_{Ruth} / d\Omega \right) \frac{1}{\varepsilon_{MARS} \varepsilon_{detect} \varepsilon_{\alpha}} \ , \qquad (2.13)$$

where $N_{EvR,\ detect}$ represents the number of detected α-decay events in the position-sensitive silicon detector for a given EvR. The MARS efficiency was discussed above, and the detection efficiency, ε_{detect}, will be discussed below. The α-branching ratios, ε_{α}, varied from ≈2% to 100% for the EvRs studied in this work.

2.4 Focal Plane Detection System

The evaporation residues produced in the ^{45}Sc- and ^{44}Ca-induced reactions were separated using MARS and focused into the DC (see Fig. 2.3). The quadrupole magnets Q4 and Q5 focused the products at a given location in the DC, and the plane along the focusing axis is known as the "focal plane". In the DC, a singular position-sensitive silicon detector (PSSD) was positioned in the focal plane, and the EvRs implanted into this PSSD. The PSSD (model X1, Micron Semiconductors Ltd., Lansing, UK) had one "full-energy" signal that measured the total charge created by each implant or decay event plus sixteen vertical charge-resistive strips that measured the vertical position of the events by extracting charge from the top of the detector. The horizontal position

resolution was defined by the ≈ 3 mm width of the strips. The PSSD had an active area of 50 mm x 50 mm, was 300 μm thick, and was biased to +60 V for these experiments. The PSSD energy signal was calibrated before the experiment using an α-particle source comprised of ~10 nCi each of ^{148}Gd, ^{239}Pu, ^{241}Am, and ^{244}Cm. An example energy calibration spectrum is shown in Fig. 2.6. This calibration gave the proper energy for an "external" alpha particle which impinged on the detector from an outside source. A secondary calibration was necessary after the start of the experiment to correct for the energy of the recoiling daughter nucleus which is captured when an EvR decays *inside* the PSSD. To do this "internal" calibration, the α-decaying products of the ^{45}Sc + ^{118}Sn reaction (for the ^{45}Sc experiments) or the ^{44}Ca + ^{116}Sn reaction (for the ^{44}Ca experiment) were measured, and a best fit was determined. An example of this internal calibration is also presented in Fig. 2.6. The formulas used to obtain the measured α-energy values are:

$$E_{\alpha,external} = m_{ext}(Channel) + b_{ext} \tag{2.14}$$

$$E_{internal} = m_{int}(E_{\alpha,external}) + b_{int} \tag{2.15}$$

$$E_{\alpha,measured} = m_{ext}m_{int}(Channel) + m_{int}b_{ext} + b_{int}, \tag{2.16}$$

where *m* and *b* are the slope and intercept and the subscripts denote the internal and external calibrations.

The PSSD position signals were calibrated using a 6-slit mask. The slits on the mask were 1 mm wide and were separated by 8 mm, and the positions of the slits relative to the center of the PSSD were known. To measure the position, the PSSD recorded the amount of charge extracted at the top of the detector. Due to the resistive nature of the strips, events which occurred far away from the top of the detector had a smaller recorded charge signal than an identical event which occurred near the top of the detector. The recorded position was calculated with the following equations:

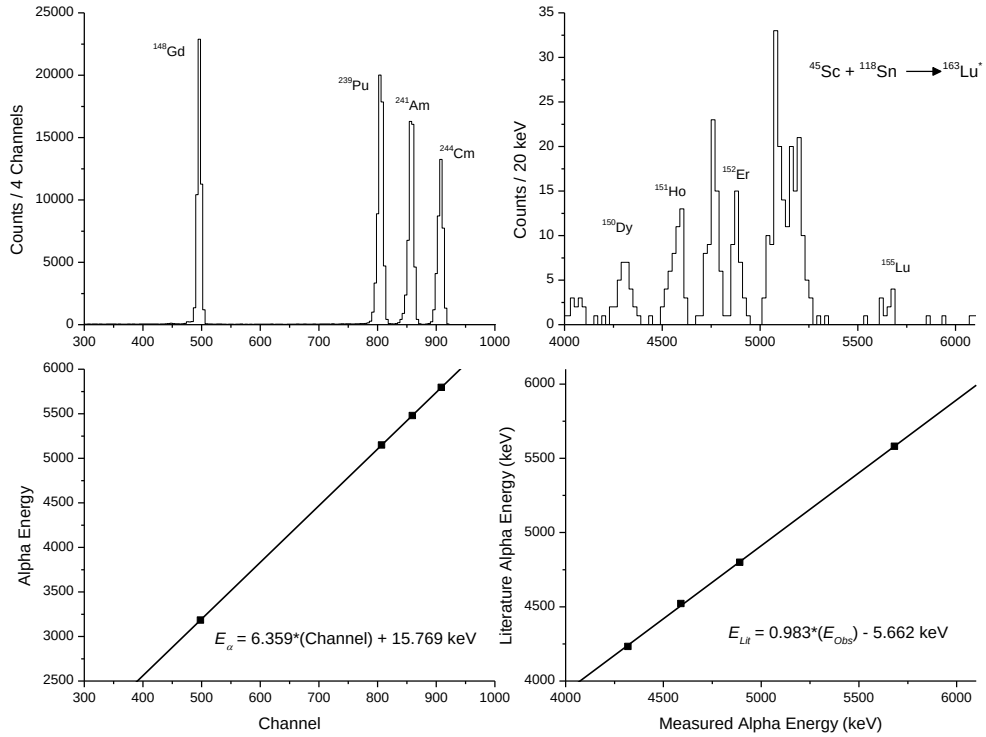

Figure 2.6. External and internal calibrations of the PSSD. The external calibration with the 4-peak α-particle source and associated fit are shown in the top left and bottom left, respectively. The internal calibration data and associated fit are shown in the top right and bottom right, respectively.

$$E_{Dep} = m_T(Channel) + b_T \ , \tag{2.17}$$

$$Pos_y = m_p(E_{Dep} / E_\alpha) + b_p \ . \tag{2.18}$$

The measured deposited energy in the strip, E_{Dep}, was determined and then converted into a vertical position, Pos_y, in millimeters. The quantities m_T, m_p, b_T, and b_p were all calibrated independently for each strip using the mask and a least-squares minimization. The horizontal position was not calibrated and was simply defined by the ~3-mm width of each strip.

The α-detection efficiency, ε_{detect}, was estimated to be (55 ± 3)% for the PSSD (meaning that ~ 45% of the α particles were emitted away from the PSSD and were not

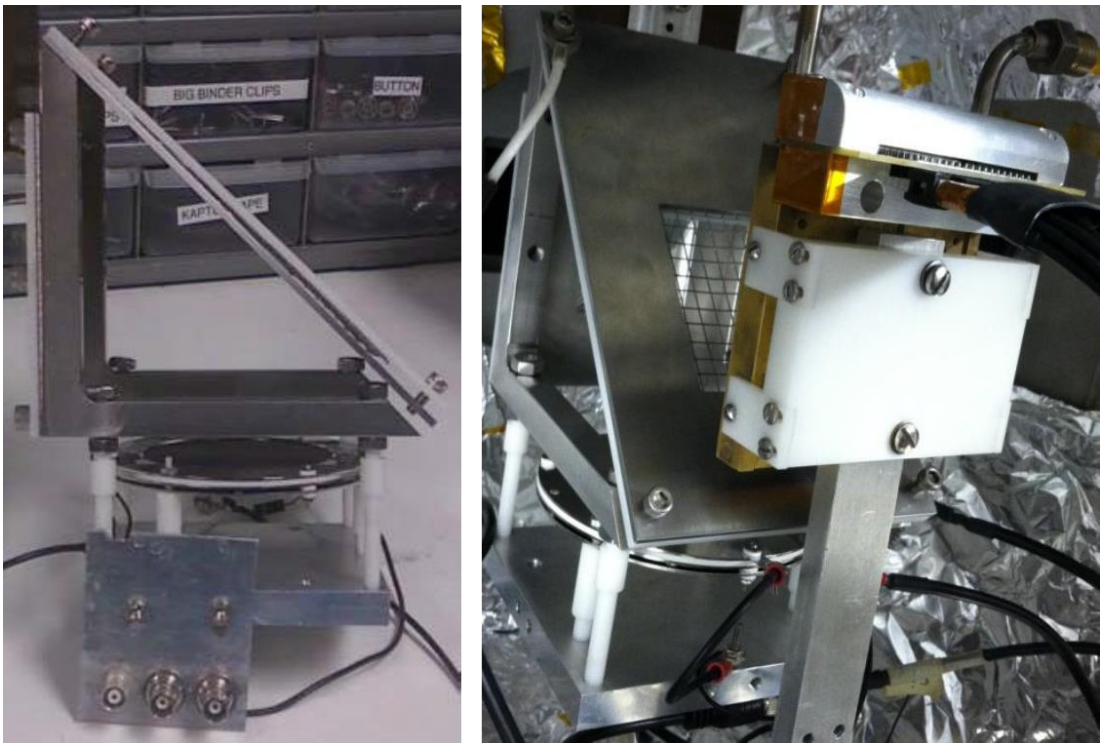

Figure 2.7. Pictures of the MCP Assembly. Left: Side view of the MCP detector assembly. The beam entered on the left-hand side of the picture and passed through the thin foil to create electrons which were steered onto the MCP detector. Right: The MCP detector and the PSSD assembled in the TC.

detected whatsoever). Due to the physical width of the EvR distribution entering the focal plane, it is likely that a small fraction of the EvRs that enter the DC did not impinge on the active area of the PSSD. The fraction of EvR distribution which struck the PSSD was estimated to be (100 ± 2)% in the horizontal plane and (95 ± 5)% in the vertical plane based on the observed position spectra during the experiments.

In addition to the PSSD, a microchannel plate (MCP) detector shown in Fig. 2.7 was located in the DC for all of the experiments in this work. The MCP detector was positioned directly upstream of the PSSD and served to discriminate implant events from α-decay events in the PSSD. A foil of 0.6 μm Al or 2 μm Ti was located perpendicular to the beam axis in the focal plane of the DC. As the EvRs passed through the foil, they knocked off electrons, which were then steered onto the MCP detector by the electrostatic grid shown in the figure. The grid typically had a bias of -100 V to steer the electrons onto the MCP detector. When the electrons encountered the surface of the MCP detector, they entered two plates with thousands of small channels etched into the surface. There, the electrons collided with the walls of the channels, knocking off more electrons in the process and creating an "electron cascade." The MCP detector used in these experiments had two plates arranged in a chevron configuration. The two plates of the MCP were typically biased to ~ +1400 V and ~ +1800 V. The average electron multiplication was ~10^6-10^7, and the signals from the MCP detector were fairly large. In the experiments, an EvR that passed through the foil and implanted into the PSSD would produce a signal in the MCP detector, while an α-decay event in the PSSD would not. Thus, the MCP detector was able to discriminate between these two types of events

occurring the PSSD. The MCP detector was originally developed by passing fission fragments from a ^{252}Cf source through the 2 μm Ti foil and measuring the response signal in the detector. With the fission fragments, the MCP had a discrimination efficiency of > 99% [86]. The MCP detector was relatively "noisy" – the detector sent out pulses with a frequency of about 1 Hz even when no radiation was impinging on it. As such it was not used to trigger the Data Acquisition System (see more on this in Section 2.5). Examples of the PSSD energy spectrum with and without event discrimination by the MCP detector are given in Fig. 2.8. Every time a candidate EvR event or *a*-decay event was recognized by the PSSD, a gate was created by the data acquisition system. The MCP detector signal was delayed, and if the MCP signal arrived while the gate was open, then the even was classified as an implant event. If no MCP detector signal arrived while the gate was open, then the event was classified as an α-decay event. The electrostatic grid shown in Fig. 2.7 had transmission efficiency of 85% which was factored into the EvR cross section calculations.

2.5 Data Acquisition System

The data acquisition system (DAQ) used in these experiments was a custom setup of electronics based on Nuclear Instrumentation Standard (NIM) electronics. The signals from each of the four detectors (two Rutherford scattering detectors, one PSSD, and one MCP detector) were processed through the NIM electronics and sent to the data analysis computer, where they were recorded and saved to a hard disc using the data

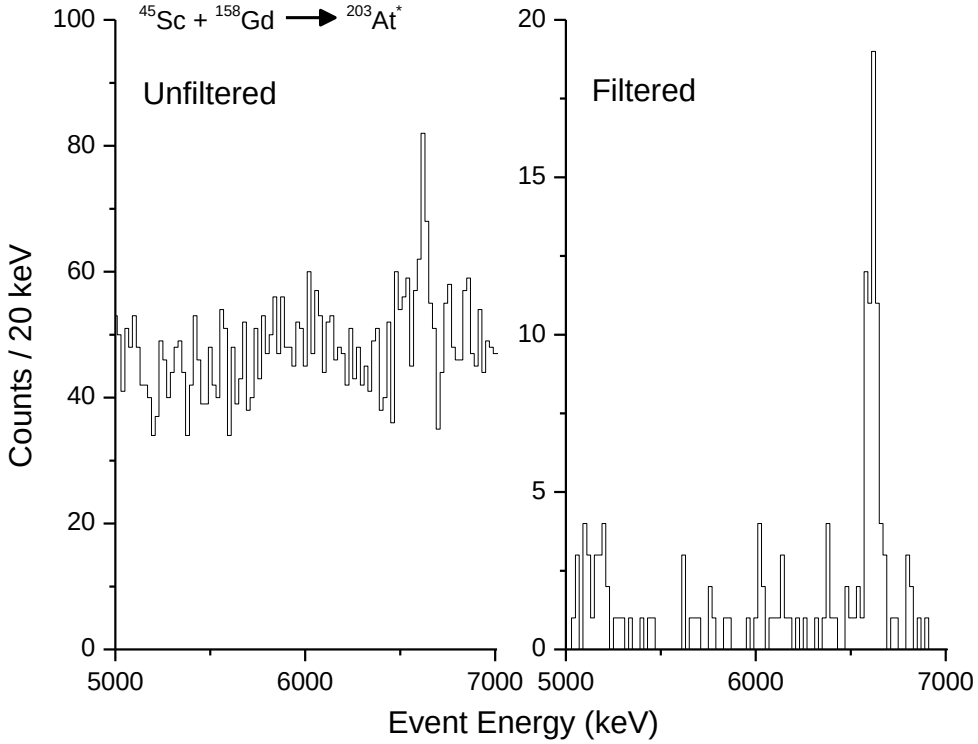

Figure 2.8. Example energy spectra before (left side) and after (right side) event discrimination was done with the MCP detector. These spectra were taken for the ^{45}Sc + ^{158}Gd reaction at $E_{Lab,\ CoT}$ = 195.3 MeV.

acquisition software. The software is based on the CYCApps framework, which in turn is based on the ROOT framework [87], and is modified specially for the number of detectors and electronics modules employed by our research group.

2.5.1 Signal Processing and Readout from the Radiation Detectors

The signals from the two Rutherford detectors, the MCP detector, and the PSSD were all fed into the DAQ. A simplified schematic of the paths that the detector signals took is presented in Fig. 2.9. The signals from the two Rutherford detectors were

amplified using Ortec model 142 preamplifiers (ORTEC, Oak Ridge, TN, USA) with a gain of 10 mV/MeV. The amplified signals were then shaped by a CAEN 16-channel model N568B amplifier (CAEN Technologies Inc., NY, USA). The full-energy signal from the PSSD was amplified by a charge sensitive pre-amplifier chip (Zepto Systems, Bloomington, IN, USA) with a gain of 7-8 mV/MeV and shaped by the same CAEN amplifier. The signal from the MCP detector was amplified by a Zepto System pre-amplifier chip and shaped by the same CAEN amplifier as the Rutherford detectors and the full-energy PSSD signal. The 16 signals from the position-sensitive strips were each amplified by an identical Zepto Systems pre-amplifier chip and shaped by a second CAEN amplifier of the same model as described above. The preamplifiers were powered by a 12V NIM power supply, while the amplifiers were powered by a standard NIM crate. Each CAEN amplifier had two outputs: one fast and one slow. The fast signal had a lower quality and was used to trigger the electronics system as will be described in Section 2.5.2. The slow ("shaped") signal provides a higher signal quality, and the shaped signal from each amplifier was passed into its own Mesytec model MADC-32 (Mesytec, Putzbrunn, Germany) 32-channel Analog-to-Digital Converter (ADC) housed in an SBS VME crate in our electronics rack. Each ADC measured the maximum pulse height from the shaped amplifier output (the "analog value") and converted it to a number (the "digital value"). The SBS VME crate also housed a PCI bus adapter module which connected to the data acquisition computer via a fiber-optical cable. The ADCs transmitted the digital output signal through the PCI bus into the data

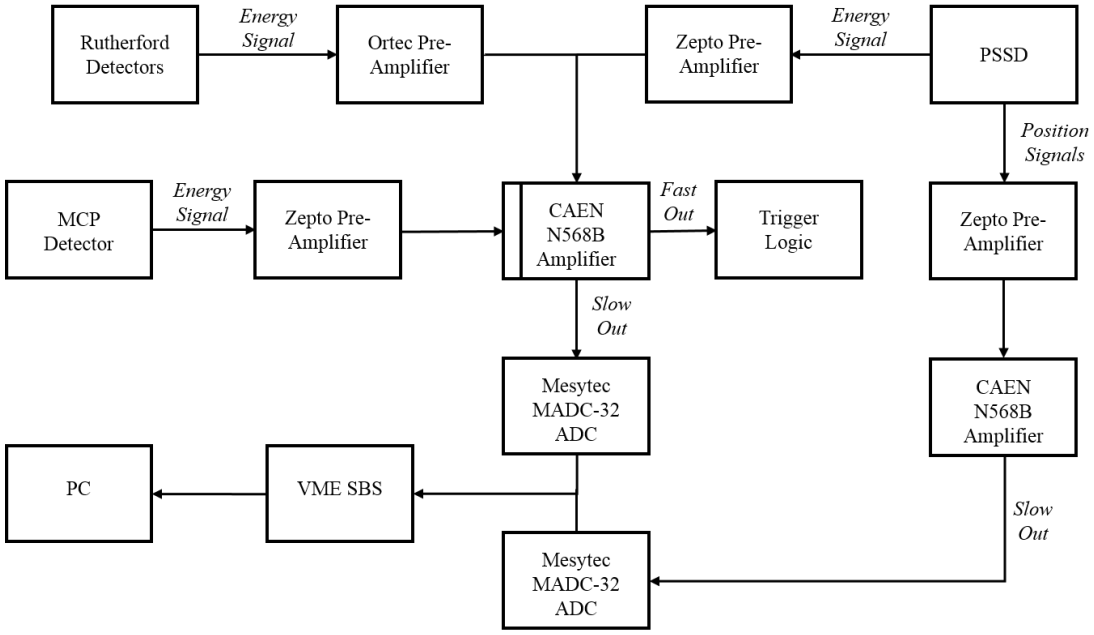

Figure 2.9. Simplified schematic of the detector signal processing pathways. Each detector signal was amplified by a pre-amp and shaped by an amplifier before being passed to the data acquisition computer. The "Trigger Logic" will be discussed in Section 2.5.2. The solid vertical line on the CAEN N568B Amplifier indicates that the Rutherford detectors and the PSSD were used to trigger the DAQ, but the MCP detector signal was not used in the trigger logic.

acquisition computer, where the energy and position values were stored and able to be viewed during and after the experiment.

2.5.2 Trigger and Logic Signal Pathways

In addition to amplifying, shaping, and recording the pulses from all four detectors, the DAQ also contained a number of NIM modules housed in NIM crates to properly trigger the electronics systems, to record the timing of the events, and to help

discriminate between different types of events in the detectors. A list of the important logic units is given in Table 2.2.

The first function of the logic units was to create the trigger signal for the system. If the DAQ was continuously accepting data, the amount of data recorded would be unnecessarily large. The trigger reduces the amount of data in the data stream by selectively telling the system to look for data at the right times. The system was triggered whenever a data event above the threshold set by the CAEN constant fraction discriminator (CFD) was seen by the PSSD or either of the Rutherford detectors. The trigger signal was created by the fast output of the CAEN amplifier and was passed into the CAEN CFD. After passing the CFD, the trigger signal entered the Phillips Fan-In/Fan-Out, where the signal was copied and sent to two places. The first trigger signal was sent to the CAEN scalar, which simply counted the total number of triggers while data was being collected. The second copy of the trigger was sent to the Phillips logic unit and finally to the Phillips gate generator, where the "gate signal" was created. After the gate signal was created, it was sent to another Fan-In/Fan-Out, where it was copied and passed to each ADC. This gate signal told the ADCs to begin collecting data, and the gate typically was open for a few microseconds. A second output from the logic unit was passed to the gate generator to create the "veto" signal, which told the DAQ to reject all incoming events while the gate was open. A VME CBD8210 branch driver created a "busy" signal which worked in tandem with the trigger logic to create the veto signal. Once the data event has been processed and recorded, the busy signal was stopped, and the DAQ was then ready to accept the next event. Because the system rejected data

Table 2.2. List of the important signal processing and logic modules used in the experiments.

Manufacturer	Model	Function
CAEN	N568B	16-Channel Spectroscopy Amplifier
	V560	Scalar
	V812	Constant Fraction Discriminator
	V977	I/O Register
Phillips Scientific	755	Quad Four-Fold Logic Unit
	757	Mixed Logic Fan-In/Fan-Out
	794	Quad Gate and Delay Generator
Mesytec	MADC-32	Peak-Sensing Analog-to-Digital Converter
Ortec	566	Time-to-Amplitude Converter
	935	Constant Fraction Discriminator

while the gate was open, a small portion of the events were not recorded. To quantify the event loss, a pulse generator created a 1 MHz time signal which was used to put a time stamp on every event. The "live time" of the system was then calculated by dividing the number of seconds that the system was active by the total number of seconds elapsed. Live times were typically >99% for the experiments in this work.

The second major function of the logic units was to help distinguish between event types. This was done with the two time-to-amplitude converters (TACs); the TACS converted time differences between events into amplitudes which were measured

and recorded. The cyclotron RF TAC was “started” by the fast amplifier output of any PSSD or Rutherford detector event and was “stopped” by the delayed cyclotron RF signal. The MCP TAC was started by the PSSD fast output and was stopped by the delayed MCP energy signal. A simplified schematic of the TAC signal logic is shown in Fig. 2.10. The cyclotron RF TAC provided information on the timings of the Rutherford scattering events relative to the cyclotron RF timing. The MCP TAC provided information that helped discriminate between implant events and EvR decay events. As discussed, an implanting EvR produced signals in both the PSSD and MCP detector. These events occurred within tens of nanoseconds of each other and produced a time signal in the TAC. An EvR decay event did not result in coincident events, and the TAC would simply time out without recording a signal.

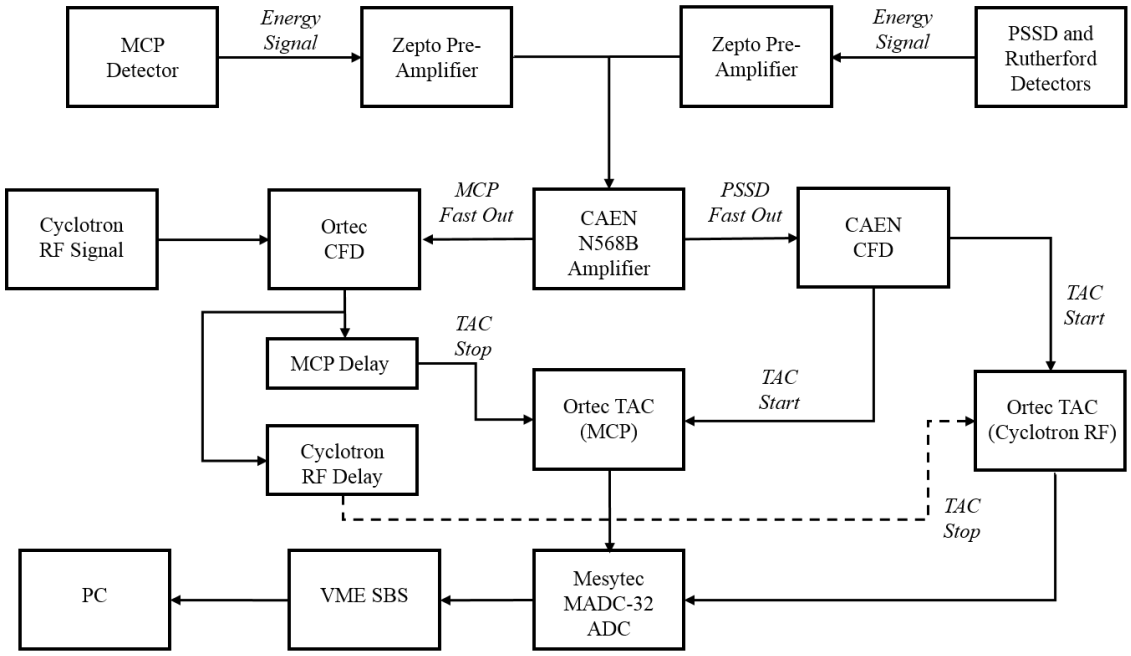

Figure 2.10. Signal pathways for the two TAC modules used in the experiments. The TACs were used to aid in event discrimination and timing. The line from the Cyclotron RF Delay to the Ortec TAC is dashed simply for the purpose of clarity.

2.6 Data Analysis Techniques

The experimental data were thoroughly analyzed using an offline analysis code, and the results are reported in Sections IV and V. The theoretical calculations used to model the data are fully explained in Section III. However, there were a few notable data analysis techniques that should be mentioned in this Section.

2.6.1 Background Fitting with GF3

Even with the use of the MCP detector to discriminate between EvR implant events and α-decay events, the α-particle energy spectra were still contaminated sparsely with background events. These events likely included scattered protons or α particles that were ejected from the target with just the right angle and momentum to be steered through MARS and into the focal plane. These light particles did not create enough signal in the MCP detector to register as an implant event, so they were sorted into the α-particle energy spectrum. Although the rate of these background events was small, the event rate for α-decay events in the PSSD was also small in many cases. Thus, a background subtraction was performed for all of the α-energy spectra measured in this work. The raw α-energy data were exported from the data acquisition software into the GF3 program that is part of the RADWARE software package [88]. The RADWARE package originated as a suite of programs designed to analyze γ-ray coincidence data, and the GF3 program was specifically designed to manipulate, fit, and analyze 1-Dimensonal spectra

such as the α-energy spectra studied here. The GF3 program is able to fit up to 15 peaks on a given spectrum with a polynomial background (the order of the polynomial can be as high as 2, a quadratic function). The backgrounds of the α-energy spectra collected in these experiments were fit with a zeroth-order polynomial function (because the backgrounds were small, they were able to be fit with a constant background over a large energy range). The peak-fitting part of the procedure was done with standard parameters for the peak centroid, width and height. The peak-fitting procedure determined the best fit for the constant background plus the centroids and areas of the peaks within the selected area. These background fits were subtracted from the observed number of EvR decay counts in all of the α-energy spectra collected in this work.

2.6.2 Rejection of Peaks Based on the Background Counts

As described above, there existed a small background underneath the peaks in the measured α-energy spectra. Due the very low statistics observed for some of the reaction channels, it was possible that the observed "decay peaks" could instead be background events. To address this problem, a simple statistical test was developed to prevent "peaks" consisting of only background events from being considered as actual EvR decay peaks. First, a region of interest (ROI) was determined for each possible reaction product based on the α-particle energy and the resolution of the PSSD. For example, the reaction product ^{199}At (which is an EvR for multiple reactions studied in this work), the literature α-particle energy is 6643 ± 3 keV [29]. Based on the known PSSD resolution

of ≈ 60-80 keV and the measured α-energy spectra, the ROI for this nuclide was set to be 6590-6690 keV. After the ROI for each nuclide was set, the background for each ROI, μ, was determined by multiplying the average background per bin (which was determined by the GF3 background fit) by the width of the ROI in bins. In the example above, the "bin width" of the ROI was 5 bins.

Due to the low event rates in this work, a Poisson distribution was used to model the background event distribution, and the statistical test is identical to that described in [89]. The number of background counts, μ, in each ROI was determined as described above. The cumulative Poisson probability of observing *j* background counts when μ are is expected is calculated with the following equation:

$$\sum_{j=0}^{n} P\left(j \mid \mu\right) = \sum_{j=0}^{n} \frac{\mu^{j}}{j!} e^{-\mu} \quad . \tag{2.19}$$

The smallest number of counts which was accepted as a real peak, *n*, was then determined by the smallest value of *n* which satisfied the following inequality:

$$\sum_{j=0}^{n} \frac{\mu^{j}}{j!} e^{-\mu} \geq \varepsilon \tag{2.20}$$

Thus, the peak was accepted if the number of counts in the peak was greater than or equal to *n*. The confidence level, ε, in this work was set to be 95%, meaning that the probability that a reported peak being mistaken for only background counts was only 5%. In practice, many of the EvR peaks were well above the background and the likelihood of mis-reporting a peak was even smaller.

3. THEORETICAL MODEL

To enhance our understanding of the physical factors which determine the evaporation residue cross sections, a theoretical model was developed and applied to the reactions studied in this work. The model was identical for both the ^{45}Sc- and ^{44}Ca-induced reactions. The model was based on the assumption that a fusion-evaporation reaction can be separated into three independent steps: the capture of the projectile-target system, the formation of the equilibrated compound nucleus, and the deexcitation of the compound nucleus into the cold evaporation residue. The cross section for producing an evaporation residue, first presented as Eq. (1.1), can be expanded to include the energy and angular momentum dependences of each stage of EvR formation:

$$\sigma_{EvR} = \sigma_{capt}(E_{cm}, l) P_{CN}(E_{cm}, l) W_{sur}(E^*_{CN}, l_{CN}) \ , \qquad (3.1)$$

where $E_{cm.}$ is the kinetic energy of the projectile in the center-of-mass frame of reference, l is the angular momentum brought into the reaction by the projectile-target interaction, E^*_{CN} is the initial excitation energy of the compound nucleus, and l_{CN} is the angular momentum of the compound nucleus. This section describes how each of the three stages of the theoretical model were calculated.

3.1 The Capture Cross Section

In simplistic terms, the initial interaction of the projectile nucleus with the target nucleus can be viewed as two positively charged spheroids traveling towards each other

in space as time elapses. As the two charges approach each other, the Coulomb repulsion energy increases until the two spheres overcome the Coulomb barrier and reach a "touching" configuration (see Fig. 3.1 for a depiction). When the system has reached this state, the projectile and target have been "captured". The cross section for the system reaching this capture configuration depends on the projectile and target nuclei physically encountering each other. In a classical approach, this interaction cross section can be calculated from the cross-sectional areas of the projectile and target:

$$\sigma_{interaction} = \pi(r_p + r_t)^2 = \pi r_0^2 (A_p^{1/3} + A_t^{1/3})^2 = \pi R^2 \ , \tag{3.2}$$

where r_p and r_t are the radii of the projectile and target nuclei, respectively. The radius of a nucleus is calculated using $r = r_0 A^{1/3}$, where $r_0 \approx 1.2$ fm and A is the mass number of the nucleus. The radius of the system in capture, R, is simply calculated as the sum of r_p and r_t. Eq. (3.2) above forms the basis for calculating the capture cross section, σ_{capt}. For the system to reach the capture configuration, the offset of the projectile and target nuclei must be small. This distance, which is known as the impact parameter, b, is depicted in Fig. 3.1. In this simplified schematic, if the projectile impinges on the target with sufficient energy in the area between the dashed lines, then the capture configuration will be reached. If b is too large, then the Coulomb repulsion will push the two nuclei away from each other in a "scattering" event. These scattering events were useful during the experiments (some were measured by the Rutherford detectors described in Section 2.3), but these events do not lead to the formation of an EvR. Additionally, larger values of b result in larger values of the angular momentum, l. If l is sufficiently large, the rotational energy will overcome the attractive nuclear force, and

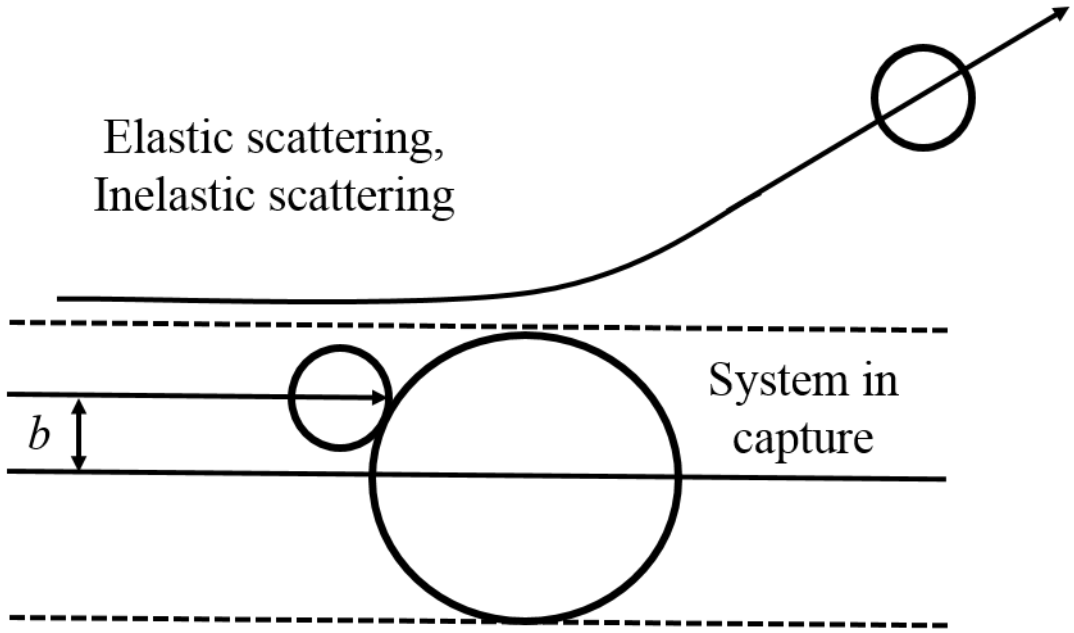

Figure 3.1. Simple schematic of the capture process. The projectile comes in from the left-hand side and interacts with the stationary target. Projectiles within the dashed lines will overcome the Coulomb repulsion and result in capture, while projectiles that impinge farther away from the target will be scattered.

the system will re-separate. The re-separation of the projectile and target will be discussed in detail in Section 3.2.

For a charged-particle-induced reaction, a semi-classical expression for σ_{capt} can be written as such [32]:

$$\sigma_{capt} = \pi R^2 \left(1 - \frac{B}{E_{cm}} \right) , \tag{3.3}$$

where R is the same as defined in Eq. (3.2), E_{cm} is the same as defined in (3.1), and B is the Coulomb barrier. B is commonly calculated as such for two point charges approaching one another:

$$B = \frac{e^2}{4\pi\varepsilon_0} \frac{Z_p Z_t}{R} , \tag{3.4}$$

where Z_p and Z_t are the atomic numbers of the projectile and target, respectively. Eq. (3.3) states that if $E_{cm} < B$, then capture is forbidden and σ_{capt} is assumed to be zero. However, due to the quantum-mechanical nature of nuclei, the projectile can tunnel through the Coulomb barrier and reach the capture configuration even when $E_{cm} < B$. This "sub-barrier" fusion has been observed for many reaction different reaction systems and extends to energies well below the Coulomb barrier [44, 90, 91].

To describe the capture process in a full quantum-mechanical framework, the quantized nature of l can be used. The target can be divided into circular zones, as shown in Fig. 3.2 and projectiles colliding anywhere within a given zone will result the same angular momentum. The cross section for each zone can be written as:

$$\sigma_l = \pi \lambda\!\!\!^{-2} \left[(l+1)^2 - l^2 \right] = \pi \lambda\!\!\!^{-2} (2l+1) = \frac{\pi \hbar^2}{2\mu E_{cm}} (2l+1), \tag{3.5}$$

where $\lambda\!\!\!^{-}$ is the reduced de Broglie wavelength of the projectile and μ is the reduced mass of the projectile-target system. The total capture cross section can then be written by summing over all l:

$$\sigma_{capture} = \frac{\pi \hbar^2}{2\mu E_{cm}} \sum_{l=0}^{\infty} (2l+1) T_l \, . \tag{3.6}$$

As the values of the impact parameter increase, so do the values of l. As stated, once the reaction has a sufficiently high value of b, the capture process is no longer likely, and scattering is the dominant process. The transmission coefficient, T_l, in Eq. (3.6) describes this cut off. The value $l_{max} = R/\lambda\!\!\!^{-}$ is the maximum achievable value of l, and T_l

cuts off values of angular momenta which are greater than l_{max} (i.e. $T_l = 1$ for $l \leq l_{max}$, and $T_l = 0$ for $l > l_{max}$).

In addition to the quantum-mechanical effects, other factors must be accounted for when trying to realistically calculate σ_{capt}. One such factor is the orientation of the projectile and target when they interact. Depending on the reaction system, the projectile nucleus, target nucleus, or both may be deformed. A schematic for a spherical projectile nucleus interacting with a prolate target nucleus is shown in Fig. 3.3. When the target is

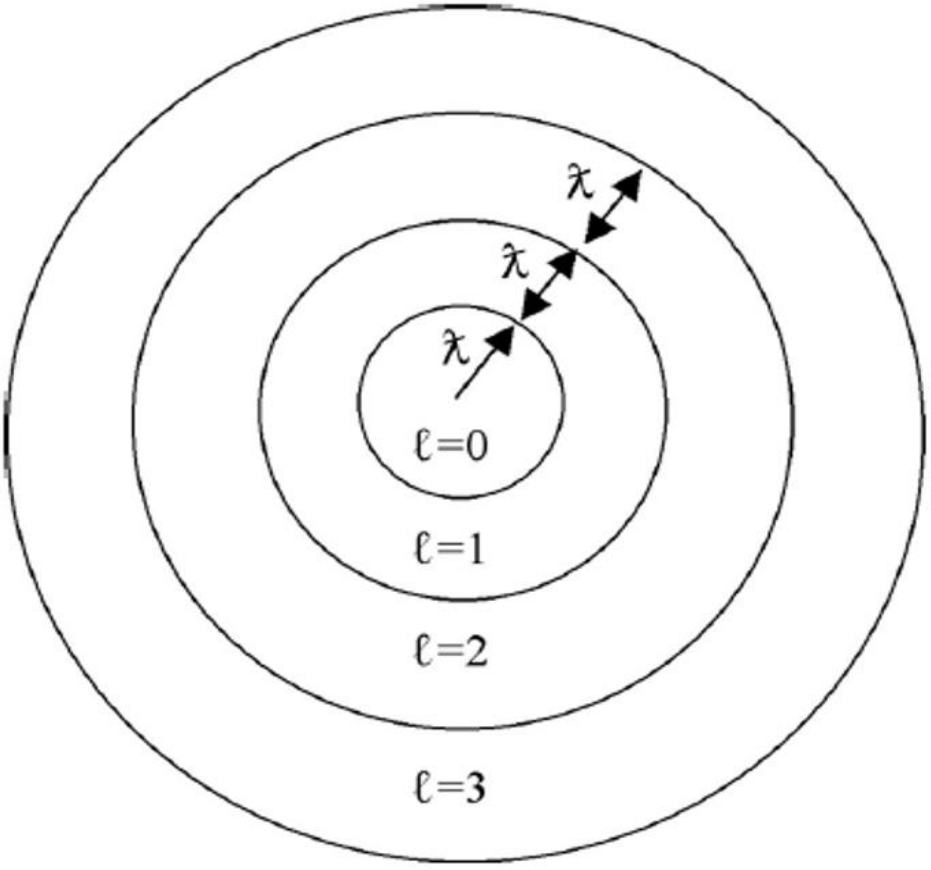

Figure 3.2. Simplified quantum-mechanical schematic of the target nucleus. A collision anywhere within a given zone will result in the same value of *l*. Figure reproduced with permission from [32] © 2006 John Wiley & Sons, Inc.

oriented such that the projectile interacts with the short axis of deformed nucleus, as shown on the left side of Fig. 3.3, then the Coulomb barrier is larger than when the target interacts with the long axis of the target, as shown on the right side of Fig. 3.3. Since the projectile can interact with the target in *any* orientation, a "distribution of barriers" is created. This situation is even more complex when both the projectile and target are deformed. This effect also helps account for some of the sub-barrier fusion that is observed but not accounted for in a "single barrier" formula such as Eq. (3.3). Other important effects that are considered for sub-barrier fusion calculations include neutron transfer channels between the projectile and target [92] and low-lying collective excitations [93].

Several options are available when attempting to perform a realistic calculation of σ_{capt}. One option is to use a fully quantum-mechanical code such as CCFULL [26]. The bases of the CCFULL code are Eq. (3.6) and the wavefunctions which describe the nuclear motion. A standard form of the Woods-Saxon potential is used to describe the attractive nuclear force, and a standard electrostatic point-charge repulsion defines the Coulomb repulsion. Experimental evidence has shown that there is a strong coupling between the motion of two colliding nuclei to their intrinsic nuclear motions (such as rotation and vibration) [94]. These interactions enhance the likelihood of tunneling through the barrier and reaching the capture configuration, and CCFULL fully defines the couplings.

The equations which define the interaction between the relative motion and the intrinsic motions are solved using numerical methods, and solving the Schrodinger

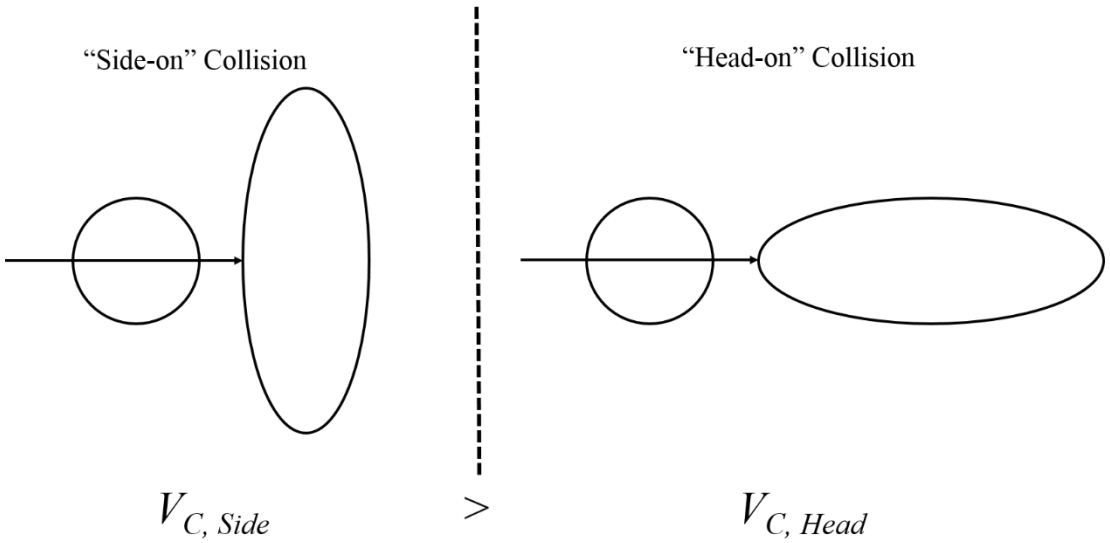

Figure 3.3. Simplified schematic of a spherical projectile interacting with a deformed target in a "side-on" collision (left) and a "head-on" collision (right). The repulsive Coulomb force felt by the system in a side-on collision is larger than in the head-on collision.

equation allows for the calculation of the σ_{capt} and the average angular momentum of the compound nucleus ($l_{CN,\,avg}$). The CCFFULL code was designed to work best for reaction systems where the sum of the charges of the projectile and target, $Z_p + Z_t > 12$, and charge product, $Z_pZ_t < 1800$. The code also models σ_{capt} at energies both above and below the Coulomb barrier. Examples of CCFULL capture calculations are shown in Fig. 3.4.

The actual values of σ_{capt} for the theoretical model in this dissertation were calculated using the semi-empirical "sticking" formula of Świątecki et al. [27]. This method has been shown to work well for heavy-ion-induced reactions such as the ones studied in this work. The formula for calculating σ_{capt} is:

$$\sigma_{capt} = \pi R^2 \frac{\nu}{2E_{cm}} \left[X(1 - erf(X)) + \frac{1}{\sqrt{\pi}} \exp\left(-X^2\right) \right], \tag{3.7}$$

$$X = (E_{cm} - B)/\nu . \tag{3.8}$$

In the above equations, $R = 1.16\, fm\left(A_p^{1/3} + A_t^{1/3}\right)$, and B is the mean interaction barrier:

$$B = 0.85247z + 0.001361z^2 - 0.00000223z^3 , \tag{3.9}$$

where z in Eq. (3.9) is a Coulomb parameter defined as

$$z = \frac{Z_p Z_t}{A_p^{1/3} + A_t^{1/3}} . \tag{3.10}$$

The formula of B in Eq. (3.9) was determined by fitting a data set of 45 different barriers measured from reactions that ranged from ^{40}Ca + ^{40}Ca up to ^{40}Ca + ^{194}Pt. The "distribution of barriers" was introduced through ν, the Gaussian range parameter:

$$\nu = CB\sqrt{W_p^2 + W_t^2 + W_0^2} , \tag{3.11}$$

where C = 0.07767 fm^{-1} is an adjustable parameter that was determined by experimental fit and W_0 = 0.41 fm is a parameter designed to account for minor shape effects, such as nuclear vibrations. The parameters W_p and W_t are the mean distributions of the radius vectors which specify the surfaces of the projectile and target, respectively. These two parameters are calculated for the projectile and targets using the formula

$$W_i = \frac{R_i \beta_{2,i}}{\sqrt{4\pi}} , \tag{3.12}$$

where the subscript i denotes either the projectile or target, $R_i = 1.14\, fm A_i^{1/3}$ is the radius and $\beta_{2,t}$ is the quadrupole deformation parameter. The parameters C and W_0 were

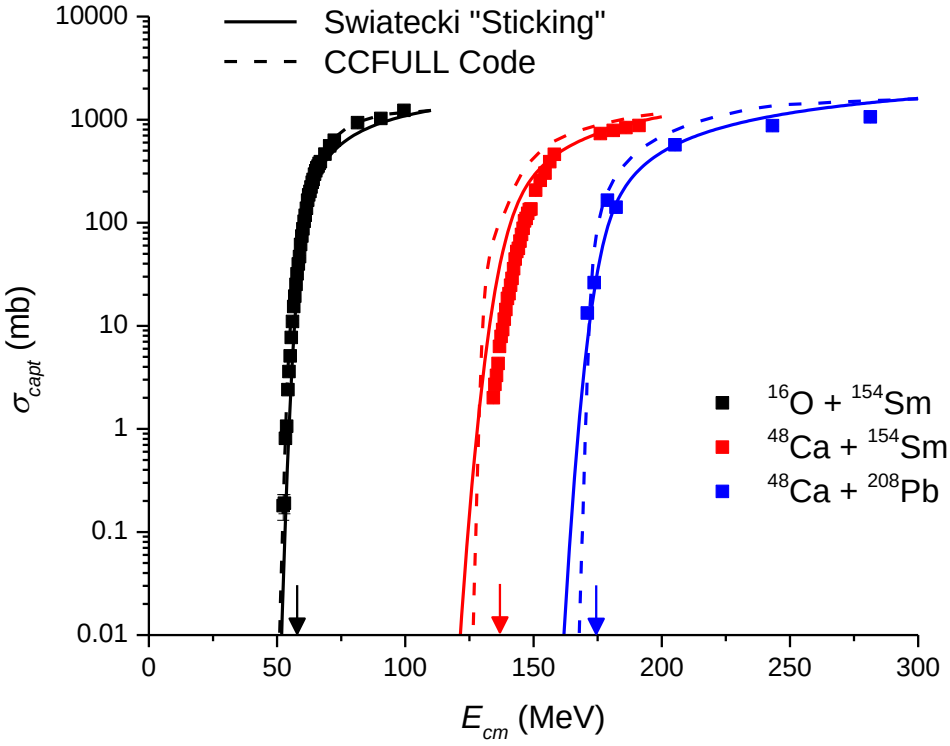

Figure 3.4. Capture cross sections calculated for three reaction systems that produce CN with $70 \leq Z \leq 102$. The squares are experimental data, the solid lines were calculated using Eq. (3.7), and dashed lines were calculated with CCFULL. The ^{16}O + ^{154}Sm data (black squares) were taken from [95], the ^{48}Ca + ^{154}Sm data (red squares) were taken from [3], and the ^{48}Ca + ^{208}Pb data (blue squares) were taken from [96]. The arrows indicate the positions of the Coulomb barriers calculated using Eq. (3.9).

determined by fitting v to the same set of 45 experiments that were used to determine the fit for Eq. (3.9).

The calculations with the "sticking" formula were compared with experimental data and with CCFULL calculations. The results are presented in Fig. 3.4, and good

agreement between the data and both sets of calculations was observed over a wide range of reactions. Overall, the error in the calculation for the capture cross section is estimated to be a factor of 2.

3.2 The Compound Nucleus Formation Probability

After the system reaches the capture configuration, the nucleons from the projectile and target mix, and the nuclear strong force holds the newly-formed CN together. However, there is a certain probability that, before an equilibrated CN is formed, the rotating di-nuclear system re-separates into two heavy fragments in a fission-like process. This process has been termed "quasifission" [97, 98], and occurs on a very short time scale ($\approx$ 1 zs = 10^{-21} s). The quasifission phenomenon was first observed in the 1970's through the measurement of the angular distribution of fission fragments in heavy-ion induced reactions [99]. The other common observables used to measure the quasifission probability are the energy distribution and the mass-angle distribution of fission fragments from heavy-ion induced reactions. A simple schematic showing the competition between quasifission and CN formation is presented in Fig. 3.5.

The probability that quasifission occurs as a system transitions from the capture configuration to the CN depends strongly on the charge product, Z_pZ_t, of the reacting system [100]. For small values of Z_pZ_t, the system in capture will always result in CN formation (P_{CN} = 1) [100]. For those reaction systems, large values of b will result in scattering events. However, as Z_pZ_t increases, the quasifission probability increases and

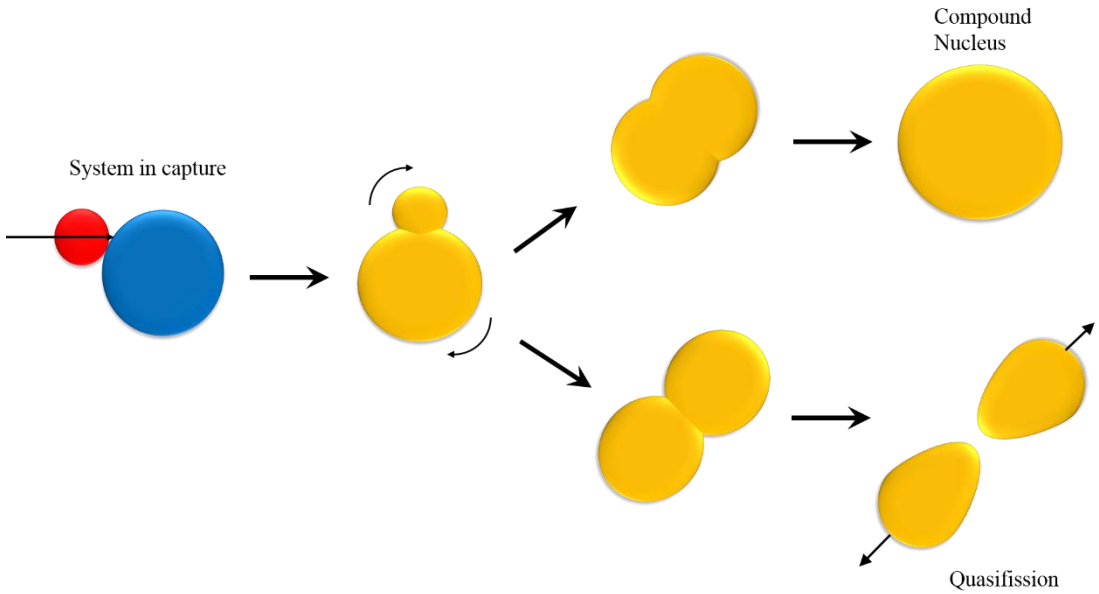

Figure 3.5. Depiction of the two possible paths from the system in capture. If the nucleons mix and are held together by the nuclear strong force, the CN is formed. If the rotational energy of the system overcomes the strong force, the two fragments undergo quasifission.

P_{CN} decreases. Early research suggested that quasifission only occurred in reactions systems with large Z_pZ_t, and theoretical calculations suggested that the onset of quasifission would occur at $Z_pZ_t > 1600$ [101]. However, it has since been shown that quasifission can inhibit CN formation for reactions with Z_pZ_t as low as 540, and ample evidence exists that shows quasifission onsets somewhere between Z_pZ_t = 540-1000 for reactions of projectiles on deformed targets [46, 100, 102, 103]. The reactions studied in this work used a spherical projectile to bombard a deformed target and have $Z_pZ_t > 1300$; quasifission will certainly inhibit CN formation for these reactions.

A qualitative understanding the dynamics of quasifission can be made by considering the potential energy surface of the reacting system in terms of its deformation. An example is plotted in Fig. 3.6 for three reactions which lead to the ^{216}Th

CN. The abscissa shows the mass asymmetry of the projectile-target system: a value of 1 means that all the mass has been transferred into a single nucleus (CN formation has occurred), and a value of 0.5 means that the mass has been distributed among two equal fragments (symmetric quasifission). The ordinate is the relative potential energy of the reacting system, and the system naturally moves to a smaller potential energy. For the heavier reaction systems (^{30}Si + ^{186}W and ^{19}F + ^{197}Au) shown in Fig. 3.6, the initial mass asymmetry of the system in capture is to the left of the maximum potential energy, and the system will naturally follow the potential energy surface to the left (quasifission). For the lighter reaction system (^{12}C + ^{204}Pb), the mass asymmetry parameter in the capture configuration is to the right of the maximum of the potential energy surface, and the system will move toward CN formation. This is a qualitative description, and various models have attempted to quantify P_{CN} with either a semi-empirical fit to experimental data [104] or with time-dependent Hartree-Fock calculations [105]. However, P_{CN} remains the least-studied and most-uncertain stage of EvR formation.

In this work, P_{CN} was calculated using the semi-empirical formula of Siwek-Wilczyńska *et al.* [106]. To determine this formula for P_{CN}, a set of 28 heavy-ion induced reactions which exhibited characteristics of quasifission were considered. The value of P_{CN} for each reactions was determined by rearranging Eq. (3.1)

$$P_{CN} = \frac{\sum \sigma_{EvR}}{\sigma_{capt} \sum W_{sur}}, \tag{3.13}$$

where the numerator is the sum of *measured* EvRs, and the denominator is the product of the *calculated* capture cross section and the *calculated* EvR survival probabilities. The values of σ_{capt} were calculated using Eq. (3.7), and the values of W_{sur} were calculated

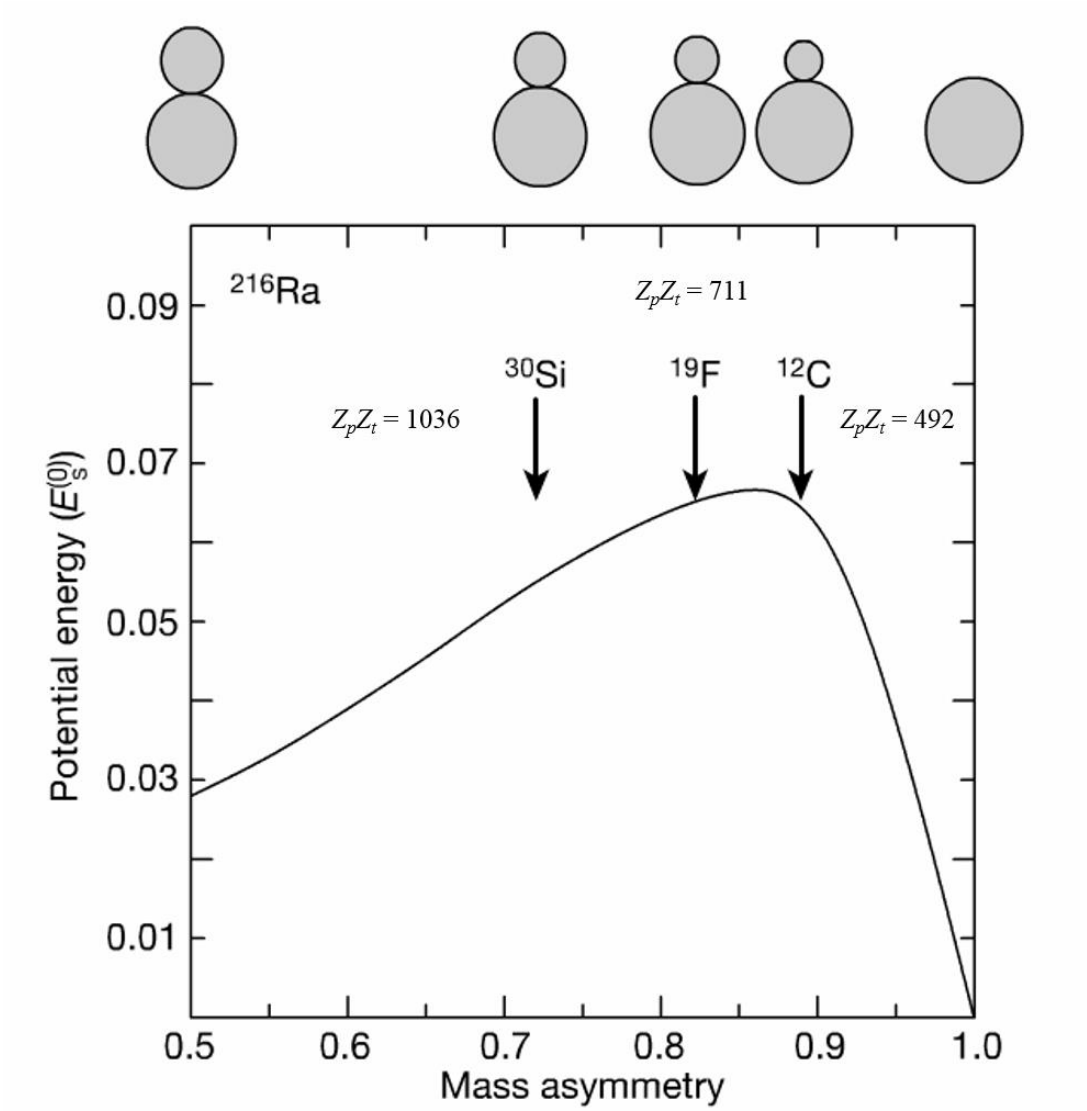

Figure 3.6. Qualitative understanding of the quasifission process for three reactions which form the ^{216}Ra CN. A mass asymmetry value of 0.5 represents two fission fragments of identical mass, while 1.0 represents the CN. The ^{12}C-induced reaction follows the potential energy surface to the right and forms a CN, while the heavier reaction systems move toward fission. Figure used with permission from [100].

using the model described in [64]. After P_{CN} was determined for each of the 28 reaction systems using Eq. (3.13), the data were plotted against the Coulomb parameter, z, as defined in Eq. (3.10) to show how P_{CN} varies with Z_pZ_t. These plots were done for two beam energies, one at the Coulomb barrier and one above the Coulomb barrier, and the results are presented in Fig. 3.7. The equations of best fit were determined to be:

$$P_{CN} = 10^{-(z/b)^k}, \tag{3.14}$$

where $k \approx 3.0$ and b is the linear interpolation which determines how P_{CN} varies with excitation energy

$$b = 2(E_{cm} - B)/MeV + 135. \tag{3.15}$$

In Eq. (3.15), B is the Coulomb barrier and was calculated using Eq. (3.9). To achieve the most realistic values of P_{CN} for the reactions being studied in this work, Eq. (3.14) was fit to experimentally measured values of P_{CN} in ^{48}Ca-induced reactions on deformed targets [3, 107]. This procedure was detailed in [50], and it was found that an empirically-determined parameter was needed to best fit the data:

$$P_{CN} = \zeta \text{ x } 10^{-(z/b)^k}. \tag{3.16}$$

The best-fit value of ζ was determined to be $\zeta = 2.5$. Unfortunately, no experimental measurements of P_{CN} with ^{45}Sc or ^{44}Ca projectiles have been reported, and the data with ^{48}Ca projectiles is the most similar data to the current work. The parameter of $\zeta = 2.5$ was used for every reaction studied in this work. The value P_{CN} must be ≤ 1, and the values of P_{CN} as calculated by Eq. (3.16) were limited to satisfy this criterion when necessary. The formation of the compound nucleus formation is the most uncertain

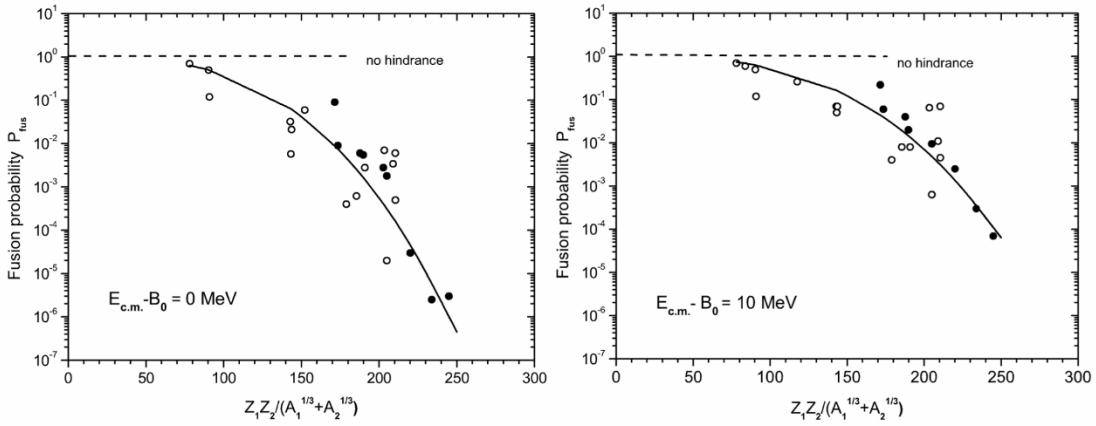

Figure 3.7. Results of the semi-empirical fitting procedure to determine formulas for P_{CN}. The solid lines are the best-fit lines to the experimental data. The left-hand side is the fit when E_{cm} is equal to the Coulomb barrier, and the right hand side is the fit when E_{cm} is 10 MeV above the Coulomb barrier. Figure used with permission from [106].

factor in Eq. (3.1). The error in the P_{CN} calculations was estimated to be approximately a factor of 10 [28].

3.3 The Survival Probability

The final step in the fusion-evaporation reaction is the deexcitation of the compound nucleus via the emission of particles and γ rays until the ground state evaporation residue is formed. Once the CN has equilibrated, all of the excitation energy has been evenly distributed among all the protons and neutrons in the CN. For a particle to be emitted, the stochastic (random) motions of the nucleus must eventually impart enough energy to a single particle to overcome the emission barrier for that particle. Due to this strong requirement, the timescales for emitting a particle from the CN, and thus the lifetime of the CN itself, are relatively long (typically $\approx 10^{-16}$ s [32]). The excitation

energies of CN, E^*_{CN}, ranged between 39-70 MeV for the ^{45}Sc- and ^{44}Ca-induced reactions studied in this dissertation, and it was observed that 3-6 particles were emitted from the CN. At each step of the de-excitation process, fission is in competition with particle emission until E^*_{CN} is below the fission barrier and particle emission barriers. At this point, γ-ray emission occurs until the EvR reaches the ground state. A simple schematic of the competition between fission and particle emission is presented in Fig. 3.8.

Due to the high density of levels in the excited CN, a statistical model is commonly used to describe the competition between fission and particle emission and calculate the survival probability, W_{sur}. The survival probability for the *xn* exit channels was calculated as:

$$W_{sur,xn} = P_{xn}(U_{CN}) \prod_{i=1}^{x} \left(\frac{\Gamma_n}{\Gamma_{tot}} \right)_i . \tag{3.17}$$

In Eq. (3.17) above, $P_{xn}(U_{CN})$ is the "Jackson Factor" [108], which determines the probability of emitting exactly *x* neutrons when given an initial "thermal excitation energy", U_{CN}. The index *i* denotes the step in the de-excitation process; for example, the quantity $\Gamma_{n,1}/\Gamma_{tot,1}$ is the probability of emitting a neutron in the first step. The probability of emitting a neutron at each step was calculated by dividing the decay width for neutron emission, Γ_n, by the total decay width, Γ_{tot}, where Γ_{tot} is the sum of all possible outcomes of a deexcitation step. A good approximation for calculating Γ_n/Γ_{tot} has been to consider *only* neutron emission and fission competition. This led to the well-known Vandenbosch-Huizenga formula for Γ_n/Γ_f [109]. For the ^{45}Sc- and ^{44}Ca- induced

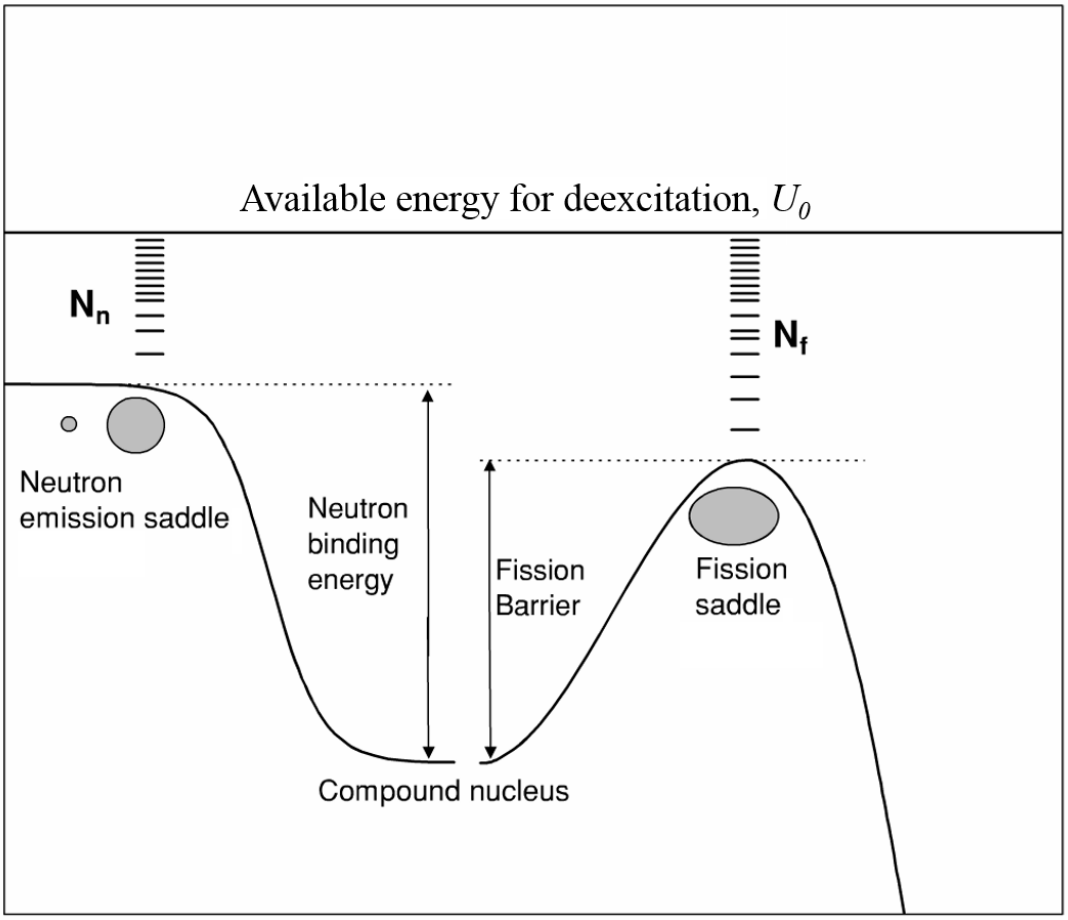

Figure 3.8. Competition between neutron emission and fission from the excited CN showing the respective barriers which must be overcome for the processes to occur. The levels above the barriers represent the level density of the daughter nucleus and the fission saddle, respectively. Once U_0 is below the neutron and fission barriers, γ rays will be emitted until the cold EvR is formed. Figure used with permission from [110].

reactions studied in this work, proton emission effectively competed with neutron emission, which is opposite to what was observed in the ^{48}Ca-induced reactions studied in Ref. [50]. Additionally, it was observed that α particles were emitted from the CN produced in the ^{45}Sc + ^{162}Dy reaction. Therefore, it was necessary for the model used in this work to include charged particle emission from the CN. The quantity Γ_{tot} was

calculated by including neutron emission, proton emission, α-particle emission, and fission (discussed below):

$$\Gamma_{tot} = \Gamma_n + \Gamma_p + \Gamma_\alpha + \Gamma_f \,. \tag{3.18}$$

In addition to calculating W_{sur} for the neutron-evaporation channels, the proton-evaporation channels were also studied by the theoretical model. It was observed in the experimental data that the only one proton was emitted from the CN, and the proton was accompanied by the emission of x neutrons, where x = 2-5. To calculate W_{sur} for the *pxn* reactions, it was assumed that the proton was the first particle emitted from the CN. This assumption is not perfect, but experimental data suggest that the proton is most likely to be emitted first. Then, the remaining particles emitted from the CN were all neutrons. The Jackson factor was also modified to account for the emission of the proton. The expression for W_{sur} in the *pxn* reactions was written as such:

$$W_{sur,pxn} = P_{pxn}(U_{CN})\left(\frac{\Gamma_{p,1}}{\Gamma_{tot,1}}\right)\prod_{i=2}^{x}\left(\frac{\Gamma_n}{\Gamma_{tot}}\right)_i \,, \tag{3.19}$$

where the index "1" on Γ_p/Γ_{tot} indicates that proton emission was the first step in the deexcitation process.

The individual decay widths for the particles, Γ_i and the fission width, Γ_f were calculated using the formulas of Siwek-Wilczyńska *et. al* [64]:

$$\Gamma_i = \frac{g_i m_i \sigma_i U_i}{\pi^2 \hbar^2 a_i} \exp\left[2\left(a_i U_i\right)^{1/2} - 2\left(a_0 U_0\right)^{1/2}\right], \tag{3.20}$$

$$\Gamma_f = \frac{2\left[\left(a_f U_f\right)^{1/2} - 1\right]}{4\pi a_f} \exp\left[2\left(a_f U_f\right)^{1/2} - 2\left(a_0 U_0\right)^{1/2}\right] . \quad (3.21)$$

In Eq. (3.20), g_i is the spin degeneracy of emitted particle i, m_i is its mass, and σ_i is the cross section for the inverse reaction. The a_i and a_f terms in Eq. (3.20) and (3.21) are the level density parameters for particle emission and fission, respectively. These will be described later. Some of the initial excitation energy of the system, E^*_{CN}, is used by the rotational motion of the system and the pairing of nucleons and is thus "unavailable" to evaporate a particle or to fission. The "available thermal excitation energy" before deexcitation is described by:

$$U_0 = E^*_{CN} - E_{rot,0} - P_0 , \quad (3.22)$$

where $E_{rot,0}$ and P_0 are the rotational energy and pairing energy of the original nucleus. During the particle emission and fission processes, significant energy changes occur. The available thermal excitation energies for these processes were calculated as:

$$U_i = E^*_{CN} - E_{rot,i} - S_i - B_i - P_i , \quad (3.23)$$

$$U_f = E^*_{CN} - E_{rot,saddle} - B_f - P_{saddle} , \quad (3.24)$$

where U_i represents the available energy after particle emission has occurred, and U_f represents the available energy at the fission saddle point. The particle separation energies, S_i, in Eq. (3.23) were taken from the experimental data in Ref. [29]. All of the other terms in Eqs. (3.22)-(3.24) will be discussed below.

The rotational energies, E_{rot}, were calculated using the formula:

$$E_{rot} = \frac{J(J+1)\hbar^2}{2I} \ , \tag{3.25}$$

where J is the angular momentum of rotating nucleus and I is the moment of inertia [58]:

$$I = \frac{2}{5} m_0 A R^2 (1 + \beta_2 / 3) \ . \tag{3.26}$$

In Eq. (3.26) above, m_0 = 931.494 MeV/c^2, R = (1.2 fm)$A^{1/3}$, and β_2 is the quadrupole deformation parameter [40]. The initial value of J was calculated using CCFULL (J_0 = l_{CN}), and each step of the deexcitation process removed a specific amount of angular momentum from the system. Each neutron, proton, and α particle emitted from system was allowed to remove 2$\hbar$, 3$\hbar$, and 10$\hbar$, respectively [111].

The particle emission barrier, B_i, in Eq. (3.23) is the Coulomb barrier for charged particle emission from the hot, rotating system. For neutron emission, it is natural that B_i = 0 MeV. For proton and α particle emission, a barrier such as Eq. (3.4) could be used, but research has shown that the barriers for charged particles being emitted from a hot, rotating nucleus are smaller than those calculated by Eq. (3.4) [112, 113]. The emission barriers in the theoretical model for protons and α particles were calculated using the semi-empirical formulas of Parker *et al.* [114]:

$$B_p \ / \ MeV = 0.106Z - 0.9 \, , \tag{3.27}$$

$$B_\alpha \ / \ MeV = \frac{2.88(Z-2)}{1.47\left(A-4\right)^{1/3} + 4.642} \, , \tag{3.28}$$

where Z and A were the atomic number and the mass number, respectively, of the excited nucleus before a particle was emitted. These formulas above were determined by

measuring the energies of protons and α particles evaporated from hot CN with $16 \leq Z \leq 105$ and determining B_p and B_α for each of those reactions. The experimentally measured barriers were then plotted against the atomic number of the emitting nucleus, and Eqs. (3.27) and (3.28) represent the equations of best fit.

The fission barrier, B_f, in Eq. (3.24) was one of the most important parameters in the entire theoretical model. The occurrence of fission during the de-excitation cascade was quite probable for the reactions studied in this dissertation, especially at small values of E^*_{CN}. Small changes in B_f resulted in large changes in Γ_f, and, due to the prevalence of fission, large changes in Γ_{tot}. Thus, an accurate model of B_f was key to obtaining good results from the theoretical model as a whole. The B_f in this work consisted of liquid-drop component calculated by the FISROT code [66, 115] plus a constant shell correction from [40]:

$$B_f(l) = B_{f,LD}(l) + \Delta_{shell}. \tag{3.29}$$

The liquid-drop portion of the fission barrier depends on the angular momentum of the rotating nucleus; as the angular momentum increases, the rotating nucleus deforms and moves closer to the fission saddle point. The angular momentum dependence of the fission barrier was also calculated by the FISROT code. The absolute uncertainty in $B_f(l)$ was expected to be ± 0.5 MeV. This uncertainty leads to a one order of magnitude uncertainty in the theoretical calculation of σ_{EvR}.

The final ingredient in Eqs. (3.22)-(3.24) was the pairing energy, P. The pairing term is strongest when all of the valence protons and neutrons are paired (i.e. when there

are even numbers of protons and neutrons, an "even-even" nucleus). The pairing energy is weaker for even-odd or odd-even nuclei, and it is weakest for odd-odd nuclei, where there is both an unpaired proton and neutron. The pairing energy was calculated as [32]:

$$P = \begin{cases} 22MeV/\sqrt{A} & \text{, even-even} \\ 11MeV/\sqrt{A} & \text{, even-odd or odd-even .} \\ 0 & \text{, odd-odd} \end{cases} \tag{3.30}$$

The pairing energy at the saddle point was assumed to the same as the pairing energy in the ground state [64]. Once the pairing energy was calculated, the thermal excitation energies U_0, U_i and U_f were able to be calculated.

Alongside the thermal excitation energies, the most important components in calculating the decay widths in Eqs. (3.20) and (3.21) were the level density parameters for the parent nucleus, a_0, for particle emission, a_i, and for fission, a_f. The level density parameters were calculated in a two-step approach that reduced the level density near shell closures, and the shell effects were faded out with increasing E^*_{CN} [116]:

$$a_0 = \tilde{a}\left\{1+\frac{\Delta^A_{shell}}{U_0}\left[1-\exp\left(-U_0/E_D\right)\right]\right\} \tag{3.31}$$

$$a_i = \tilde{a}\left\{1+\frac{\Delta^{A-A_i}_{shell}}{U_i}\left[1-\exp\left(-U_i/E_D\right)\right]\right\} , \tag{3.32}$$

$$a_f = \tilde{a}\left\{1+\frac{\Delta^A_{shell,saddle}}{U_f}\left[1-\exp\left(-U_f/E_D\right)\right]\right\} . \tag{3.33}$$

In the above equations, the shell corrections, Δ_{shell}, were taken for the parent nucleus, the nucleus after particle emission, and the parent nucleus at the fission saddle point,

respectively. E_D = 18.5 MeV is the shell damping parameter which controls the fade-out of shell effects with increasing E^*_{CN} . The shell correction at the saddle point has been assumed to be zero [64], so $a_f \approx \tilde{a}$. The asymptotic level density parameter, $\tilde{a}$, was calculated using the formula of [55]:

$$\tilde{a} / MeV^{-1} = 0.04543(r_0 / fm)^3 A + 0.1355(r_0 / fm)^2 A^{2/3} B_S + 0.1426\left(r_0 / fm\right) A^{1/3} B_K \ . \quad (3.34)$$

In Eq. (3.34) above, r_0 = 1.15 fm, and B_s and B_K are the surface and curvature factors, respectively. B_s and B_K are parameters in the rotating liquid drop model, and tabulated values are presented in [117]. It is important to note that $B_s = B_K = 1$ for spherical nuclei. All the terms in Eqs. (3.20) and (3.21) have now been defined, and W_{sur} can now be calculated. However, there is one more important factor to consider when calculating W_{sur}.

3.3.1 Collective Enhancement to the Level Density

As discussed in Section 1.4.2 of this dissertation, CELD may have a large impact on the EvR cross sections measured in this work. In the theoretical model, CELD was included to directly modify the level density, which can then directly modify the decay width as such [59]:

$$\Gamma_i \rightarrow K_{coll,i}\Gamma_i \ , \quad (3.35)$$

$$\Gamma_f \rightarrow K_{coll,f}\Gamma_f \ , \quad (3.36)$$

$$K_{coll}(U,\beta_2) = K_{rot}\varphi(\beta_2) f(U) + K_{vib}[1-\varphi(\beta_2)] f(U). \quad (3.37)$$

The rotation and vibrational collective enhancement factors, denoted as K_{rot} and K_{vib}, respectively, were calculated with following equations:

$$K_{rot} = \frac{J_{\perp} T}{\hbar^2}, \quad (3.38)$$

$$K_{vib} = \exp[0.0555 A^{2/3} (T)^{4/3}], \quad (3.39)$$

where $J_{\perp} = l_{CN}$ is the component of the angular momentum that is perpendicular to the axis of rotation and T, the nuclear temperature, was calculated as:

$$T = \sqrt{U_0 / a_0}. \quad (3.40)$$

It should be noted that $K_{rot} \approx$ 100-150 is typically an order of magnitude larger than $K_{vib} \approx$ 1-10 due to the much smaller spacing of rotational levels. In Eq. (3.37), $\varphi(\beta_2)$ is a smoothing function that weights K_{coll} based on the shape of the nucleus:

$$\varphi(\beta_2) = \left[1 + \exp\left(\frac{\beta_2^0 - |\beta_2|}{\Delta\beta_2}\right)\right]^{-1}. \quad (3.41)$$

The value of β_2 was taken either for the ground state parent nucleus (when calculating $K_{coll,i}$) or for the saddle point of the fissioning parent nucleus (when calculating $K_{coll,f}$). The quantity $\beta_2^0 \approx 0.15$ represents the boundary between spherical and deformed nuclei, and $\Delta\beta_2 \approx 0.04$. The final parameter in Eq. (3.37) is the Fermi function, $f(U)$, which accounts for the fade-out of CELD with increasing excitation energy:

$$f(U) = \left[1 + \exp\left(\frac{U - E_{crit}}{d_{crit}}\right)\right]^{-1}. \quad (3.42)$$

The values of U were calculated from Eq. (3.23) or (3.24) when calculating $K_{coll,\,i}$ and $K_{coll,\,f}$, respectively. The other parameters in Eq. (3.42) were E_{crit} = 40 MeV and d_{crit} = 10 MeV.

4. EXPERIMENTAL RESULTS AND DISCUSSION*

The use of ^{45}Sc as a projectile in fusion-evaporation reactions has been very limited, and, to the best of our knowledge, no other literature data exists specifically on ^{45}Sc-induced hot fusion-evaporation reactions. The use of ^{44}Ca as a projectile has been almost as limited, while other isotopes of Ca have been more widely used. The ^{48}Ca isotope has been used for the synthesis of SHEs (see [10] and references therein), and the ^{40}Ca isotope has been used as a projectile for fusion (e.g. [118, 119] and references therein) and for fusion-evaporation studies [54]. There was a study of cold fusion reactions with ^{44}Ca + $^{206, 208}$Pb [120], but otherwise ^{44}Ca has not been used as a projectile for hot-fusion-evaporation reactions. The results of the ^{44}Ca-induced reactions will serve as an interesting comparison to the ^{45}Sc results because ^{44}Ca is only one proton removed from ^{45}Sc, but the CN are more "neutron-rich". Additionally, the measured data in this work will be compared to the ^{48}Ca, ^{50}Ti, and ^{54}Cr reactions which were previously studied within our research group. This section describes the experimental results of the ^{45}Sc- and ^{44}Ca-induced reactions and discusses the results of the model calculations in the context of these reactions.

* The data reported in this section are reprinted with permission from T. A. Werke *et al.*, Phys. Rev. C **92**, 034613 (2015) and T. A. Werke *et al.*, Phys. Rev. C **92**, 054617 (2015), © 2015 American Physical Society

4.1. Properties of the Irradiations

The reactions using ^{45}Sc as the projectile were performed over three temporally separated experiments starting in August 2012 and finishing in July 2014. The $^{45}Sc^{6+}$ projectiles were accelerated by the K500 cyclotron, and each experiment lasted 5-7 days with a total beam dose that ranged between $4.9 \times 10^{14} – 3.3 \times 10^{15}$ particles. The average beam intensities on the Faraday Cup FC02 (located just outside the extraction point of the K500 cyclotron) ranged between 11 and 19 enA, and the intensity reading on the TC FC was consistently about one-third of the FC02 value. The beam energy from the cyclotron was requested to be ≈ 5 MeV/A, and the beam energies were varied with the Al degrader system described in Section 2.1.2 The first two days of each experiment were typically used to develop the beam and perform the preliminary measurements and calibrations described in Section 2.2. The remainder of the beam time was devoted to measuring EvR excitation functions; the term "excitation function" simply means that the EvR cross sections were measured at multiple beam energies.

The experiment with ^{44}Ca projectiles was performed in one, seven-day irradiation in July of 2014, and the format was similar to the ^{45}Sc irradiations. The $^{44}Ca^{6+}$ projectiles were accelerated by the K500 cyclotron, and the total beam dose was 4.1×10^{14} particles. The average beam intensity on FC02 was 5 enA, and the intensity on the TC FC was again consistently about one-third of that. The ^{45}Sc and ^{44}Ca irradiations are summarized in Table 4.1.

Table 4.1. Selected properties of the beam irradiations described in this dissertation.

Experiment Date	Reactions Studied	Beam Energy (MeV)	Avg. Intensity on FC02 (enA)	Beam Dose (x 10^{14} particles)
July 11-16, 2012	^{45}Sc + ^{159}Tb, ^{162}Dy	224.6	19	32.5
August 16-21, 2013	^{45}Sc + ^{158,} ^{160}Gd, ^{159}Tb	227.6	11	4.9
July 1-7, 2014	^{45}Sc + ^{156,} ^{157}Gd, ^{159}Tb	226.0	13	17.2
July 15-21, 2014	^{44}Ca + ^{158}Gd, ^{159}Tb, ^{162}Dy	211.0	5	4.1

4.2 Results of the ^{45}Sc-Induced Reactions

The ^{45}Sc + $^{156\text{-}158,\ 160}$Gd, ^{159}Tb, and ^{162}Dy reactions were studied in this work. The beam energies were selected so that the production of the CN followed by emission of four neutrons – this is termed the "4*n* EvR" or, alternatively, the "4*n* exit channel" - was maximized and its excitation function could be fully measured. Along with the 4*n* EvR, the 3*n*, 5*n*, and 6*n* EvRs were also observed at various energies, although complete excitation functions were not measured. These are collectively termed the "*xn* EvRs" or "*xn* exit channels". The 4*n* EvR was observed for all of the reactions listed above, but the other *xn* channels were not observed for *all* of the reactions. In addition to the *xn* exit channels, channels that involved the emission of a proton plus a few neutrons from the CN were also observed; these were collectively termed the "*pxn* EvRs" or "*pxn* exit channels". A combination of the *p*2*n*, *p*3*n*, *p*4*n*, and *p*5*n* exit channels were observed for

all of the ^{45}Sc-induced reactions studied in this work. Finally, the emission of an α particle accompanied by 0, 1, or 2 neutrons from the CN was observed for the ^{45}Sc + ^{162}Dy reaction.

Example α-decay spectra for all six of the ^{45}Sc-induced reactions are presented in Fig. 4.1. Selected decay properties of the 4*n* and *p*3*n* EvRs are presented in Table 4.2. The measured α-particle energies were obtained for each nuclide by fitting the α-particle energy spectrum with the GF3 program; see Section 2.6 for more information about data

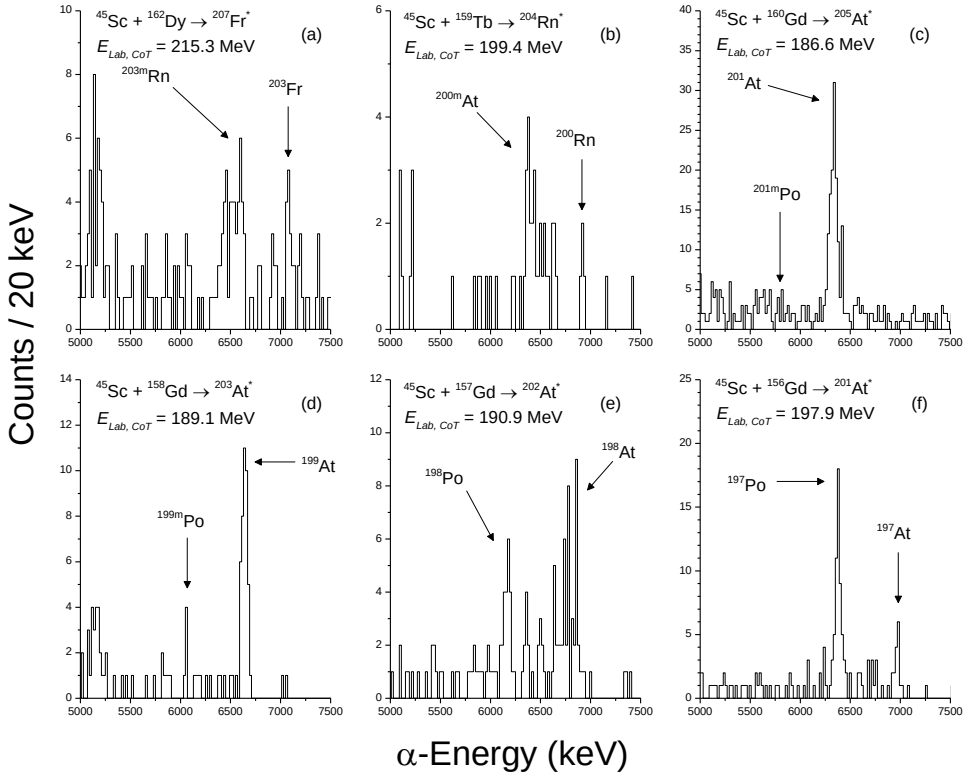

Figure 4.1. Experimental α-particle energy spectra for the six ^{45}Sc-induced reactions studied in this work. The selected beam energies correspond to the peak of the 4*n* EvR excitation function. The approximate positions of the 4*n* and *p*3*n* EvR peaks are labelled on the spectra. The *p*3*n* peak for the ^{45}Sc + ^{160}Gd reaction, shown in panel (c), did not pass the statistical test described in Section 2.6.2. Figure used with permission from [121].

fitting procedures. These spectra represent the peak of the 4*n* excitation functions for these reactions and also include the expected location of the *p3n* peak. A full listing of measured EvR cross sections from the ^{45}Sc-induced reactions is presented in Table 4.3. All the reported error bars in Table 4.3 are statistical only, and the systematic error is estimated to be 50%, primarily due to the uncertainty in the MARS efficiency. Many of the cross sections were near the experimental limits of sensitivity, and all of the reported data points in Table 4.3 have passed the statistical test described in Section 2.6.2. Approximately half of the possible EvR data points were rejected by the test.

Table 4.2. Properties of the 4*n* and *p*3*n* EvR for the ^{45}Sc-induced reactions studied in this work. The observed α-decay energies, $E_{\alpha,\,obs}$, were fit using GF3. The literature α-decay energies, branching ratios, and half-lives, denoted as $E_{\alpha,\,lit}$, $b_{\alpha,\,lit}$, and $t_{1/2,\,lit}$, respectively, were taken from [29].

Reaction	4*n*, *p*3*n* EvR	$E_{\alpha,\,obs}$ (keV)	$E_{\alpha\,,\,lit}$ (keV)	$b_{\alpha,\,lit}$ (%)	$t_{1/2,\,lit}$
^{45}Sc +^{156}Gd	^{197}At	6960 ± 12	6959.0 ± 3.0	100	0.388 ± 0.006 s
	^{197}Po	6326 ± 27	6281.0 ± 4.0	44 ± 7	53.6 ± 1.0 s
^{45}Sc +^{157}Gd	^{198}At	6724 ± 26	6753.0 ± 4.0	97	4.1 ± 0.3 s
	^{198}Po	6184 ± 49	6182.0 ± 2.2	57 ± 2	1.77 ± 0.03 min
^{45}Sc +^{158}Gd	^{199}At	6620 ± 31	6643.0 ± 3.0	90	7.03 ± 0.15 s
	^{199}Po	6030 ± 10	6059.0 ± 3.0	39 ± 4	4.17 ± 0.05 min
^{45}Sc +^{160}Gd	^{201}At	6314 ± 31	6342.0 ± 1.0	59	83 ± 2 s
	^{201}Po	5766 ± 33	5786.0 ± 2.0	2.9 ± 0.3	8.9 ± 0.2 min
^{45}Sc +^{159}Tb	^{200}Rn	6874 ± 16	6902.0 ± 3.0	98	0.96 ± 0.03 s
	^{200}At	6386 ± 52	6411.8 ± 1.3	57	43 ± 1 s
^{45}Sc +^{162}Dy	^{203}Fr	7072 ± 27	7131.0 ± 5.0	95	0.549 ± 0.015 s
	^{203}Rn	6580 ± 29	6550.3 ± 1.0	78	26.9 ± 0.5 s

Table 4.3. List of measured EvR cross sections in ^{45}Sc-induced reactions. $E_{lab,\,CoT}$ is the center-of-target projectile energy in the laboratory frame, and is the initial excitation energy of the CN. All of the reported cross sections passed the statistical test described in Section 2.6.2.

Target	$E_{Lab,CoT}$ (MeV)	E^*_{CN} (MeV)	σ_{3n} (μb)	σ_{4n} (μb)	σ_{5n} (μb)	σ_{6n} (μb)	σ_{p2n} (μb)	σ_{p3n} (μb)	σ_{p4n} (μb)	σ_{p5n} (μb)
^{156}Gd	182.6	38.9	5.8 ± 1.7	$1.2^{+0.9}_{-0.6}$			$3.6^{+1.9}_{-1.3}$	$1.4^{+1.1}_{-0.7}$		
	191.5	45.8	$3.1^{+1.9}_{-1.3}$	$3.4^{+1.8}_{-1.3}$				26 ± 5		
	197.9	50.8		5.7 ± 2.1				32 ± 5		
	203.3	54.9						24 ± 5	13 ± 3	
	208.7	59.1						11 ± 3	34 ± 5	
^{157}Gd	185.3	42.7	$9.8^{+4.6}_{-3.4}$							
	190.9	47.1	$6.7^{+3.1}_{-2.3}$	25 ± 5				18 ± 6	$5.9^{+3.2}_{-2.3}$	
	194.2	49.6	14 ± 4	22 ± 5			36^{+21}_{-15}	$8.0^{+3.9}_{-2.9}$		
	198.2	52.7	$2.9^{+2.4}_{-1.5}$	20 ± 5				39 ± 8	18 ± 5	
	200.5	54.5	$3.7^{+2.3}_{-1.6}$	14 ± 4	$3.5^{+2.1}_{-1.5}$		49^{+25}_{-18}	42 ± 8	28 ± 6	
	205.9	58.7		$3.3^{+2.9}_{-1.8}$				15 ± 6	29 ± 7	
	211.3	62.9						10^{+6}_{-4}	42 ± 9	$6.9^{+4.0}_{-2.8}$
^{158}Gd	180.4	40.8	15^{+13}_{-8}	$7.1^{+6.8}_{-4.3}$			69^{+59}_{-38}			
	185.9	45.1	$8.7^{+6.2}_{-4.2}$	34 ± 8						
	189.1	47.6	$8.3^{+5.2}_{-3.7}$	39 ± 7				26^{+24}_{-15}		
	195.3	52.4		33 ± 5	$3.0^{+1.9}_{-1.3}$			17^{+15}_{-9}	$3.5^{+2.6}_{-1.7}$	
	201.3	57.1		17 ± 4	11 ± 4			88 ± 33	23 ± 7	
^{160}Gd	181.2	45.4		100 ± 20						
	186.6	49.6	41 ± 14	150 ± 20	35 ± 10					
	189.9	52.2		120 ± 20	100 ± 20			150^{+120}_{-80}		
	194.3	55.6	12^{+6}_{-4}	140 ± 10	140 ± 10	$2.4^{+1.4}_{-1.0}$			38^{+15}_{-11}	
	202.0	61.1		28 ± 9	330 ± 30	41 ± 7				55^{+30}_{-22}

Table 4.3 Continued

Target	$E_{Lab,CoT}$ (MeV)	E^*_{CN} (MeV)	σ_{3n} (μb)	σ_{4n} (μb)	σ_{5n} (μb)	σ_{6n} (μb)	σ_{p2n} (μb)	σ_{p3n} (μb)	σ_{p4n} (μb)	σ_{p5n} (μb)
^{159}Tb	195.0	49.4					$4.8^{+4.1}_{-2.6}$			
	195.8	50.0						40 ± 14		
	199.4	52.8		$2.4^{+2.3}_{-1.4}$				39 ± 10	$3.1^{+2.5}_{-1.6}$	
	201.2	54.2						26 ± 10	$3.0^{+2.5}_{-1.6}$	
	203.9	56.3		$0.8^{+0.6}_{-0.4}$	$0.5^{+0.4}_{-0.3}$		9.8 ± 2.3	52 ± 5	9.5 ± 1.4	
	205.8	57.8					$7.4^{+3.3}_{-2.5}$	54 ± 8	17 ± 3	
	213.3	63.6		$2.0^{+1.3}_{-0.9}$			$8.1^{+3.4}_{-2.6}$	31 ± 6		
	217.0	66.5						19 ± 6	29 ± 4	
	221.4	69.9							11^{+6}_{-4}	15^{+7}_{-5}
^{162}Dy	201.5	51.3					$1.1^{+0.6}_{-0.4}$	8.1 ± 1.6	$1.1^{+0.6}_{-0.5}$	
	206.0	54.8					$1.2^{+0.9}_{-0.6}$	8.7 ± 2.4	$2.2^{+1.3}_{-0.9}$	
	207.7	56.2					$1.3^{+0.7}_{-0.5}$	10 ± 2	6.6 ± 1.5	
	215.3	62.1	$1.2^{+0.8}_{-0.5}$	1.8 ± 0.6	$0.7^{+0.4}_{-0.3}$		2.5 ± 0.8	7.2 ± 1.6	3.6 ± 1.0	
	218.9	64.9					$0.8^{+0.5}_{-0.3}$	$1.6^{+0.8}_{-0.6}$	12 ± 2	$0.7^{+0.4}_{-0.3}$
	223.3	68.3							6.6 ± 1.2	2.4 ± 0.6
			σ_{α} (μb)	$\sigma_{\alpha n}$ (μb)	$\sigma_{\alpha 2n}$ (μb)					
	201.5	51.3	98^{+40}_{-31}							
	206.0	54.8								
	207.7	56.2	200 ± 60	35^{+17}_{-12}						
^{162}Dy	215.3	62.1	40^{+30}_{-20}							
(cont.)	218.9	64.9		88 ± 20	$6.6^{+5.1}_{-3.3}$					
	223.3	68.3		79 ± 18	29 ± 8					

4.3 Results of the ^{44}Ca-Induced Reactions

The ^{44}Ca + ^{158}Gd, ^{159}Tb, and ^{162}Dy reactions were studied in this work. As for the ^{45}Sc-induced reactions, the beam energies were selected so that production of the 4*n* EvR was maximized and that a full 4*n* excitation function was measured for each reaction. The 3*n, 5n, and* 6*n* exit channels were observed for each of the ^{44}Ca-induced reactions, but full excitation functions were not measured. The *pxn* exit channels were observed in the ^{44}Ca + ^{159}Tb and ^{162}Dy reactions, but not for the ^{44}Ca + ^{158}Gd reaction. No α-particle exit channels were observed for any of the reactions. Selected EvR decay properties are presented in Table 4.4. As in the ^{45}Sc-induced reactions, the produced CN were northwest of the $N = 126$ closed shell, had significant shell corrections, and were nearly spherical.

Example α-decay energy spectra for the ^{44}Ca-induced reactions are presented in Fig. 4.2. These spectra represent the peak of the 4*n* excitation functions, and the expected location of the 4*n* EvR α-decay energy is marked on each panel. Additionally,

Table 4.4. Properties of the 4*n* and *p*3*n* EvRs for the ^{44}Ca-induced reactions studied in this work. Columns headings are the same as in Table 4.2.

Reaction	4*n*, *p*3*n* EvR	$E_{\alpha,\,\mathrm{obs}}$ (keV)	$E_{\alpha,\,\mathrm{lit}}$ (keV)	$b_{\alpha,\,\mathrm{lit}}$ (%)	$t_{1/2,\,\mathrm{lit}}$
^{44}Ca + ^{158}Gd	^{198}Po	6150 ± 16	6182 ± 2	57 ± 2	1.77 ± 0.03 min
	^{198}Bi	N/A	N/A	0	10.3 ± 0.3 min
^{44}Ca + ^{159}Tb	^{199}At	6630 ± 12	6643 ± 3	90[a]	6.92 ± 0.13 s
	^{199m}Po	6042 ± 20	6059 ± 3	9.4 ± 1	4.17 ± 0.05 min
^{44}Ca + ^{162}Dy	^{202}Rn	6642 ± 15	6639.5 ± 1.9	78 ± 8	9.7 ± 0.1 s
	^{202}At	6218 ± 26	6227.7 ± 1.4	37[a]	3.07 ± 0.02 min

[a]Uncertainties were not reported for these branching ratios

the expected locations of the *p*3*n* α-decay energy (for the ^{44}Ca + ^{159}Tb and ^{162}Dy reactions) or the 5*n* α-decay energy (for the ^{44}Ca + ^{158}Gd reaction) are marked. Due to the good EvR statistics, small backgrounds, and short α-decay half-lives for the EvRs produced in the ^{44}Ca + ^{159}Tb, ^{162}Dy reactions, it was possible to correlate the implant event of the EvR into the PSSD with the subsequent α-decay event. These "EvR-α_1" correlations give information on the lifetime of the decaying nucleus and help confirm the identity of the EvR. Plots of the EvR-α_1 correlations for the ^{44}Ca + ^{159}Tb and ^{162}Dy reactions are presented in panels a) and b) of Fig. 4.3. The possible EvR-α_1 correlations were constrained to events occurring in the same strip in the PSSD (~ 3mm horizontal width) and to ±1.5 mm in the vertical direction. Additionally, the maximum allowable time between the EvR implant event and the α-decay event was constrained to be five half-lives. The vertical position correlations are presented in panel c) of Fig. 4.3. The experimental lifetimes determined in panels a) and b) were extracted from the data by fitting the experimental data with Eq. (8) from [122].

Additionally, α_1-α_2 correlations were observed for the ^{44}Ca + ^{162}Dy reaction, and the results are presented in panel d) of Fig. 4.3. These were observable because the α-decay daughter of the 4*n* EvR, which was ^{198}Po, has a (57 ± 2)% α-decay branching ratio and a 1.77 min half-life. Based on the α-detection probability of the PSSD of (55 ± 3)% and the α-branching ratio of ^{202}Rn of (78 ± 8)%, it was expected that the 39 observed ^{202}Rn EvR-α_1 decays in panel c) of Fig. 4.3 would result in 17 ^{198}Po α_1-α_2 correlations in panel d) of Fig. 4.3. The observed 13 EvR-α_1-α_2 events in panel d) of Fig.

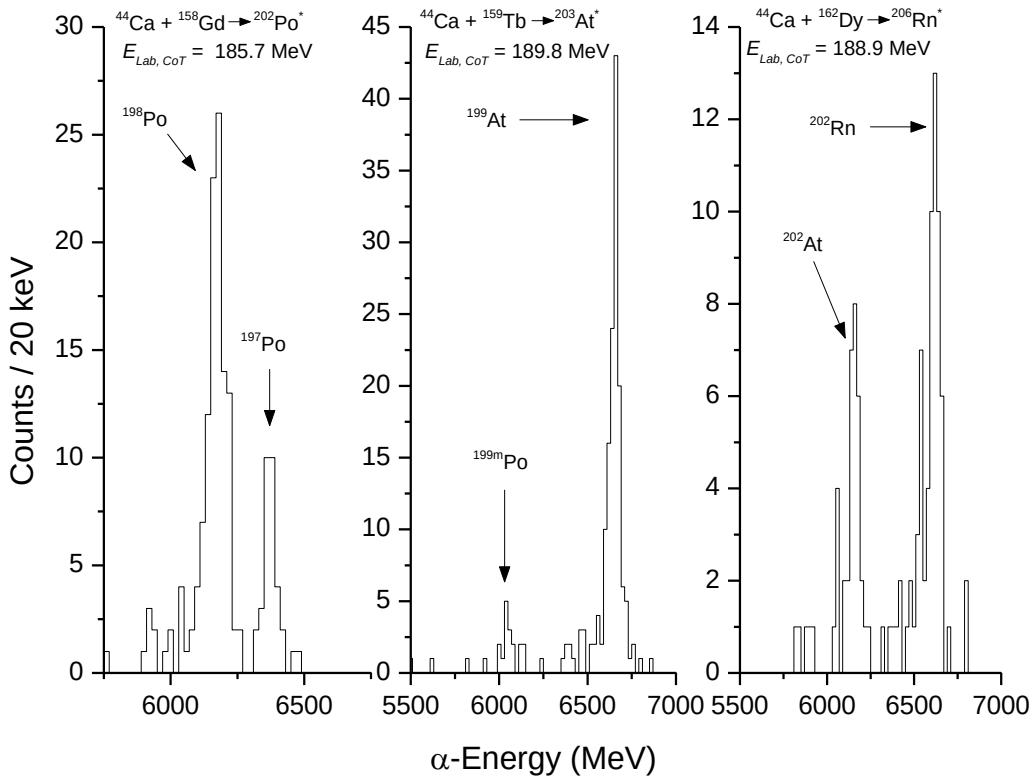

Figure 4.2. Experimental α-particle energy spectra for the three ^{44}Ca-induced reactions studied in this work. The selected beam energies correspond to the peak of the 4*n* EvR excitation function. The arrows show the approximate location of the 4*n* EvR peak (all three reactions) and either the *p*3*n* peak (for the ^{44}Ca + ^{159}Tb, ^{162}Dy reactions) or the *5n* EvR peak (for the ^{44}Ca + ^{158}Gd reaction). Figure used with permission from [123].

4.3 is reasonable. The energy limits for the accepted α_1-α_2 correlations in panel d) were determined by the experimental resolution of the PSSD (≈60-80 keV FWHM) and are roughly represented by the black circle. The two data points just below the circle fell outside the acceptable energy range for the 6182 keV α particle emitted from ^{198}Po.

The full listing of measured EvR cross sections measured in the ^{44}Ca-induced reactions is presented in Table 4.5. The ^{44}Ca reaction data were subjected to the same statistical test as the ^{45}Sc reaction data. A large portion of the data passed the statistical

test described in Section 2.6.2 because MARS was tuned to one charge state above the peak for all the ^{44}Ca-induced reactions. The backgrounds were very small for all these reactions. The error bars reported in Table 4.5 are again purely statistical, and the absolutely uncertainties are estimated to be ~50% due primarily to the uncertainty in the MARS transmission efficiency.

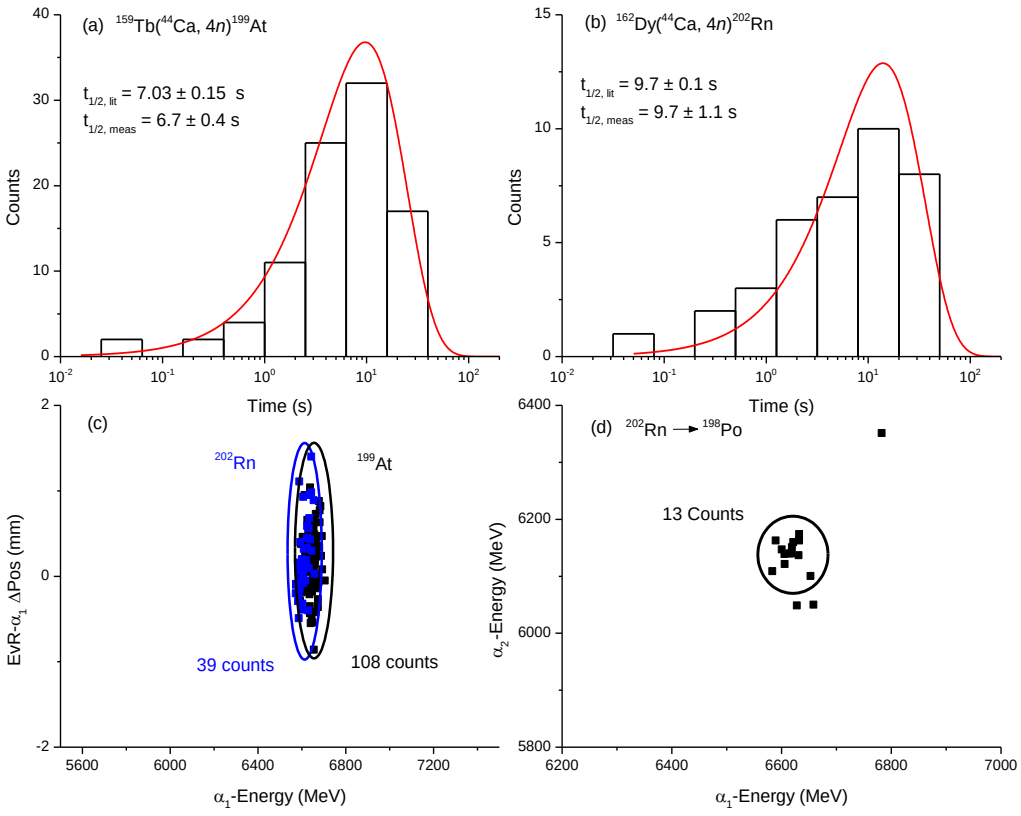

Figure 4.3. EvR Implant-α correlations for the 4n products of the ^{44}Ca + ^{159}Tb, ^{162}Dy reactions. Panels a) and b) show the measured lifetime distributions for ^{199}At and ^{202}Rn, respectively. The measured half-lives were extracted using Eq. (8) in [122]. The literature values were taken from [29]. The EvR-α_1 position correlations for both EvRs are shown in panel (c). The α_1-α_2 correlations are shown in panel (d). There were thirteen counts inside the circle drawn on the plot. The other counts in panel (d) fell outside the acceptable energy range based on the resolution of the PSSD. Figure used with permission from [123].

Table 4.5. List of measured EvR cross sections in the reactions with ^{44}Ca projectiles. Column headings are the same as in Table 4.3.

Target	$E_{Lab,CoT}$ (MeV)	E^*_{CN} (MeV)	σ_{3n} (μb)	σ_{4n} (μb)	σ_{5n} (μb)	σ_{6n} (μb)	σ_{p2n} (μb)	σ_{p3n} (μb)	σ_{p4n} (μb)	σ_{p5n} (μb)
	177.6	44.7	2290^{+590}_{-490}	600^{+120}_{-100}						
	184.2	49.8	910^{+340}_{-270}	1620 ± 150	200^{+60}_{-50}					
^{158}Gd	185.7	51.0	1840^{+620}_{-480}	2100 ± 230	600^{+130}_{-110}					
	188.4	53.1	1440^{+440}_{-340}	1940 ± 190	620 ± 100					
	191.3	55.4	1020^{+360}_{-290}	1380 ± 140	1090 ± 120					
	196.0	59.1	770^{+320}_{-250}	660 ± 110	2700 ± 180	56^{+29}_{-21}				
	184.7	45.8	140^{+37}_{-30}	130 ± 20						
	189.8	49.9	90^{+25}_{-21}	230 ± 20	18^{+8}_{-6}			170^{+70}_{-60}		
^{159}Tb	196.3	54.9	23^{+11}_{-8}	120 ± 10	34^{+8}_{-7}			220^{+60}_{-50}	33^{+10}_{-8}	
	200.5	58.2		41^{+10}_{-8}	48^{+11}_{-9}			200^{+80}_{-60}	51^{+15}_{-12}	
	208.0	64.1			33^{+9}_{-7}			160^{+70}_{-50}	50^{+14}_{-11}	38^{+11}_{-9}
	183.7	43.9	71^{+17}_{-14}	50^{+13}_{-11}						
	188.9	48.0	59^{+19}_{-15}	130 ± 20				62^{+31}_{-23}		
^{162}Dy	195.4	53.1	31^{+11}_{-9}	76 ± 14	24^{+7}_{-6}		62^{+44}_{-30}	98^{+28}_{-22}	25^{+11}_{-8}	
	199.5	56.4		55^{+12}_{-10}	20^{+7}_{-5}			100^{+30}_{-20}	100 ± 20	51^{+16}_{-13}
	207.1	62.3		14^{+7}_{-5}	27^{+7}_{-6}			29^{+17}_{-12}	94 ± 18	42^{+15}_{-12}

4.4 Discussion

Most of the EvRs had large α-decay branching ratios and short half-lives. The α-particle decay energies for all of the EvRs measured in the ^{45}Sc-induced reactions ranged from 5786-7241 keV, and the half-lives were between 0.3 s and 3.1 min. For the ^{44}Ca-induced reactions, the α-particle decay energies ranged between 6059-6856 keV, and the half-lives were between and 1.04 s and 4.17 min.

The CN produced by these reactions were all located to the northwest of ^{208}Pb. spherical closed shell. All of the CN were close enough to the shell such that they had significant shell corrections. The shell corrections lead to enhancement of the liquid-drop portion of the fission barrier (see Eq. (3.29)). The larger fission barrier should have led to enhancement of the EvR cross sections. However, the CN produced in the reactions were nearly spherical, meaning that the values of the quadrupole deformation parameter, β_2, were < 0.15. The quadrupole deformations at the fission saddle point were > 1, meaning that the CN underwent large shape changes as fission occurred. This meant that level density for fission would be greatly enhanced as the CN deformed and the system gained rotational levels. The large shape change and the proximity to the closed neutron shell means that these reactions were good candidates for studying the influence of CELD. If the expected cross-sectional enhancement was not observed, then CELD could be used to explain the lack of enhancement. Selected properties of the CN and the decay cascade are presented in Table 4.6. The negative value of the shell correction is meant to indicate a stabilizing influence on the nucleus. When B_f was calculated using

Table 4.6. Selected properties of the CN and the decay cascade for the ^{45}Sc-induced reactions and ^{44}Ca-induced reactions. The liquid-drop shell correction, $\Delta_{shell,\,CN}$, was taken from [40]. The quantity $\overline{B_f - S_n}$ represents the average difference is the fission barrier and neutron across the entire deexcitation cascade, and B_f was calculated for each step using Eq. (3.29). The proton and neutron separation energies, S_p and S_n, respectively, were taken from [29], and the quadrupole deformation parameter, β_2, was taken from [40].

Reaction	CN	N_{CN}	$\Delta_{shell,\,CN}$ (MeV)	$\overline{B_f - S_n}$ (MeV)	S_p(CN) (MeV)	S_n(CN) (MeV)	β_2(CN)
^{45}Sc + ^{156}Gd	^{201}At	116	-2.14	–0.2	1.124(17)	9.87(3)	+0.071
^{45}Sc + ^{157}Gd	^{202}At	117	-2.87	+0.8	1.350(30)	7.87(3)	+0.062
^{45}Sc + ^{158}Gd	^{203}At	118	-3.59	+1.8	1.527(18)	9.64(3)	+0.045
^{45}Sc + ^{160}Gd	^{205}At	120	-5.07	+4.0	1.918(19)	9.17(3)	+0.035
^{45}Sc + ^{159}Tb	^{204}Rn	118	-2.90	–0.2	3.109(18)	9.90(3)	–0.087
^{45}Sc + ^{162}Dy	^{207}Fr	120	-3.66	0.0	1.018(23)	9.67(3)	–0.104
^{44}Ca + ^{158}Gd	^{202}Po	118	-4.64	+4.1	3.798(21)	9.471(16)	+0.009
^{44}Ca + ^{159}Tb	^{203}At	118	-3.59	+1.8	1.527(18)	9.64(3)	+0.045
^{44}Ca + ^{162}Dy	^{206}Rn	120	-4.26	+1.9	3.434(21)	9.47(5)	-0.044

Eq. (3.29), the absolute value of Δ_{shell} was added to the liquid drop calculation. The properties listed in Table 4.6 will be key in the discussion of the interpretation of the experimental results.

4.4.1 Observed Trends in the Experimental Data

The EvR data presented in Tables 4.3 and 4.5 have several noteworthy trends. The first observation is that the most neutron-rich reactions systems have the largest *xn* cross sections. These systems typically exhibit larger *xn* cross sections than *pxn* cross sections. As the reaction systems become more neutron-deficient, the *xn* sections decreased while the *pxn* cross sections remained relatively constant. A clear example is

the ^{45}Sc + $^{156\text{-}158,\ 160}$Gd series of reactions. The most neutron-rich target, ^{160}Gd, has a maximum 4*n* cross section of 150 ± 20 μb, while the ^{158}Gd, ^{157}Gd, and ^{156}Gd targets have maximum 4*n* cross sections of 39 ± 7 μb, 25 ± 5 μb, and 5.7 ± 2.1 μb respectively. For the most neutron-deficient reaction systems studied in this work, the *pxn* cross sections are larger than the *xn* cross sections. For example, the maximum *p*3*n* cross section of the ^{45}Sc + ^{159}Tb reaction is 54 ± 8 μb, which is approximately 20 times larger than the maximum 4*n* cross section of $2.4^{+2.3}_{-1.4}$ μb. Together, the *4n* EvR cross sections for the ^{45}Sc- and ^{44}Ca-induced reactions spanned more than three orders of magnitude, ranging from 2100 ± 230 μb in the ^{44}Ca + ^{158}Gd reaction to 1.8 ± 0.6 μb in the ^{45}Sc + ^{162}Dy reaction. The *p3n* data spanned a smaller range, ranging from 220 ± 80 μb in the ^{44}Ca + ^{159}Tb reaction to 10 ± 2 μb in the ^{45}Sc + ^{162}Dy reaction.

The ^{45}Sc and ^{44}Ca projectiles bombarded two of the same targets as the ^{48}Ca projectiles that were also studied by our group: ^{159}Tb and ^{162}Dy [50]. The experimental 4*n* EvR cross sections in the ^{48}Ca-, ^{44}Ca-, and ^{45}Sc-induced reactions are plotted in Fig. 4.4. The ^{45}Sc *xn* cross sections were *four* orders of magnitude smaller than the ^{48}Ca cross sections and two orders of magnitude smaller than the ^{44}Ca *xn* cross sections in reactions on the same targets. The maximum *4n* cross sections in the ^{44}Ca-induced reactions were factors of 54 ± 11, 96^{+92}_{-57}, and 72 ± 26 larger than in the ^{45}Sc reactions on the ^{158}Gd, ^{159}Tb, and ^{162}Dy targets, respectively. However, the maximum *4n* cross sections in the ^{44}Ca + ^{159}Tb and ^{162}Dy reactions were factors of 55 ± 9 and 97 ± 20, respectively, smaller than the ^{48}Ca-induced reactions on the same targets. It was expected that the

^{45}Sc-induced reactions would have smaller cross sections than the ^{48}Ca-induced reactions on the same targets simply due to the extreme neutron-richness of ^{48}Ca as compared to ^{45}Sc; however, the four orders-of-magnitude difference was quite surprising. The maximum *p3n* cross sections were 5-10 times larger in the ^{44}Ca-induced reactions than the ^{45}Sc-induced reactions. No *pxn* exit channels were observed in the ^{48}Ca-induced reactions, so no comparison can be made. Additionally, ^{50}Ti-induced reactions on these same targets were studied [51]. A listing of the reactions on ^{159}Tb and ^{162}Dy targets is presented in Table 4.7. The parameter *(N-Z)/A* represents the relative neutron asymmetry of the CN, and $\Sigma\sigma_{EvR}(E^*)$ is the sum of all of the EvR cross sections (includes *xn, pxn* and *αxn* exit channels when applicable) at a given excitation energy E^*. In this table, the sum of the EvR cross sections was taken at the energy which maximized production of the *4n* EvR. Clearly, there is a correlation between a more neutron-rich CN and larger EvR cross sections. This will be discussed in Section 4.4.3 below.

Table 4.7. Comparison of cross section data in ^{48}Ca-, ^{44}Ca-, ^{45}Sc-, and ^{50}Ti-induced reactions on ^{159}Tb and ^{162}Dy targets. The neutron asymmetry parameter *(N-Z)/A* represents the relative neutron-richness of the CN; a larger value of *(N-Z)/A* represents a more neutron-rich CN. The maximum 4*n* and *p*3*n* cross sections for the ^{48}Ca reactions were taken from [50], the ^{44}Ca and ^{45}Sc data were presented in this work, and the ^{50}Ti data were taken from [51]. The sum EvR cross sections were calculated by summing all of the reported EvR cross sections at the same energy as the maximum 4*n* EvR cross section.

Reaction	CN	*(N-Z)/A*	Max σ_{4n} (μb)	Max σ_{p3n} (μb)	$\Sigma\sigma_{EvR}(E^*)$ (μb)
^{48}Ca + ^{159}Tb	^{207}At	0.179	12600 ± 1900	N/A	16400
^{50}Ti + ^{159}Tb	^{209}Fr[a]	0.167	481^{+173}_{-144}	150^{+140}_{-90}	710
^{44}Ca + ^{159}Tb	^{203}At	0.163	230 ± 20	220^{+60}_{-50}	510
^{45}Sc + ^{159}Tb	^{204}Rn	0.157	$2.4^{+2.3}_{-1.4}$	54 ± 8	44
^{48}Ca + ^{162}Dy	^{210}Rn[b]	0.181	12600 ± 1700	N/A	13900
^{50}Ti + ^{162}Dy	^{212}Ra[a,b]	0.170	169^{+77}_{-60}	160^{+150}_{-98}	410
^{44}Ca + ^{162}Dy	^{206}Rn	0.165	130 ± 20	100^{+30}_{-20}	254
^{45}Sc + ^{162}Dy	^{207}Fr	0.159	1.8 ± 0.6	10 ± 2	57

[a]A sum of the *p*2*n* and *p*3*n* EvR cross sections was reported.
[b]A sum of the 4*n* and 5*n* EvR cross sections was reported.

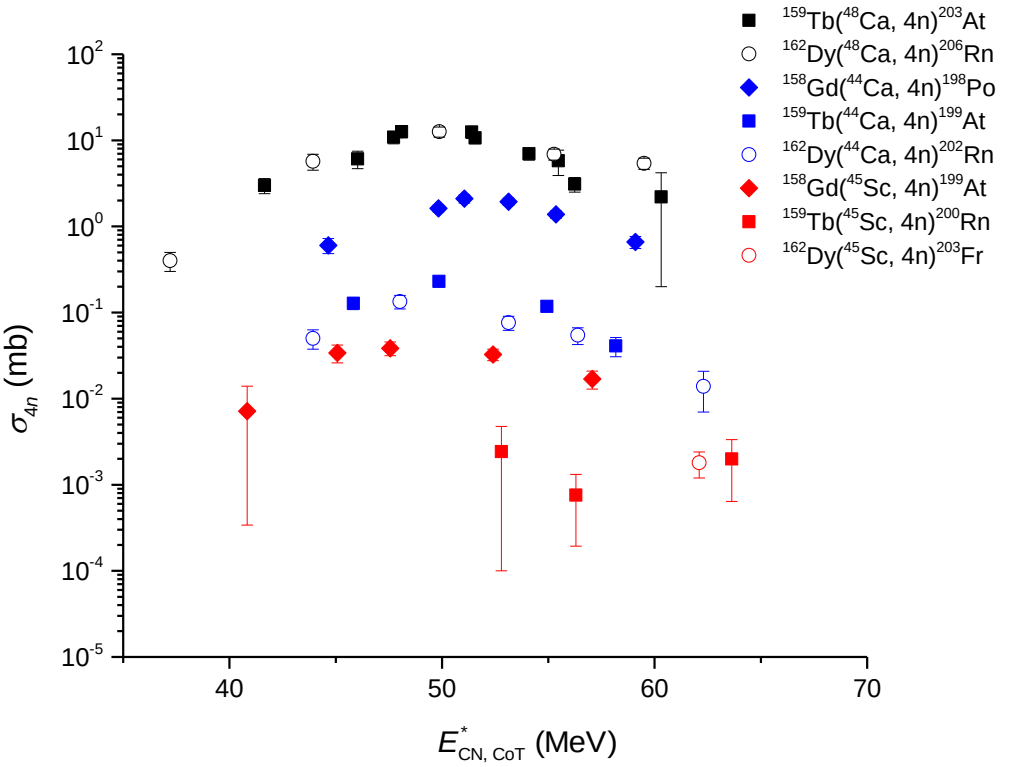

Figure 4.4. Excitation functions for reactions with ^{48}Ca projectiles (black data points), ^{44}Ca projectiles (blue data points), and ^{45}Sc projectiles (red data points). The solid squares indicate reactions on the ^{159}Tb target, open circles indicate reactions on the ^{162}Dy target, and solid diamonds indicate reactions on the ^{158}Gd target. The ^{48}Ca data were taken from [50], and the ^{44}Ca and ^{45}Sc data are presented in this work. Figure used with permission from [121].

4.4.2 Fit of the Model to the Data

The theoretical model which was described in Section III of this dissertation was used to fit the experimental data. The results of fitting the 4*n* and *p*3*n* exit channels with the model calculations for the ^{45}Sc- and ^{44}Ca-induced reactions are presented in Fig 4.5 and 4.6, respectively. The model does well to reproduce the 4*n* cross sections, but the

*p*3*n* cross sections are severely under-predicted. As discussed in Section III, the calculations for the capture cross section, σ_{capt}, are accurate within a factor of 2, so σ_{capt} is unlikely to be the source of the disagreement between the *p*3*n* data and theory. The compound nucleus formation probability, P_{CN}, is uncertain to a factor of ≈ 10, which could explain up to half of the disagreement between the model and data. However, P_{CN} is unlikely to be the difference between the *p*3*n* data and the model calculations following the discussion of the cross bombardments later in this Section.

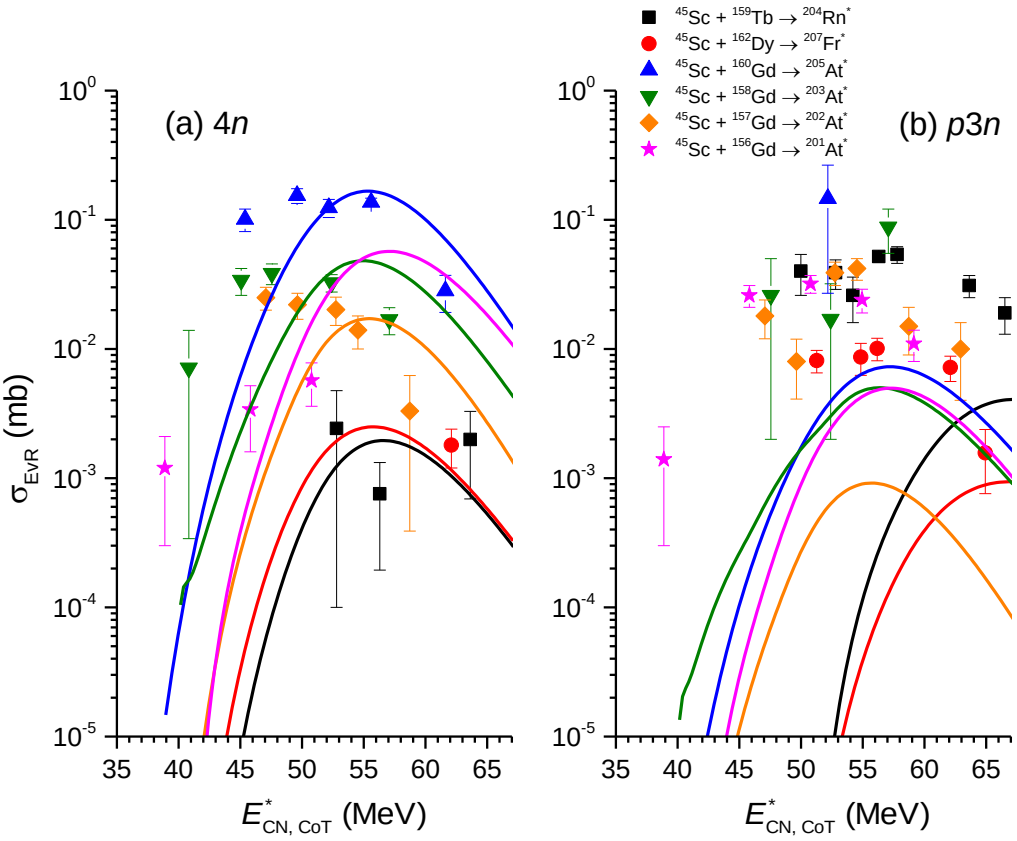

Figure 4.5. The a) 4*n* and b) *p*3*n* measured excitation functions (solid points) and theoretical calculations (solid lines) for the ^{45}Sc-induced reactions studied in this work. The agreement of the model with the data is good for the 4*n* exit channels, but the *p*3*n* exit channels are underpredicted. Figure used with permission from [121].

Additionally, errors in σ_{capt} and P_{CN} would affect the model calculations for the 4*n* and *p*3*n* exit channels equally.

The final factor is the survival probability, W_{sur}, which was calculated using Eq. (3.17) and Eq. (3.19) for *xn* and *pxn* exit channels, respectively. The three most influential factors in calculating W_{sur} for proton emission are the level density parameter for particle emission, a_i (see Eq. (3.32)), the particle emission barrier, B_i (see Eq. (3.27)), and the fission barrier, B_f (see Eq. (3.29)). The level density parameter used in this work was calculated with well-defined systematics, and the same formalism was used for

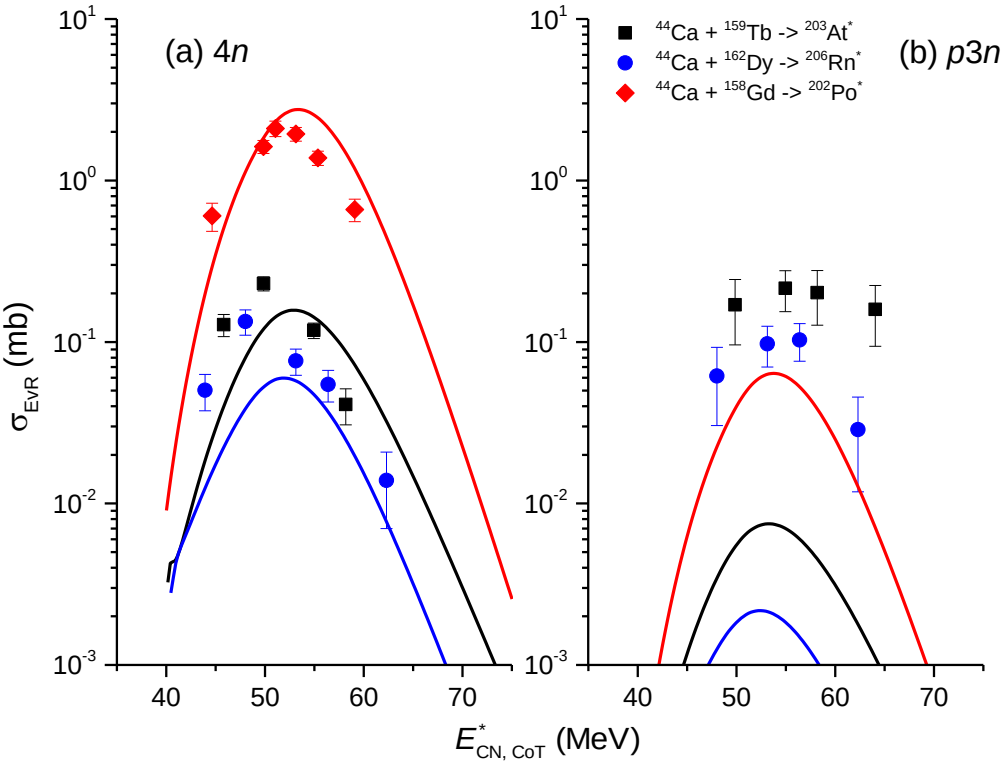

Figure 4.6. The a) 4*n* and b) *p*3*n* measured excitation functions (solid points) and theoretical calculations (solid lines) for the ^{44}Ca-induced reactions studied in this work.

neutron emission and proton emission. Because the 4*n* excitation functions are well-reproduced by the theoretical model, it is unlikely that the level density parameter caused the disagreement in the *p*3*n* excitation function. It has already been stated that the model used for B_f has an estimated error of approximately ±0.5 MeV, and the uncertainty for the neutron-deficient CN studied in this work may be even larger. However, such an error would affect the 4*n* and *p*3*n* excitation functions in a similar way, and would not be enough to account for poor fitting of the *p*3*n* excitation function without causing a discrepancy in the fit of the 4*n* excitation function. That leaves the proton emission barrier, B_p, which in this work was calculated with Eq. (3.27). It is possible that the B_p is still too large, even though Eq. (3.27) accounts for the emission of the proton from the hot, rotating CN. A small change in B_p results in a large change in the *p*3*n* survival probability; a 1 MeV change in the emission barrier results in a whole order of magnitude in the cross section. This is such a large effect because B_p exponentially affects the proton decay width, Γ_p, as shown in Eq. 3.20. The semi-empirical fits for B_p and B_α from [114] are plotted in Fig. 4.7. The fit for B_p on the top part of Fig. 4.7 is fairly good. However, there is a section between $Z \approx 40$ and $Z \approx 55$ where the difference between the experimental data and the fit is approximately 1 MeV. Thus, it is possible that for the neutron-deficient reaction systems studied in this work (with Z = 84-87) that the error is also 1 MeV. Additionally, nuclear structure effects could further facilitate the emission of a proton in these neutron-deficient systems. It is most likely that the model for B_p is the cause of the majority of the disagreement between the *p*3*n* data and the theoretical model, but more investigation is necessary to

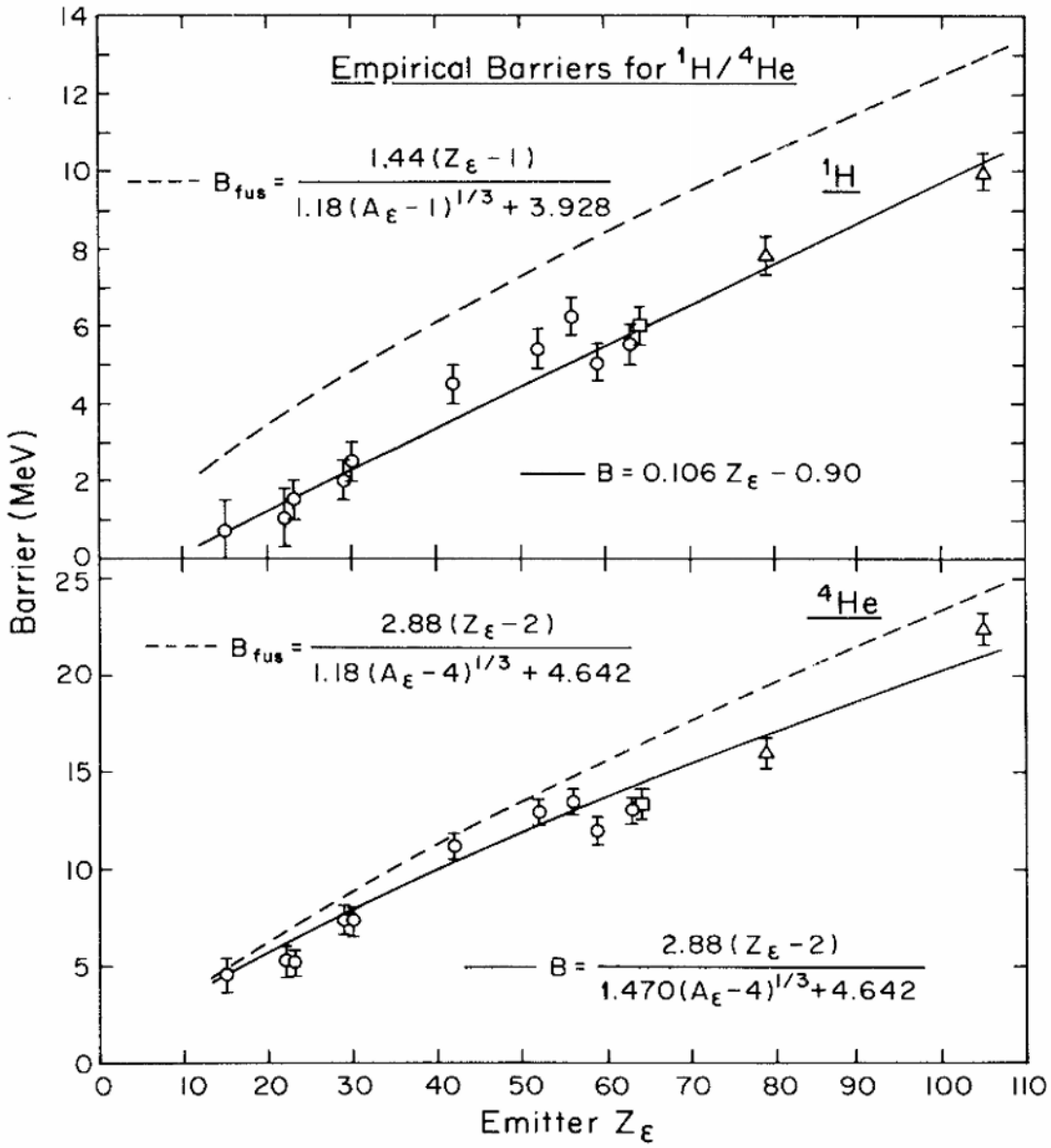

Figure 4.7. Empirical determinations of the proton (top) and α particle (bottom) emission barriers from hot, rotating nuclei over a wide range of *Z*. The open points represent measured emission barriers. The dashed lines represent the *fusion* barriers from [124], and the solid lines represent the empirical line of best fit in both cases. Figure used with permission from [114].

make a more quantitative statement. Ideally, the proton emission barriers for these neutron-deficient nuclei need to be measured.

To further examine the validity of the model in this region, experimental data were compared to theoretical calculations of 4*n* excitation functions over a wide range of cross sections. The results from the ^{40}Ar-, ^{40}Ca-, ^{48}Ca- and ^{45}Sc-induced reactions are presented in in Fig. 4.8. The beam energies were chosen specifically to maximize production of the 4*n* EvR (as is common in hot-fusion reactions), and the theoretical model does well to reproduce these cross sections. The reactions in Fig. 4.8 were chosen so that a wide range of reaction systems were examined. Fig. 4.8 includes systems that are relatively neutron rich (^{48}Ca + ^{159}Tb and ^{40}Ar + ^{165}Ho) and relatively neutron poor (^{45}Sc + ^{159}Tb and ^{40}Ca + ^{159}Tb), and the model does well to reproduce the *4n* excitation functions in both cases as well as intermediate cases (^{45}Sc + ^{160}Gd).

The dashed lines in Fig. 4.8 show the calculated "fusion" cross sections for each of the five reactions, where $\sigma_{fus} = \sigma_{capt}P_{CN}$. In the experimental data presented in this dissertation, two pairs of "cross-bombardment" reactions were studied, which means that the two reaction systems within the pair produced the same CN. According to the Bohr independence hypothesis [41], the decay of an excited CN is independent of its formation, an assumption which has been mostly supported by experimental data [125, 126]. The Bohr independence hypothesis leads to the conclusion that W_{sur} should be the same for the cross bombardments given that the CN has the same E^*_{CN} and l_{CN}. Thus, the difference in σ_{EvR} for the cross bombardment pairs comes from the difference in σ_{fus}, and the cross bombardment pair tests how well our model calculates σ_{fus}.

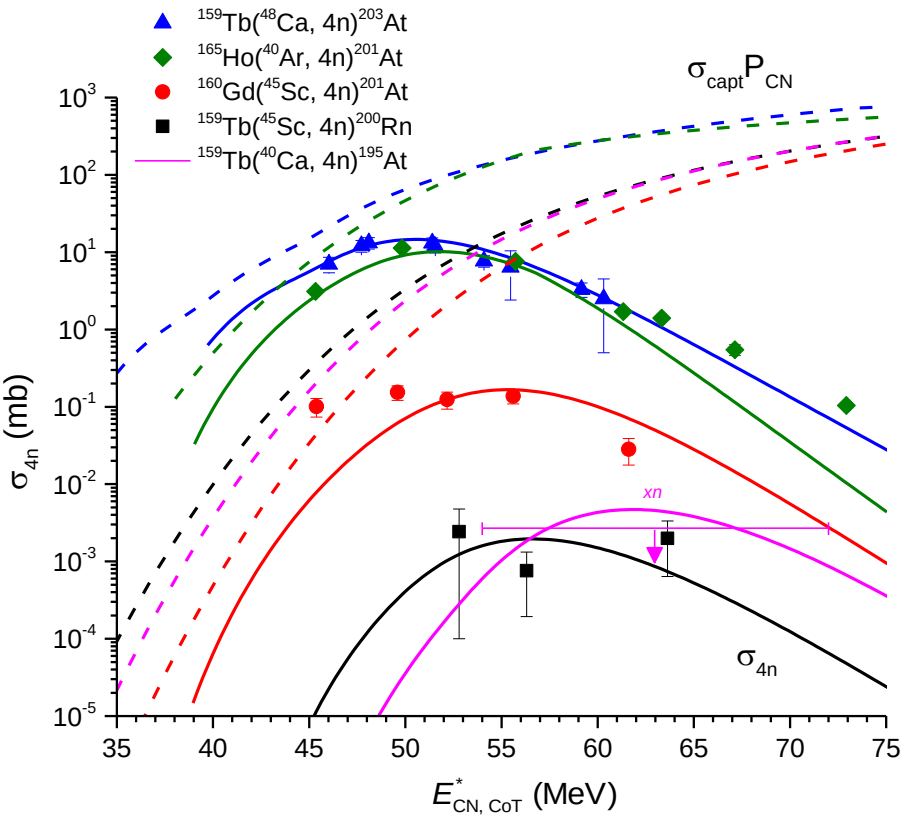

Figure 4.8. Tests of the described theoretical model using the 4*n* EvR cross sections produced with ^{40}Ar, ^{40}Ca, ^{48}Ca, and ^{45}Sc projectiles. The horizontal pink line represents that only an upper limit was reported for the *xn* cross sections in the ^{40}Ca + ^{159}Tb reaction. The dashed lines are the calculated fusion cross sections, and the solid lines are calculated *4n* EvR cross sections. The ^{40}Ar data were taken from [48], the ^{40}Ca were taken from [54], the ^{48}Ca data were taken from [50] and the ^{45}Sc data were taken from [121] and are presented in this dissertation. Figure used with permission from [121].

The 4*n* EvR cross sections for the two cross bombardment pairs are presented in Fig. 4.9, and the solid lines are the calculations of σ_{fus}. For both cross bombardments, the model calculations show that σ_{fus} is the main cause of the discrepancies in the measured *4n* EvR cross sections. This is especially evident for the ^{44}Ca + ^{159}Tb and ^{45}Sc + ^{158}Gd pair, where the *4n* cross sections are almost a full order of magnitude different at the

peak of the excitation function. The experimental difference in the measured *4n* cross sections at $E^*_{CN} \approx 50$ MeV is $\sigma_{4n}(^{44}\text{Ca})/\sigma_{4n}(^{45}\text{Sc}) \approx 6.5 \pm 1.2$, and the calculated difference due to the fusion cross section is $\sigma_{fus}(^{44}\text{Ca})/\sigma_{fus}(^{45}\text{Sc}) \approx 6$. The ^{45}Sc data were taken from [121] and this dissertation, while the ^{44}Ca data were taken from [123] and this dissertation. There was no measured experimental cross section near $E^*_{CN} \approx 50$ MeV for the ^{45}Sc + ^{158}Gd reaction, so this cross section was estimated with a linear interpolation between the measured cross sections at $E^*_{CN} \approx 47.6$ MeV and $E^*_{CN} \approx 52.2$ MeV. The error was estimated based on the errors of these two surrounding data points. As stated in Section 3.2, there is a factor of 10 uncertainty associated with P_{CN}; however, our approach to calculating P_{CN} leads to good agreement with the data for the reactions studied in this dissertation.

4.4.3 Discussion of the Data with the Model

The theoretical model was used to investigate the important physical factors which were responsible for determining the EvR cross sections. One important experimental question that needed to be answered was this: what caused the four order-of-magnitude difference between the ^{48}Ca- and ^{45}Sc-induced reactions on the same target? Additionally, the importance of CELD is still an open question (see Section 1.4 for discussion), and the ^{45}Sc and ^{44}Ca reactions studied in this work were good candidates to study this effect. Finally, the model was able provide some insight into

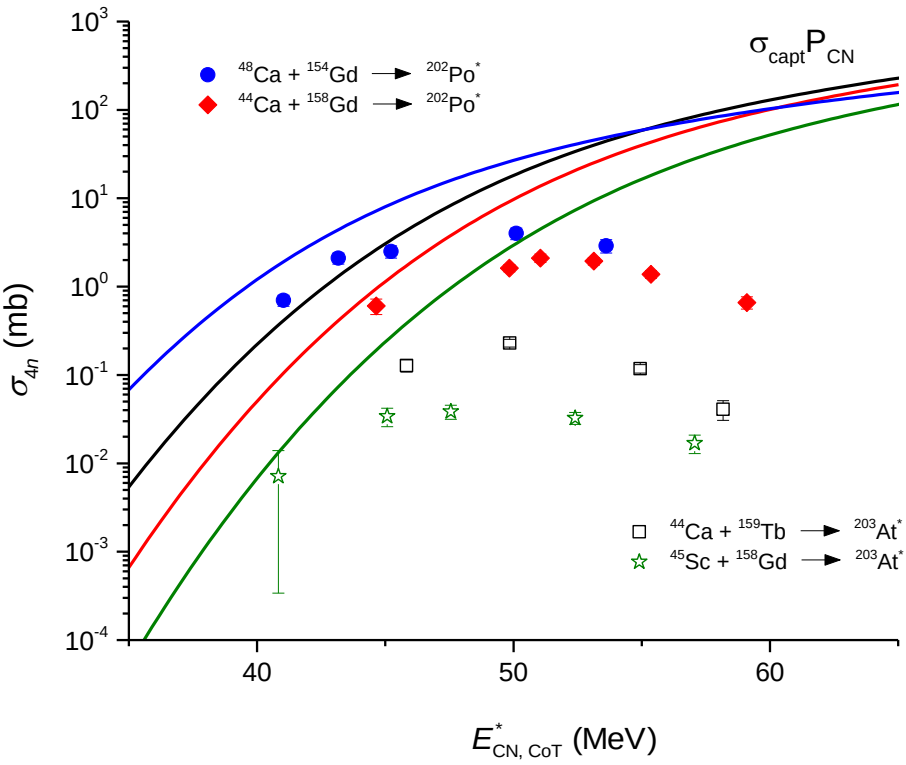

Figure 4.9. Cross sections for the 4*n* EvR for the two cross bombardment pairs studied in this dissertation. Solid lines are calculations of σ_{fus}, and points are the experimental data. Each line is associated with the data points of the same color. The ^{48}Ca data was taken from [50], while the ^{44}Ca and ^{45}Sc data are presented in this dissertation. Figure used with permission from [123].

how well ^{45}Sc and ^{44}Ca would perform in reactions which synthesize superheavy elements.

As shown in Table 4.7, there was a correlation between the relative neutron-richness of the reaction system and the magnitude of the EvR cross sections. Table 4.8 reports the maximum measured *4n* cross sections in the ^{48}Ca, ^{44}Ca-, and ^{45}Sc + ^{159}Tb reactions. The calculated values of σ_{capt}, P_{CN}, and $W_{sur,\,4n}$ at the given initial excitation

energy of the CN, E^*_{CN}, are also reported, and W_{sur} is shown to be the primary factor in determining the EvR cross sections. Note that multiplying σ_{capt}, P_{CN}, and $W_{sur,\,4n}$ in Table 4.8 will not exactly equal the listed values of $\sigma_{4n,\,max}$ because the former quantities were all calculated while the latter quantity was measured experimentally.

Qualitatively, the neutron richness affects W_{sur} as such: for a neutron-rich reaction system, the neutron binding energy will be relatively small and the fission barrier will be relatively large. Thus, neutron emission from the excited CN will be preferred over fission or charged particle emission. The opposite is true for a neutron-deficient reaction; the neutron binding energy will be relatively large and the fission barrier will be relatively small. Thus, fission will the preferred mode of deexcition, and particle emission can effectively compete with neutron emission.

Quantitatively, it was shown in Eqs. (3.20) and (3.21) that the calculated neutron decay width and the fission width depend on the exponential of S_n and B_f, respectively,

Table 4.8. Maximum 4*n* cross section of ^{48}Ca-, ^{44}Ca-, and ^{45}Sc-induced reactions on ^{159}Tb. The reported cross sections were measured experimentally, while σ_{capt}, P_{CN}, and $W_{sur,\,4n}$ were calculated at the indicated E^*_{CN} using the model described in Section 3.

Reaction	$\sigma_{4n,\,max}$ (μb)	E^*_{CN} (MeV)	σ_{capt} (μb)	P_{CN}	$W_{sur,\,4n}$
^{48}Ca + ^{159}Tb	12600 ± 1900	48.1	1.6 x 10^5	0.26	0.37
^{44}Ca + ^{159}Tb	230 ± 20	49.9	8.7 x 10^4	0.20	0.0069
^{45}Sc + ^{159}Tb	$2.4^{+2.3}_{-1.4}$	52.8	7.4 x 10^4	0.13	0.00014

where S_n is the neutron separation energy and B_f is the fission barrier. The survival probability can then be written to show its strong dependence on B_f and S_n [20]:

$$W_{sur} \propto \prod_{j=1}^{x} \exp\left[\left(B_f - S_n\right)/T\right]_j , \tag{4.1}$$

where x is the number of neutrons emitted and T is the nuclear temperature as calculated by Eq. (3.40). This leads to the following approximate expression for the *xn* reactions:

$$W_{sur} \propto \left\{\exp\left[\left(\overline{B_f - S_n}\right)/T\right]\right\}^x , \tag{4.2}$$

where $\overline{B_f - S_n}$ is the average value of the fission barrier minus the neutron separation energy across the entire deexcitation cascade. Values of $\overline{B_f - S_n}$ for the ^{45}Sc- and ^{44}Ca-induced reactions are reported in Table 4.6. Plots of the maximum 4*n* EvR cross sections against $\overline{B_f - S_n}$ are presented for reactions with even-*Z* projectiles in Fig. 4.10 and for reactions with ^{45}Sc projectiles in Fig. 4.11. The solid data points in Figs. 4.10 and 4.11 are the experimental EvR cross sections measured by our group. The 4*n* EvR was below the limits of experimental sensitivity for the ^{54}Cr + ^{162}Dy reaction, so comparisons were made with the ^{40}Ar + ^{176}Hf [48] and ^{124}Sn + ^{92}Zr [49] cross bombardments. Additional discussion on the ^{48}Ca-, ^{50}Ti-, and ^{54}Cr-induced reactions can be found in our publications [50, 51] and the thesis of D. A. Mayorov [73]. Two theoretical calculations for the *4n* EvR cross section are presented in both figures: the dashed line indicates the calculation *with* CELD included in the model, and the solid line indicates the theoretical calculation *without* CELD included in the model. In all calculations, the 4*n* cross section was calculated at the same initial excitation energy as the experimental data point. The

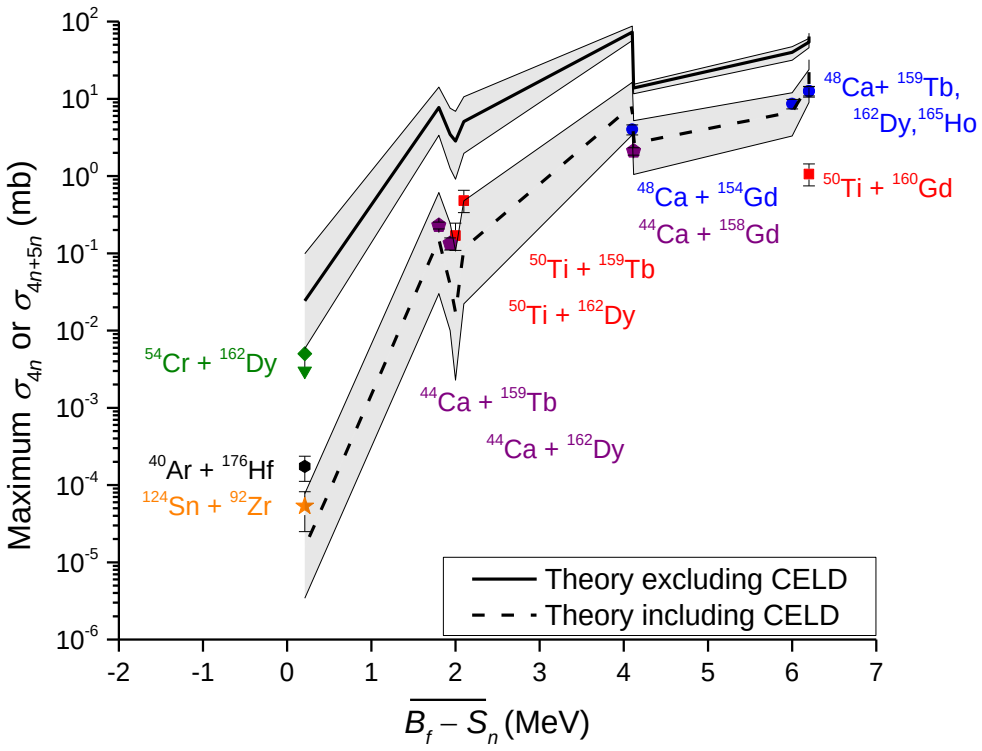

Figure 4.10. Maximum 4*n* EvR cross sections in reactions with even-*Z* projectiles (solid points) as a function of the average difference in the fission barrier and neutron separation energy across the deexcitation cascade. The dashed line is the model calculation with CELD *included*, while the solid line is the model calculation with CELD excluded. The gray shaded regions indicate the effects of changing the fission barrier by ±0.5 MeV. All reactions produce CN near the N = 126 spherical closed shell. The ^{48}Ca data were reported in [50], the ^{50}Ti and ^{54}Cr data were reported in [51], the ^{44}Ca data were discussed in this work, the ^{40}Ar data were reported in [48], and the ^{124}Sn data were reported in [49]. Only an upper limit was measured for the ^{54}Cr + ^{162}Dy reaction, so the ^{40}Ar + ^{176}Hf and ^{124}Sn + ^{92}Zr cross bombardments were considered to provide an estimate of $\sigma_{4n,\,max}$ for the ^{54}Cr-induced reaction. Figure used with permission from [123].

gray bands around the dashed and solid lines represent the effects of changing B_f by ±

0.5 MeV, which corresponds to the estimated uncertainty in B_f.

The experimental and theoretical results presented in Fig. 4.10 and Fig. 4.11 have several implications. Firstly, the importance of $\overline{B_f - S_n}$ to maximizing the EvR cross sections is shown. As the values of $\overline{B_f - S_n}$ decrease, the values of $\sigma_{max,\,4n}$ decrease as well. This is especially evident in Fig 4.10 as $\overline{B_f - S_n}$ drops from ≈ 2 MeV (the ^{44}Ca, ^{50}Ti + ^{159}Tb, ^{162}Dy reactions) to ≈ 0 MeV (the ^{54}Cr + ^{162}Dy reaction). The corresponding values of $\sigma_{max,\,4n}$ decrease by three orders of magnitude from ≈ 100 μb to ≈ 0.1 μb. When considering the ^{45}Sc-induced reactions in Fig. 4.11, the values of $\sigma_{max,\,4n}$ still

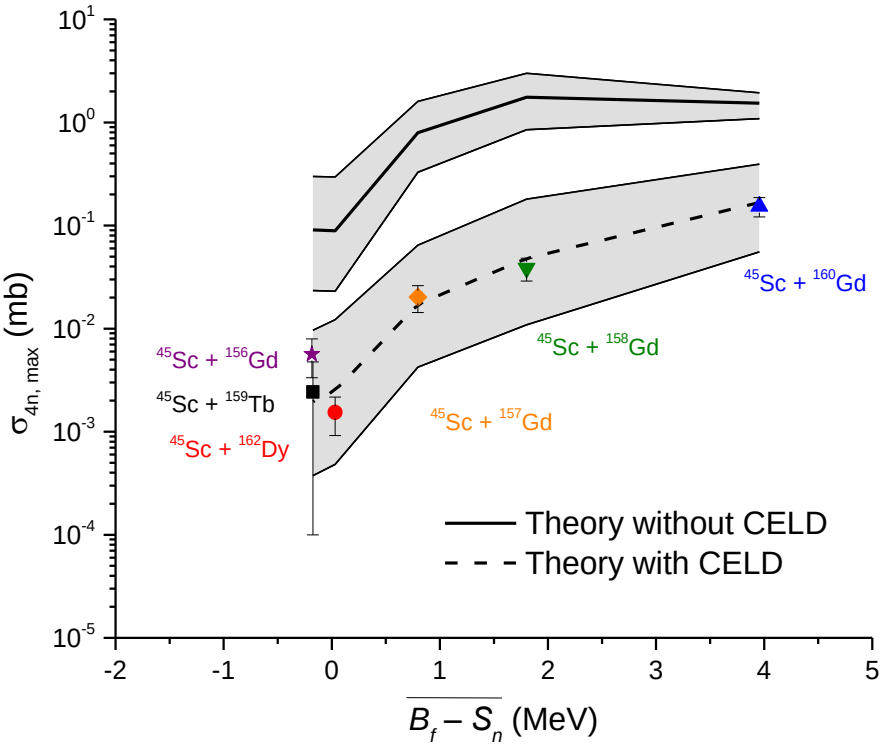

Figure 4.11. Same as Fig. 4.6, except for reactions with ^{45}Sc projectiles. Figure used with permission from [121].

decrease, although the severity of the drop is not as sharp. As $\overline{B_f - S_n}$ decreases from ≈ 2 MeV (the ^{45}Sc + ^{158}Gd reaction) to ≈ 0 MeV (the ^{45}Sc + ^{156}Gd, ^{159}Tb, and ^{162}Dy reactions), the corresponding values of $\sigma_{max,\,4n}$ only decrease from ≈ 40 μb to ≈ 5 μb.

The second main conclusion from Figs. 4.10 and 4.11 is that the data best fits the model when CELD is included. As discussed in Section 1.4.2, the reactions studied in this dissertation were good candidates to study CELD because the CN were shell-stabilized, spherical nuclei. As fission occurs, many rotational levels were introduced, and the fission probability was thus enhanced. The model calculations with CELD included (dashed lines) fit the data better than calculations where CELD is not included (solid lines). This is true across all values of $\overline{B_f - S_n}$ for all the projectiles which were studied in this work. This interpretation was consistent with the previous work described in Section 1.4.2 which discussed the influence of CELD on reaction products near the N = 126 shell.

Interestingly, the same theoretical model (with a small variation in P_{CN}) that was used in this work was described in [64] for the ^{16}O + ^{208}Pb and ^{12}C + ^{236}U reactions, and it was found that CELD was *not* necessary to reproduce the experimental data. The CN for the two reactions, ^{224}Th and ^{248}Cf, produced deformed CN which are not close to a closed shell. Due to the large ground state deformations of these CN, CELD was expected to have a smaller effect for those reactions than the ones studied in this work. More investigation is needed into that area to clarify the situation.

The results presented in Fig. 4.10 show a very steep drop-off in $\sigma_{max,\,4n}$ as $\overline{B_f - S_n}$ drops from ≈ 2 MeV to ≈ 0 MeV. This is, perhaps, due to the interplay of two effects. Firstly, it has been discussed that CELD is more influential for spherical, shell-corrected CN. However, at large values of $\overline{B_f - S_n}$, neutron emission dominates fission because $\Gamma_n >> \Gamma_f$. CELD still enhances fission in this region, as evidenced by the fact that the fission enhancement factor, $K_{coll,\,f}$, is larger than the particle emission enhancement factor, $K_{coll,\,i}$, for all the reactions studied in this work. For example, typical values of $K_{coll,\,f}$ and $K_{coll,\,i}$ for the ^{44}Ca + ^{158}Gd reaction are 80 and 10 (unitless), respectively. However, the overall effect of CELD is weak because neutron emission is still dominant when $K_{coll,\,i}\Gamma_n >> K_{coll,\,f}\Gamma_f$. This is illustrated in Fig. 4.10, where the difference in the theoretical calculations with and without CELD is only one order of magnitude. For small values of $\overline{B_f - S_n}$, neutron emission is no longer the dominant process, and, generally speaking, $\Gamma_n \approx \Gamma_f$. The inclusion of CELD in these reaction systems makes $K_{coll,\,i}\Gamma_n < K_{coll,\,f}\Gamma_f$, and CELD has a stronger effect in this range of $\overline{B_f - S_n}$. In Fig. 4.10, there is a three order-of-magnitude difference in the theoretical calculations with and without CELD at $\overline{B_f - S_n} \approx 0$ MeV.

The final interesting observation from Figs. 4.10 and 4.11 is that the decrease of $\sigma_{max,\,4n}$ with $\overline{B_f - S_n}$ is much more severe for the reactions with even-*Z* projectiles than the reactions with the ^{45}Sc projectiles. Maximum 4*n* cross sections for selected reactions at three different values of $\overline{B_f - S_n}$ are presented in Table 4.9 and in Fig. 4.12. At large

values of $\overline{B_f - S_n}$, the reactions with even-*Z* projectiles clearly have larger maximum 4*n* cross sections and total EvR cross sections than the ^{45}Sc-induced reactions. Interestingly, this is reversed at small values of $\overline{B_f - S_n}$; the ^{45}Sc-induced reactions have larger maximum 4*n* cross sections at $\overline{B_f - S_n} \approx 0$. For the three reactions at $\overline{B_f - S_n} \approx 0$, the reactions with even-*Z* projectiles produced CN directly on the *N* = 126 closed shell, whereas the ^{45}Sc + ^{159}Tb reaction produces a CN with *N* = 118. The ^{204}Rn CN is still

Table 4.9. Maximum 4*n* cross sections and sum EvR cross sections for groups of reactions with similar values of $\overline{B_f - S_n}$. The ^{48}Ca data were taken from [50], the ^{44}Ca and ^{45}Sc data were presented in this dissertation, the ^{40}Ar data were taken from [48], and the ^{124}Sn data were taken from [49]. The sum EvR cross sections were determined at the same energy as $\sigma_{4n,\,max}$.

Reaction	$\overline{B_f - S_n}$ (MeV)	$\sigma_{4n,\,max}$ (μb)	$\Sigma\sigma_{EvR}(E^*)$ (μb)
^{48}Ca + ^{154}Gd	4.11	4000 ± 600	6400
^{44}Ca + ^{158}Gd	4.11	2100 ± 230	4500
^{45}Sc + ^{160}Gd	3.96	150 ± 20	230
^{50}Ti + ^{159}Tb	2.08	481^{+173}_{-144}	710
^{44}Ca + ^{159}Tb	1.80	230 ± 20	510
^{45}Sc + ^{158}Gd	1.80	39 ± 7	73
^{45}Sc + ^{159}Tb	-0.17	$2.4^{+2.3}_{-1.4}$	44
^{40}Ar + ^{176}Hf	0.21	0.17 ± 0.06	9.1
^{124}Sn + ^{92}Zr[a]	0.21	0.0534 ± 0.0284	0.59

[a]A sum of the 4*n* and 5*n* cross sections was reported for the ^{124}Sn + ^{92}Zr reaction.

considered to be spherical ($\beta_2 < 0.15$), but as the CN emits neutrons, the *4n* EvR is far enough away from the $N = 126$ shell to be deformed ($\beta_2 > 0.15$). Thus, the effects of CELD would be expected to be stronger for the reactions with even-*Z* projectiles, and this is perhaps why the dropoff in $\sigma_{max,\,4n}$ is larger for those reactions. More research is needed to clarify this situation.

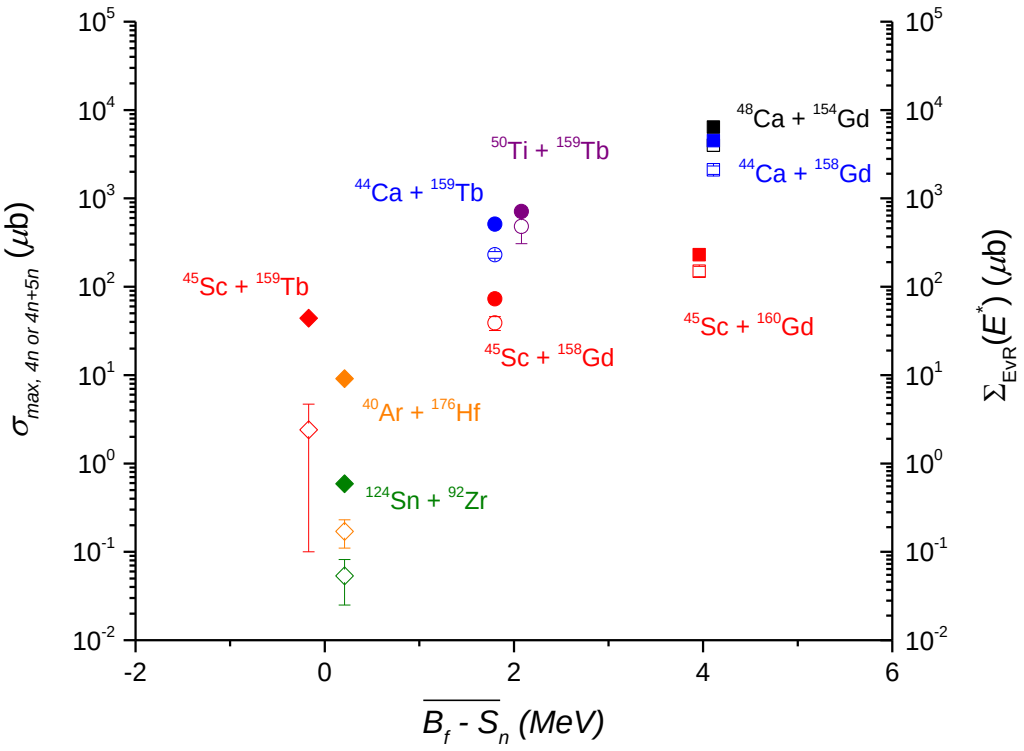

Figure 4.12. Plots of the maximum 4*n* cross sections (open points with error bars) and the sum cross sections (solid points) for the three sets of reactions in Table 4.10. All the ^{45}Sc-induced reactions are in red, the ^{44}Ca-induced reactions are in blue, and other reactions have their own individual color. The ^{45}Sc cross sections are clearly below the reactions induced by even-Z projectiles at $\overline{B_f - S_n} \approx 4$ MeV. At $\overline{B_f - S_n} \approx 0$ MeV, the ^{45}Sc reaction has larger cross sections. This is perhaps because the ^{45}Sc-induced reactions farther away from the shell and the effect of CELD is weaker for these reactions. See main text for discussion.

4.4.4 Implications for Superheavy Element Synthesis

The results described in this section have several implications for the synthesis of superheavy elements (SHEs). The prospects for the use of ^{45}Sc as a projectile to synthesize new SHEs or new isotopes of existing SHEs are very bleak. For the reactions studied in this work, the large reduction in W_{sur} due to the neutron-deficiency of ^{45}Sc led to a four order-of-magnitude reduction in the 4*n* cross sections as compared to ^{48}Ca-induced reactions on the same targets. The magnitude of the cross section reduction when using ^{45}Sc instead of ^{48}Ca to produce SHEs is unknown because the experiments have not been done. However, we can say with confidence that the ^{45}Sc-induced, SHE-producing reactions would have smaller cross sections than those produced in the ^{48}Ca-induced reactions and that the difference is likely several orders of magnitude. The cross sections with ^{48}Ca projectiles are single picobarns, the use of ^{45}Sc as a projectile is simply not feasible unless the beam intensity (as compared to current intensities of ^{48}Ca) were increased by several orders of magnitude (see [10] and references therein for a discussion about SHEs). Not even the Superheavy Element Factory being constructed in Dubna, Russia will able to deliver such beam intensity to produce very-neutron-deficient isotopes of SHEs in reactions with ^{45}Sc projectiles. Additionally, the scientific interest in doing such an experiment is likely low; there are other projectiles which could be used for the same purpose and would produce new isotopes of SHEs with larger cross sections (such as ^{44}Ca). There is a theoretical calculation which suggests that reactions with ^{45}Sc projectiles may have similar EvR cross sections to those in the ^{48}Ca-induced

reactions [127]; however, these experimental data and other theoretical calculations [128] strongly suggest that this would not be the case.

The influence of CELD may bode ill for the SHE region of the chart of the nuclides. The island of stability may be centered on the $N = 184$ spherical closed shell, and the region is expected to contain spherical, shell-stabilized nuclei. As in the reactions near the $N = 126$ spherical closed shell which were studied in this work, the EvR cross sections for these SHEs may not be enhanced due to CELD. One important point to note is that the fission saddle point occurs at much smaller values of β_2 for SHEs than for the nuclei studied in this work. This means that less of a deformation is required to fission, and this possibly could weaken the overall effect of CELD for SHEs. Our results indicate that CELD will influence the production of SHEs; making a quantitative statement, however, is still difficult at this time.

To connect this to the background research described in the introductory section of this dissertation, Vermeulen *et al.* found that fusion-evaporation cross sections near the $N = 126$ spherical closed shell were not enhanced due to the presence of the spherical closed shell [48]. The lack of shell stabilization was supported in Ref. [49], while other authors proposed that the fission barrier for neutron-deficient nuclei was too large [52]. In all cases, the presence of the shell closure did not enhance the fusion-evaporation cross sections. The experimental and theoretical results presented in this dissertation also show that the shell closure does not enhance fusion-evaporation cross sections, most likely because CELD enhances the fission probability for these spherical nuclei

produced in these reactions. All cases suggest that the production of SHEs near the N = 184 spherical closed shell will not be enhanced.

At the time of this writing, five reactions have been used in attempts to synthesize elements with Z > 118. These reactions were, in order of oldest to most recent: ^{58}Fe + ^{244}Pu [129], ^{64}Ni + ^{238}U [130], ^{54}Cr + ^{248}Cm [131], ^{50}Ti + ^{249}Cf [132], and ^{50}Ti + ^{249}Bk [132]. The products were expected to have shell corrections of ~ 7 MeV. Only upper limits have been measured thus far in the reactions listed above, and the most sensitive experiment reported an upper limit of 90 fb [130]. There is no evidence so far of any extra stabilization due to the shell closures, but only the discovery of these elements and measurement of the cross sections will provide definitive evidence of the effects of the shell closures.

5. CONCLUSIONS AND FUTURE WORK

5.1 Conclusions

The production of spherical, shell-stabilized evaporation residues in ^{45}Sc- and ^{44}Ca-induced reactions was studied at the Cyclotron Institute at Texas A&M University using the K500 cyclotron and MARS. The products were identified via their characteristic α-decay energies. A wide variety of exit channels were observed, and complete 4*n* excitation functions were measured for the ^{45}Sc + $^{156\text{-}158,\,160}$Gd, ^{159}Tb, and ^{162}Dy reactions and the ^{44}Ca + ^{158}Gd, ^{159}Tb, ^{162}Dy reactions. The largest observed 4*n* cross section was 2100 ± 230 μb in the ^{44}Ca + ^{158}Gd reaction, and the smallest "peak" 4*n* cross section was 1.8 ± 0.6 μb in the ^{45}Sc + ^{162}Dy reaction. The *p*3*n* exit channel was commonly observed; the largest observed *p*3*n* cross section was 220^{+60}_{-50} μb in the ^{44}Ca + ^{159}Tb reaction and the smallest "peak" *p*3*n* cross section was 10 ± 2 μb in the ^{45}Sc + ^{162}Dy reaction. The cross sections were compared to ^{48}Ca-induced reactions on the same targets, and it was observed that the cross sections with ^{45}Sc projectiles were three to four orders of magnitude smaller than the cross sections with ^{48}Ca projectiles.

A theoretical model was developed and used to draw several main conclusions from the data:

i. The model of $\sigma_{fus} = \sigma_{capt} P_{CN}$ is accurately reproducing the experimental data.

ii. The survival probability is the main factor in determining the EvR cross sections.

iii. CELD reduces the survival probability for EvRs produced near the N = 126 shell and will be an important phenomenon to consider for SHEs produced near the N = 184 shell.

iv. The ^{45}Sc cross sections decrease more slowly as $\overline{B_f - S_n}$ decreases than in the even-Z-projectile reactions, perhaps because the CN are farther away from the shell (more deformed) and CELD has a weaker effect.

v. The neutron content of the reaction system should absolutely be maximized in order to maximize $\overline{B_f - S_n}$ and maximize the cross sections for the production of the next SHEs.

The first main conclusion is that the model does a good job of calculating the fusion cross sections. There is a large uncertainty associated with P_{CN}, but the two cross bombardment pairs tested how well the model calculated $\sigma_{fus} = \sigma_{capt}P_{CN}$. Fig. 4.9 and the surrounding discussion show that the model reproduces the data well.

The second main conclusion is that the survival probability is the dominant factor in determining the EvR cross sections. The evidence for this conclusion lies in the comparison between the ^{45}Sc- and ^{48}Ca-induced reactions on the same targets. Fig. 4.8 shows comparisons of the fusion cross sections for the ^{48}Ca, ^{45}Sc + ^{159}Tb reactions. The

fusion cross section accounts for approximately one order of magnitude difference, while the remaining three orders of magnitude come from the survival probability. Additionally, Table 4.8 shows calculations for each of the three stages of EvR formation for three reactions on the ^{159}Tb target, and W_{sur} is shown to be the dominant factor.

The third main conclusion is that CELD reduced the EvR cross sections for the reactions which produce CN near the N = 126 spherical closed shell. Fig. 4.10 and 4.11 show the maximum 4n cross sections for the even-Z reactions and ^{45}Sc-induced reactions as a function of $\overline{B_f - S_n}$. In both cases, the calculations with CELD included fit the data better than the calculations without CELD. Thus, CELD is expected to affect the production of SHEs near the N = 184 spherical closed shell. However, the strength of the CELD effect in this region is a question for debate.

The fourth main conclusion is that the CELD effect might be weaker for the ^{45}Sc-induced reactions because they produce CN farther from the N = 126 spherical shell closure. This can be seen in Fig. 4.11, Fig. 4.12, and Table 4.10, where the decrease in $\sigma_{max,\,4n}$ as $\overline{B_f - S_n}$ decreases is weaker for the ^{45}Sc-induced reactions.

The fifth main conclusion that can be drawn from the data and the model is that maximizing the neutron content is critical to maximizing the EvR production cross sections. This follows from the first conclusion that the survival probability is the most important factor in determining EvR cross sections. As shown in Fig 4.10 and Fig. 4.11, the EvR cross section depends on the difference in the fission barrier and the neutron binding energy. This can also be gleaned from Table 4.8 and Table 4.12. In order to maximize the survival probability, the neutron binding energy should be minimized and

the fission barrier should be maximized. To accomplish this, the CN should be as neutron-rich as possible. This is the main reason why ^{48}Ca has been so successful as a projectile for synthesizing SHEs. This is also why ^{45}Sc would be a poor projectile for synthesizing SHEs. The neutron deficiency of ^{45}Sc leads to higher neutron binding energies and lower fission barriers, both of which result in smaller survival probabilities.

5.2 Future Work

Although the present reaction studies have led to useful conclusions about the fusion-evaporation reaction mechanism, there are other reaction systems which could help increase our knowledge. Studying ^{44}Ca-induced reactions on multiple isotopes of Gd (similar to the series of ^{45}Sc reactions on Gd targets) will again help study the effects of the relative neutron content of the reaction system on the EvR cross sections. The 4*n* EvR cross section of the ^{44}Ca + ^{154}Gd reaction ($\overline{B_f - S_n}$ = 0.15 MeV) in particular could be very interesting to compare with the other even-*Z* and the ^{45}Sc 4*n* cross sections at similar values of $\overline{B_f - S_n}$. Additionally, it would be interesting if *pxn* exit channels are observed from the ^{44}Ca-induced reactions on the more neutron-deficient isotopes of Gd. These reactions produce nuclei which are still approximately spherical and are good candidates of observing the influence of CELD.

The future installation of the AGGIE gas-filled separator (formerly named SASSYER at Yale University [133]) and larger beam intensities from the recommissioned K150 cyclotron will lead to an increase in experimental sensitivity of at

least a factor of 10. This will allow us to study reactions with lower cross sections, and the ^{45}Sc + ^{154}Gd reaction would be an interesting extension of the ^{45}Sc + Gd series studied in this work. The CN (^{199}At, N = 114) is 12 neutrons away from the N = 126 closed shell, and the 4n EvR has $\overline{B_f - S_n}$ = -1.81 MeV, which would be the lowest that we have studied. The CN is still considered to be spherical (β_2 = 0.08), but every nucleus in the deexcitation cascade is deformed (β_2 < -0.15). If the cross sections in the ^{45}Sc + ^{154}Gd reaction follow the trend of the ^{45}Sc-induced reactions in Fig. 4.12, it would indeed be a very interesting result. The data combined with the model analysis would give insight into how important CELD is for a reaction system which produces deformed EvRs in this region.

Finally, some improvements in the theoretical calculations could help shed better insight into the experimental results. As discussed, the *pxn* cross sections are not well reproduced, potentially due to an uncertainty in B_p. However, improving this aspect of the model will be extremely challenging unless very particular measurements are made and published. The fission barrier is an extremely important quantity in the calculations, and the ±0.5 MeV error in B_f is not negligible to the interpretation of the results. If B_f is over predicted for neutron-deficient heavy nuclei, such as suggested in [52], then the interpretation of the influence of CELD may change. More accurate knowledge of B_f is key. Finally, the order-of-magnitude uncertainty in P_{CN} is always a worrisome effect. The cross bombardments in Fig. 4.9 tested the model of σ_{capt} and P_{CN} with good results; however, these are still purely theoretical calculations. As more neutron-deficient reactions with lower cross sections are studied by our research group, it is quite possible

that the error in the P_{CN} calculation would increase. The scaling factor, ζ, in Eq. (3.16) was determined by an experimental fit to P_{CN} data from ^{48}Ca-induced reactions, and its accuracy will likely decrease for reactions which produced CN farther from stability. The behavior of P_{CN} as the relative neutron-richness changes is also a subject of current research (see [134] and references therein). Having cross bombardments in the experimental data is thus desirable when reasonably achievable. There are still many interesting topics in the field of low-energy heavy-ion-induced nuclear reactions, and the topics discussed here are on the cutting edge of modern research. The future is bright for the study of fusion-evaporation reactions!

REFERENCES

[1] C. L. Jiang, K. E. Rehm, R. V. F. Janssens, H. Esbensen, I. Ahmad, B. B. Back, P. Collon, C. N. Davids, J. P. Greene, D. J. Henderson, G. Mukherjee, R. C. Pardo, M. Paul, T. O. Pennington, D. Seweryniak, S. Sinha, and Z. Zhou, *Influence of nuclear structure on sub-barrier hindrance in Ni+Ni fusion*, Phys. Rev. Lett. **93**, 012701 (2004).

[2] D. J. Hinde, D. Hilscher, H. Rossner, and B. Gebauer, *Neutron emission as a probe of fusion-fission and quasifission dynamics*, Phys. Rev. C **45**, 1229 (1992).

[3] G. N. Knyazheva, E. M. Kozulin, R. N. Sagaidak, A. Y. Chizhov, M. G. Itkis, N. A. Kondratiev, V. M. Voskressensky, A. M. Stefanini, B. R. Behera, L. Corradi, E. Fioretto, A. Gadea, A. Latina, S. Szilner, M. Trotta, S. Beghini, G. Montagnoli, F. Scarlassara, F. Haas, N. Rowley, P. R. S. Gomes, and A. S. deToledo, *Quasifission processes in $^{40,48}Ca+^{144,154}Sm$ reactions*, Phys. Rev. C **75**, 064602 (2007).

[4] J. Panqueva, H. P. Hellmeister, L. Lühmann, F. J. Bergmeister, K. P. Lieb, and T. Otsuka, *Nuclear structure studies of high-spin states in ^{79}Rb and ^{79}Kr*, Nucl. Phys. A **389**, 424 (1982).

[5] J. J. Gaardhøje, *Nuclear structure at high excitation energy studied with giant resonances*, Ann. Rev. Nucl. Part. Sci. **42**, 483 (1992).

[6] International Atomic Energy Agency, *Cyclotron produced radionuclides: physical characteristics and production methods*, in Technical Reports Series (2009) (unpublished).

[7] A. Yakushev, J. M. Gates, A. Türler, M. Schädel, C. E. Düllmann, D. Ackermann, L.-L. Andersson, M. Block, W. Brüchle, J. Dvorak, K. Eberhardt, H. G. Essel, J. Even, U. Forsberg, A. Gorshkov, R. Graeger, K. E. Gregorich, W. Hartmann, R.-D. Herzberg, F. P. Heßberger, D. Hild, A. Hübner, E. Jäger, J. Khuyagbaatar, B. Kindler, J. V. Kratz, J. Krier, N. Kurz, B. Lommel, L. J. Niewisch, H. Nitsche, J. Omtvedt, E. Parr, Z. Qin, D. Rudolph, J. Runke, B. Schausten, E. Schimpf, A. Semchenkov, J. Steiner, P. Thörle-Pospiech, J. Uusitalo, M. Wegrzecki, and N. Wiehl, *Superheavy element flerovium (Element 114) is a volatile metal*, Inorganic Chemistry **53**, 1624 (2014).

[8] A. Ghiorso, B. G. Harvey, G. R. Choppin, and S. G. Thompson, *New element mendelevium, atomic number 101*, Physical Review **98**, 1518 (1955).

[9] Y. Oganessian, V. Utyonkov, Y. Lobanov, F. Abdullin, A. Polyakov, R. Sagaidak, I. Shirokovsky, Y. Tsyganov, A. Voinov, G. Gulbekian, S. Bogomolov, B. Gikal, A. Mezentsev, S. Iliev, V. Subbotin, A. Sukhov, K. Subotic, V. Zagrebaev, G. Vostokin, M. Itkis, K. Moody, J. Patin, D. Shaughnessy, M. Stoyer, N. Stoyer, P. Wilk, J. Kenneally, J. Landrum, J. Wild, and R. Lougheed, *Synthesis of the isotopes of elements 118 and 116 in the ^{249}Cf and $^{245}Cm+^{48}Ca$ fusion reactions*, Phys. Rev. C **74**, 044602 (2006).

[10] J. H. Hamilton, S. Hofmann, and Y. T. Oganessian, *Search for superheavy nuclei*, Ann. Rev. Nucl. Part. Sci. **63**, 383 (2013).

[11] M. Thoennessen, *Current status and future potential of nuclide discoveries*, Rep. Prog. Phys. **76**, 1 (2013).

[12] K. Morita, K. Morimoto, D. Kaji, T. Akiyama, S. Goto, H. Haba, E. Ideguchi, R. Kanungo, K. Katori, H. Koura, K. Kudo, T. Ohnishi, A. Ozawa, T. Suda, K. Sueki, H. Xu, T. Yamaguchi, A. Yoneda, A. Yoshida, and Y. Zhao, *Experiment on the synthesis of element 113 in the reaction $^{209}Bi(^{70}Zn, n)^{278}113$*, J. Phys. Soc. Jpn. **73**, 2593 (2004).

[13] K. Morita, K. Morimoto, D. Kaji, T. Akiyama, S. Goto, H. Haba, E. Ideguchi, K. Katori, H. Koura, H. Kikunaga, K. Kudo, T. Ohnishi, A. Ozawa, N. Sato, T. Suda, K. Sueki, F. Tokanai, T. Yamaguchi, A. Yoneda, and A. Yoshida, *Observation of second decay chain from $^{278}113$*, J. Phys. Soc. Jpn. **76**, 045001 (2007).

[14] D. C. Hoffman, F. O. Lawrence, J. L. Mewherter, and F. M. Rourke, *Detection of plutonium-244 in nature*, Nature (London) **234**, 132 (1971).

[15] E. K. Hulet, J. F. Wild, R. W. Lougheed, J. E. Evans, B. J. Qualheim, M. Nurmia, and A. Ghiorso, *Spontaneous-fission half-life of ^{258}Fm and nuclear instability*, Phys. Rev. Lett. **26**, 523 (1971).

[16] K. Morita, K. Morimoto, D. Kaji, H. Haba, K. Ozeki, Y. Kudou, T. Sumita, Y. Wakabayashi, A. Yoneda, K. Tanaka, S. Yamaki, R. Sakai, T. Akiyama, S.-i. Goto, H. Hasebe, M. Huang, T. Huang, E. Ideguchi, Y. Kasamatsu, K. Katori, Y. Kariya, H. Kikunaga, H. Koura, H. Kudo, A. Mashiko, K. Mayama, S.-i. Mitsuoka, T. Moriya, M. Murakami, H. Murayama, S. Namai, A. Ozawa, N. Sato, K. Sueki, M. Takeyama, F. Tokanai, T. Yamaguchi, and A. Yoshida, *New result in the production and decay of an isotope, $^{278}113$, of the 113th element*, J. Phys. Soc. Jpn. **81**, 103201 (2012).

[17] Lawrence Berkeley National Laboratory, *Periodic table of the elements* (2016); available at http://education.lbl.gov/assets/img/home/PeriodicTable.pdf.

[18] S. Hofmann, *New elements - approaching Z = 114*, Rep. Prog. Phys. **61**, 639 (1998).

[19] S. Hofmann, *Synthesis of superheavy elements by cold fusion*, Radiochimica Acta **99**, 405 (2011).

[20] Y. T. Oganessian and V. K. Utyonkov, *Super-heavy element research*, Rep. Prog. Phys. **78**, 036301 (2015).

[21] R. Eichler, N. V. Aksenov, A. V. Belozerov, G. A. Bozhikov, V. I. Chepigin, S. N. Dmitriev, R. Dressler, H. W. Gäggeler, V. A. Gorshkov, F. Haenssler, M. G. Itkis, A. Laube, Y. V. Lebedev, O. N. Malyshev, Y. Oganessian, O. V. Petrushkin, D. Piguet, P. Rasmussen, S. V. Shishkin, A. V. Shutov, A. I. Svirikhin, E. E. Tereshatov, G. K. Vostokin, M. Wegrzecki, and A. V. Yeremin, *Chemical characterization of element 112*, Nature (London) **447**, 72 (2007).

[22] R. Eichler, N. V. Aksenov, Y. V. Albin, A. V. Belozerov, G. A. Bozhikov, V. I. Chepigin, S. N. Dmitriev, R. Dressler, H. W. Gäggeler, V. A. Gorshkov, and G. S. Henderson, *Indication for a volatile element 114*, Radiochimica Acta **98**, 133 (2010).

[23] J. Even, A. Yakushev, C. E. Dullmann, H. Haba, M. Asai, T. K. Sato, H. Brand, D. A. Nitto, R. Eichler, F. L. Fan, W. Hartmann, M. Huang, E. Jager, D. Kaji, J. Kanaya, Y. Kaneya, J. Khuyagbaatar, B. Kindler, J. V. Kratz, J. Krier, Y. Kudou, N. Kurz, B. Lommel, S. Miyashita, K. Morimoto, K. Morita, M. Murakami, Y. Nagame, H. Nitsche, K. Ooe, Z. Qin, M. Schadel, J. Steiner, T. Sumita, M. Takeyama, K. Tanaka, A. Toyoshima, K. Tsukada, A. Turler, I. Usoltsev, Y. Wakabayashi, Y. Wang, N. Wiehl, and S. Yamaki, *Synthesis and detection of a seaborgium carbonyl complex*, Science **345**, 1491 (2014).

[24] A. Türler and V. Pershina, *Advances in the production and chemistry of the heaviest elements*, Chemical Reviews **113**, 1237 (2013).

[25] O. Kester, D. Bazin, and C. Benatti, *The MSU/NSCL re-accelerator ReA3*, Proceedings of the Linear Accelerator Conference LINAC2010 **MO203**, 26 (2009).

[26] K. Hagino, N. Rowley, and A. T. Kruppa, *A program for coupled-channels calculations with all order couplings for heavy-ion fusion reactions*, Comp. Phys. Commun. **123**, 143 (1999).

[27] W. Świątecki, K. Siwek-Wilczyńska, and J. Wilczyński, *Fusion by diffusion. II. Synthesis of transfermium elements in cold fusion reactions*, Phys. Rev. C **71**, 014602 (2005).

[28] W. Loveland, *Synthetic paths to the heaviest elements*, J. Phys: Conf. Ser. **420**, 12004 (2013).

[29] National Nuclear Data Center, *Chart of the nuclides* (2016); available at http://www.nndc.bnl.gov/chart/.

[30] M. Schädel, *The chemistry of superheavy elements*, Acta Physica Polonica B **34**, 1701 (2003).

[31] C. F. v. Weizsäcker, *Zur theorie der kernmassen*, Zeitschrift für Physik **96**, 431 (1935).

[32] W. Loveland, D. J. Morrissey, and G. T. Seaborg, *Modern Nuclear Chemistry* (John Wiley & Sons, Inc., Hoboken, New Jersey, 2006).

[33] Z. Patyk and A. Sobiczewski, *Ground-state properties of the heaviest nuclei analyzed in a multidimensional deformation space*, Nucl. Phys. A **533**, 132 (1991).

[34] M. G. Mayer, *Nuclear configurations in the spin-orbit coupling model. I. Empirical evidence*, Physical Review **78**, 16 (1950).

[35] M. G. Mayer, *Nuclear configurations in the spin-orbit coupling model. II. Theoretical considerations*, Physical Review **78**, 22 (1950).

[36] S. G. Nilsson, *Binding states of individual nucleons in strongly deformed nuclei*, Dan. Vid. Selsk. Mat. Fys. **29**, 1 (1955).

[37] W. D. Myers and W. J. Swiatecki, *Anomalies in nuclear masses*, Arkiv for Fysik **36**, 343 (1967).

[38] V. M. Strutinsky, *Shell effects in nuclear masses and deformation energies*, Nucl. Phys. A **95**, 420 (1967).

[39] V. M. Strutinsky, *"Shells" in deformed nuclei*, Nucl. Phys. A **122**, 1 (1968).

[40] P. Möller, J. R. Nix, W. D. Myers, and W. Świątecki, *Nuclear ground-state masses and deformations*, At. Data Nucl. Data Tables **59**, 185 (1995).

[41] N. Bohr, *Neutron capture and nuclear constitution*, Nature (London) **137**, 344 (1936).

[42] M. Beckerman, *Sub-barrier fusion of two nuclei*, Rep. Prog. Phys. **51**, 1047 (1988).

[43] Y. V. Denisov, *Nucleus-nucleus potential with shell-correction contribution and deep sub-barrier fusion of heavy nuclei*, Phys. Rev. C **89**, 044604 (2014).

[44] G. Montagnoli, A. M. Stefanini, L. Corradi, S. Courtin, E. Fioretto, F. Haas, D. Lebhertz, F. Scarlassara, R. Silvestri, and S. Szilner, *Sub-barrier fusion of $^{36}S + ^{64}Ni$ and other medium-light systems*, Phys. Rev. C **82**, 064609 (2010).

[45] R. Yanez, W. Loveland, J. Barrett, L. Yao, B. Back, S. Zhu, and T. Khoo, *Measurement of the fusion probability, P_{CN}, for hot fusion reactions*, Phys. Rev. C **88**, 014606 (2013).

[46] E. Williams, D. J. Hinde, M. Dasgupta, R. d. Rietz, I. P. Carter, M. Evers, D. H. Luong, S. D. McNeil, D. C. Rafferty, K. Ramachandran, and A. Wakhle, *Evolution of signatures of quasifission in reactions forming curium*, Phys. Rev. C **88**, 034611 (2013).

[47] R. Yanez, W. Loveland, L. Yao, J. S. Barrett, S. Zhu, B. B. Back, T. L. Khoo, M. Alcorta, and M. Albers, *Measurement of the survival probabilities for hot fusion reactions*, Phys. Rev. Lett. **112**, 152702 (2014).

[48] D. Vermeulen, H.-G. Clerc, C.-C. Sahm, K.-H. Schmidt, J. G. Keller, G. Munzenberg, and W. Reisdorf, *Cross sections for evaporation residue production near the N= 126 shell closure*, Z. Phys. A **318**, 157 (1984).

[49] C.-C. Sahm, H.-G. Clerc, K.-H. Schmidt, W. Reisdorf, P. Armbruster, F. P. Hessberger, J. G. Keller, G. Münzenberg, and D. Vermeulen, *Fusion probability of symmetric heavy, nuclear systems determined from evaporation-residue cross sections*, Nucl. Phys. A **441**, 316 (1985).

[50] D. A. Mayorov, T. A. Werke, M. C. Alfonso, M. E. Bennett, and C. M. Folden III, *Production cross sections of elements near the N = 126 shell*

in ^{48}Ca-induced reactions with ^{154}Gd, ^{159}Tb, ^{162}Dy, and ^{165}Ho targets, Phys. Rev. C **90**, 024602 (2014).

[51] D. A. Mayorov, T. A. Werke, M. C. Alfonso, E. E. Tereshatov, M. E. Bennett, M. M. Frey, and C. M. Folden III, *Evaporation residue excitation function measurements in ^{50}Ti- and ^{54}Cr-induced reactions with lanthanide targets*, Phys. Rev. C **92**, 054601 (2015).

[52] A. N. Andreyev, D. Ackermann, S. Antalic, I. G. Darby, S. Franchoo, F. P. Hessberger, S. Hofmann, M. Huyse, P. Kuusiniemi, B. Lommel, B. Kindler, R. Mann, G. Munzenberg, R. D. Page, S. Saro, B. Sulignano, B. Streicher, K. v. d. Vel, P. V. Duppen, and D. R. Wiseman, *Cross section systematics for the lightest Bi and Po nuclei produced in complete fusion reactions with heavy ions*, Phys. Rev. C **72**, 014612 (2005).

[53] A. N. Andreyev, D. D. Bogdanov, V. I. Chepigin, A. P. Kabachenko, O. N. Malyshev, Y. A. Muzichka, Y. Oganessian, A. G. Popeko, B. I. Pustylnik, R. N. Sagaidak, G. M. Ter-Akopian, and A. V. Yeremin, *Decay widths of highly excited Ra compound nuclei*, Nucl. Phys. A **620**, 229 (1997).

[54] A. N. Andreev, D. D. Bogdanov, A. V. Eremin, A. P. Kabachenko, Y. A. Muzychka, O. A. Orlova, B. I. Pustyl'nik, G. M. Ter-Akop'yan, V. I. Chepigin, and S. Sharo, *Cross sections for production of neutron-deficient isotopes of At and Po in Ho+Ar, Tb+Ca, and Ta+Mg reactions*, Sov. J. Nucl. Phys. **52**, 412 (1990).

[55] W. Reisdorf, *Analysis of fissionability data at high excitation energies*, Z. Phys. A **300**, 227 (1981).

[56] W. Reisdorf, *HIVAP manual (*1990) (unpublished)

[57] F. Plasil, *Deexcitation of compound nuclei with high angular momenta*, Phys. Rev. C **17**, 823 (1978).

[58] A. R. Junghans, M. de Jong, H. G. Clerc, A. V. Ignatyuk, G. A. Kudyaev, and K.-H. Schmidt, *Projectile-fragment yields as a probe for the collective enhancement in the nuclear level density*, Nucl. Phys. A **629**, 635 (1998).

[59] V. I. Zagrebaev, Y. Aritomo, M. G. Itkis, Yu. Ts. Oganessian, and M. Ohta, *Synthesis of superheavy nuclei: how accurately can we describe it and calculate the cross sections?*, Phys. Rev. C **65**, 014607 (2001).

[60] K. Mahata, S. Kailas, A. Shrivastava, A. Chatterjee, A. Navin, P. Singh, S. Santra, and B. S. Tomar, *Fusion of ^{19}F with $^{188,192}Os$*, Nucl. Phys. A **720**, 209 (2003).

[61] A. Heinz, K. H. Schmidt, A. R. Junghans, P. Armbruster, J. Benlliure, C. Bockstiegel, H. G. Clerc, A. Grewe, M. de Jong, J. Muller, M. Pfutzner, S. Steinhauser, and B. Voss, *Electromagnetic-induced fission of U-238 projectile fragments, a test case for the production of spherical super-heavy nuclei*, Nucl. Phys. A **713**, 3 (2003).

[62] P. Roy, K. Banerjee, M. Gohil, C. Bhattacharya, S. Kundu, T. K. Rana, T. K. Ghosh, G. Mukherjee, R. Pandey, H. Pai, V. Srivastava, J. K. Meena, S. R. Banerjee, S. Mukhopadhyay, D. Pandit, S. Pal, and S. Bhattacharya, *Effect of collectivity on the nuclear level density*, Phys. Rev. C **88**, 031601(R) (2013).

[63] V. Singh, B. R. Behera, M. Kaur, A. Kumar, K. P. Singh, N. Madhavan, S. Nath, J. Gehlot, G. Mohanto, A. Jhingan, M. Ish, T. Varughese, J. Sadhukhan, S. Pal, S. Goyal, A. Saxena, S. Santra, and S. Kailas, *Measurement of evaporation residue excitation functions for the ^{19}F + $^{194, 196, 198}Pt$ reactions*, Phys. Rev. C **89**, 024609 (2014).

[64] K. Siwek-Wilczyńska, I. Skwira, and J. Wilczyński, *Tests of the fission-evaporation competition in the deexcitation of heavy nuclei*, Phys. Rev. C **72**, 034605 (2005).

[65] R. Sagaidak and A. Andreyev, *Fission barriers for Po nuclei produced in complete fusion reactions with heavy ions*, Phys. Rev. C **79**, 054613 (2009).

[66] A. J. Sierk, Computer Code FISROT, available at https://www-nds.iaea.org/RIPL-3/fission/fis-barrier-liquiddrop.for.

[67] S. Komarov, R. J. Charity, C. J. Chiara, W. Reviol, D. G. Sarantites, L. G. Sobotka, A. L. Caraley, M. P. Carpenter, and D. Seweryniak, *Search for the fade out of a collective enhancement of the nuclear level density*, Phys. Rev. C **75**, 064611 (2007).

[68] (!!! INVALID CITATION !!! [50, 51]).

[69] H. A. Kramers, *Brownian motion in a field of force and the diffusion model of chemical reactions*, Physica (Utrecht) **VII, no. 4**, 284 (1940).

[70] M. Sharma, P. P. Singh, D. P. Singh, A. Yadav, V. Sharma, I. Bala, R. Kumar, Unnati, B. P. Singh, and R. Prasad, *Systematic study of pre-*

equilibrium emission at low energies in ^{12}C- and ^{16}O-induced reactions, Phys. Rev. C **91**, 014603 (2015).

[71] R. W. Lougheed, J. H. Landrum, E. K. Hulet, J. F. Wild, R. J. Dougan, A. D. Dougan, H. Gäggeler, M. Schädel, K. J. Moody, K. E. Gregorich, and G. T. Seaborg, *Search for superheavy elements using the ^{48}Ca+ ^{254}Es reaction*, Phys. Rev. C **32**, 1760 (1985).

[72] V. I. Zagrebaev, *Fusion-Evaporation Codes of NRV* (2016); available at http://nrv.jinr.ru/nrv.

[73] D. A. Mayorov, Doctorate Thesis, Texas A&M University, College Station, Texas (2015).

[74] R. E. Tribble, R. H. Burch, and C. A. Gagliardi, *MARS: a momentum achromat recoil spectrometer*, Nucl. Instrum. Methods. Phys. Res., Sect. A **285**, 441 (1989).

[75] C. M. Folden III, M. C. Alfonso, D. A. Mayorov, K. R. Lawrence, A. A. Alharbi, E. Berdugo, P. J. Cammarata, A. C. Raphelt, B. T. Roeder, and T. A. Werke, *Development of the MARS separator for heavy element studies*, Nucl. Instrum. Methods. Phys. Res., Sect. A **678**, 1 (2012).

[76] V. I. Zagrebaev, *Fusion Code of NRV* (2016); available at http://nrv.jinr.ru/nrv/webnrv/fusion/.

[77] V. I. Zagrebaev, *Evaporation Code of NRV* (2016); available at http://nrv.jinr.ru/nrv/webnrv/evaporation_residue_theory/dialog.php.

[78] National Instruments, *Computer Code LABVIEW*; available at http://www.ni.com/labview/.

[79] W. Parker and R. Falk, *Molecular plating: a method for the electrolytic formation of thin inorganic films*, Nucl. Instrum. Methods **16**, 355 (1962).

[80] W. Parker, H. Bildstein, N. Getoff, H. Fischer-Colbrie, and H. Regal, *Molecular plating II: a rapid and quantitative method for the electrodeposition of the rare-earth elements*, Nucl. Instrum. Methods **26**, 61 (1964).

[81] K. Eberhardt, M. Schädel, E. Schimpf, P. Thörle, and N. Trautmann, *Preparation of targets by electrodeposition for heavy element studies*, Nucl. Instrum. Methods. Phys. Res., Sect. A **521**, 208 (2004).

[82] K. Eberhardt, W. Brüchle, C. E. Düllmann, K. E. Gregorich, W. Hartmann, A. Hübner, E. Jäger, B. Kindler, J. V. Kratz, D. Liebe, B. Lommel, H. J. Maier, M. Schädel, B. Schausten, E. Schimpf, A. Semchenkov, J. Steiner, J. Szerypo, P. Thörle, A. Türler, and A. Yakushev, *Preparation of targets for the gas-filled recoil separator TASCA by electrochemical deposition and design of the TASCA target wheel assembly*, Nucl. Instrum. Methods. Phys. Res., Sect. A **590**, 134 (2008).

[83] O. Tarasov and D. Bazin, *LISE++: Radioactive beam production with in-flight separators*, Nucl. Instrum. Methods. Phys. Res., Sect. B **266**, 4657 (2008).

[84] G. Schiwietz and P. L. Grande, *Improved charge-state formulas*, Nucl. Instrum. Methods. Phys. Res., Sect. B **175**, 125 (2001).

[85] E. Segré, *Nuclei and particles: an introduction to nuclear and subnuclear physics* (Benjamin-Cummings, Massachusetts, 1977).

[86] T. A. Werke, M. C. Alfonso, M.E. Bennett, D. A. Mayorov, and C. M. Folden III, *Improvements to the heavy elements program aimed toward reaching lower cross-sections at the Texas A&M University Cyclotron Institute*, in Progress in Research (2012) (unpublished) pp. II-52.

[87] CERN, *ROOT Data Analysis Framework*; available at https://root.cern.ch/.

[88] D. C. Radford, *RADWARE Software Package* (2015); available at http://radware.phy.ornl.gov.

[89] K.-H. Schmidt, C.-C. Sahm, K. Pielenz, and H.-G. Clerc, *Some remarks on the error analysis in the case of poor statistics*, Z. Phys. A **316**, 19 (1984).

[90] C. L. Jiang, A. M. Stefanini, H. Esbensen, K. E. Rehm, S. Almaraz-Calderon, M. L. Avila, B. B. Back, D. Bourgin, L. Corradi, S. Courtin, E. Fioretto, F. Galtarossa, A. Goasduff, F. Haas, M. M. Mazzocco, D. Montanari, G. Montagnoli, T. Mijatovic, R. Sagaidak, D. Santiago-Gonzalez, F. Scarlassara, E. E. Strano, and S. Szilner, *Fusion reactions of* $^{58,64}Ni+^{124}Sn$, Phys. Rev. C **91**, 044602 (2015).

[91] H. Esbensen and A. M. Stefanini, *Influence of multiphonon excitations and transfer on the fusion of Ca+Zr*, Phys. Rev. C **89**, 044616 (2014).

[92] G. L. Zhang, X. X. Liu, and C. J. Lin, *Systematic analysis of the effect of a positive Q-value neutron transfer in fusion reactions*, Phys. Rev. C **89**, 054602 (2014).

[93] M. Dasgupta, D. J. Hinde, N. Rowley, and A. M. Stefanini, *Measuring barriers to fusion*, Ann. Rev. Nucl. Part. Sci. **48**, 401 (1998).

[94] A. M. Stefanini, D. Ackermann, L. Corradi, D. R. Napoli, C. Petrache, P. Spolaore, P. Bednarczyk, H. Q. Zhang, S. Beghini, G. Montagnoli, L. Mueller, F. Scarlassara, G. F. Segato, F. Soramel, and N. Rowley, *Influence of complex surface vibrations on the fusion of $^{58}Ni + ^{60}Ni$*, Phys. Rev. Lett. **74**, 864 (1995).

[95] J. R. Leigh, M. Dasgupta, D. J. Hinde, J. C. Mein, C. R. Morton, R. C. Lemmon, J. P. Lestone, J. O. Newton, H. Timmers, J. X. Wei, and N. Rowley, *Barrier distributions from the fusion of oxygen ions with $^{144,148,154}Sm$ and ^{186}W*, Phys. Rev. C **52**, 3151 (1995).

[96] A. J. Pacheco, F. J. O. Niello, D. E. DiGregorio, M. di Tada, J. E. Testoni, Y. Chan, E. Chávez, S. Gazes, E. Plagnol, and R. G. Stokstad, *Capture reactions in the $^{40,48}Ca + ^{197}Au$ and $^{40,48}Ca + ^{208}Pb$ systems*, Phys. Rev. C **45**, 2861 (1992).

[97] J. Tõke, R. Bock, G. X. Dai, A. Gobbi, S. Gralla, K. D. Hildenbrand, J. Kuzminski, W. F. J. Müller, A. Olmi, H. Stelzer, B. B. Back, and S. Bjørnholm, *Quasi-fission — The mass-drift mode in heavy-ion reactions*, Nucl. Phys. A **440**, 327 (1985).

[98] B. Back, P. Fernandez, B. Glagola, D. Henderson, S. Kaufman, J. Keller, S. Sanders, F. Videbæk, T. Wang, and B. Wilkins, *Entrance-channel effects in quasifission reactions*, Phys. Rev. C **53**, 1734 (1996).

[99] F. Hanappe, M. Lefort, C. Ngô, J. Péter, and B. Tamain, *Cross section and angular distribution of products in "quasifission" reactions induced by 525-MeV ^{84}Kr ions on a ^{209}Bi target*, Phys. Rev. Lett. **32**, 738 (1974).

[100] A. C. Berriman, D. J. Hinde, M. Dasgupta, C. R. Morton, R. D. Butt, and J. O. Newton, *Unexpected inhibition of fusion in nucleus-nucleus collisions*, Nature (London) **413**, 144 (2001).

[101] J. P. Blocki, H. Feldmeier, and W. J. Swiatecki, *Dynamical hindrance to compound-nucleus formation in heavy-ion reactions*, Nucl. Phys. A **459**, 145 (1986).

[102] E. Prasad, K. M. Varier, R. G. Thomas, P. Sugathan, A. Jhingan, N. Madhavan, B. R. S. Babu, S. R., S. Kalkal, S. Appannababu, J. Gehlot, K. S. Golda, S. Nath, A. M. Vinodkumar, B. P. A. Kumar, B. V. John, G. Mohanto, M. M. Musthafa, R. Singh, A. K. Sinha, and S. Kailas, *Conclusive evidence of quasifission in reactions forming the ^{210}Rn compound nucleus*, Phys. Rev. C **81**, 054608 (2010).

[103] C. Yadav, R. G. Thomas, R. K. Choudhury, P. Sugathan, A. Jhingan, S. Appannababu, K. S. Golda, D. Singh, I. Mukul, J. Gehlot, E. Prasad, and H. J. Wollersheim, *Evidence of quasifission in asymmetric reactions forming the ^{250}Cf compound system*, Phys. Rev. C **86**, 034606 (2012).

[104] V. Zagrebaev and W. Greiner, *Synthesis of superheavy nuclei: a search for new production reactions*, Phys. Rev. C **78** (2008).

[105] V. E. Oberacker, A. S. Umar, and C. Simenel, *Dissipative dynamics in quasifission*, Phys. Rev. C **90**, 054605 (2014).

[106] K. Siwek-Wilczyńska, A. Borowiec, I. Skwira-Chalot, and J. Wilczyński, *Entrance-channel effects in suppression of fusion of heavy nuclei*, Int. J. Mod. Phys. E **17**, 12 (2008).

[107] R. N. Sagaidak, G. N. Kniajeva, I. M. Itkis, M. G. Itkis, N. A. Kondratiev, E. M. Kozulin, I. V. Pokrovsky, A. I. Svirikhin, V. M. Voskressensky, A. V. Yeremin, L. Corradi, A. Gadea, A. Latina, A. M. Stefanini, S. Szilner, M. Trotta, A. M. Vinodkumar, S. Beghini, G. Montagnoli, F. Scarlassara, D. Ackermann, F. Hanappe, N. Rowley, and L. Stuttgé, *Fusion suppression in mass-asymmetric reactions leading to Ra compound nuclei*, Phys. Rev. C **68**, 014603 (2003).

[108] J. D. Jackson, *A schematic model for (p, xn) cross sections in heavy elements*, Can. J. Phys **34**, 767 (1956).

[109] R. Vandenbosch and J. Huizenga, *Nuclear Fission* (Academic, New York, 1973).

[110] W. Świątecki, K. Siwek-Wilczyńska, and J. Wilczyński, *Ratios of disintegration rates for distinct decay modes of an excited nucleus*, Phys. Rev. C **78**, 054604 (2008).

[111] F. Plasil and R. L. Ferguson, in *Proceedings of the international symposium of physics and chemistry of fission*, Jülich, Düren (IAEA, Vienna, 1980), Vol. 1, p. 521.

[112] L. G. Moretto, *A novel approach to the evaporation of complex fragments*, Physics Letters **40B**, 185 (1972).

[113] L. G. Moretto, *Statistical emission of large fragments: a general theoretical approach*, Nucl. Phys. A **247**, 211 (1975).

[114] W. E. Parker, M. Kaplan, D. J. Moses, G. La Rana, D. Logan, R. Lacey, J. M. Alexander, D. M. de Castro Rizzo, P. DeYoung, R. J. Welberry, and J. T. Boger, *Charged-particle evaporation from hot composite nuclei: evidence over a broad Z range for distortions from cold nuclear profiles*, Phys. Rev. C **44**, 774 (1991).

[115] A. J. Sierk, *Macroscopic model of rotating nuclei*, Phys. Rev. C **33**, 2039 (1986).

[116] A. V. Ignatyuk, G. N. Smirenkin, and A. S. Tishin, *Phenomenological description of the energy dependence of the level density parameter*, Sov. J. Nucl. Phys **21**, 485 (1975).

[117] W. D. Myers and W. J. Swiatecki, *The nuclear droplet model for arbitrary shapes*, Ann. Phys. (N. Y.) **84**, 186 (1974).

[118] A. M. Stefanini, G. Montagnoli, H. Esbensen, L. Corradi, S. Courtin, E. Fioretto, A. Goasduff, J. Grebosz, F. Haas, M. Mazzocco, C. Michelagnoli, T. Mijatović, D. Montanari, G. Pasqualato, C. Parascandolo, F. Scarlassara, E. Strano, S. Szilner, and D. Torresi, *Fusion of $^{40}Ca + ^{96}Zr$ revisited: transfer couplings and hindrance far below the barrier*, Phys. Lett. B **728**, 639 (2014).

[119] G. Montagnoli, A. M. Stefanini, C. L. Jiang, H. Esbensen, L. Corradi, S. Courtin, E. Fioretto, A. Goasduff, F. Haas, A. F. Kifle, C. Michelagnoli, D. Montanari, T. Mijatović, K. E. Rehm, R. Silvestri, P. P. Singh, F. Scarlassara, S. Szilner, X. D. Tang, and C. A. Ur, *Fusion of $^{40}Ca + ^{40}Ca$ and other Ca + Ca systems near and below the barrier*, Phys. Rev. C **85**, 024607 (2012).

[120] A. V. Belozerov, M. L. Chelnokov, V. I. Chepigin, T. P. Drobina, V. A. Gorshkov, A. P. Kabachenko, O. N. Malyshev, I. M. Merkin, Y. T. Oganessian, A. G. Popeko, R. N. Sagaidak, A. I. Svirikhin, A. V. Yeremin, G. Berek, I. Brida, and Š. Šáro, *Spontaneous-fission decay properties and production cross-sections for the neutron-deficient nobelium isotopes formed in the $^{44,48}Ca + ^{204,206,208}Pb$ reactions*, Eur. Phys. J. A **16**, 447 (2003).

[121] T. A. Werke, D. A. Mayorov, M. C. Alfonso, M. E. Bennett, M. J. DeVanzo, M. M. Frey, E. E. Tereshatov, and C. M. Folden III, *Hot fusion-evaporation cross sections of ^{45}Sc-induced reactions with lanthanide targets*, Phys. Rev. C **92**, 034613 (2015).

[122] K. H. Schmidt, *A new test for random events of an exponential distribution*, Eur. Phys. J. A **8**, 141 (2000).

[123] T. A. Werke, D. A. Mayorov, M. C. Alfonso, E. E. Tereshatov, and C. M. Folden III, *Hot fusion-evaporation cross sections of ^{44}Ca-induced reactions with lanthanide targets*, Phys. Rev. C **92**, 054617 (2015).

[124] L. C. Vaz and J. M. Alexander, *Empirical and theoretical fusion barriers for ^{1}H and ^{4}He: connections to evaporation from hot nuclei*, Z. Phys. A **318**, 231 (1984).

[125] S. N. Ghoshal, *An experimental verification of the theory of compound nucleus*, Physical Review **80**, 939 (1950).

[126] M. Go and S. S. Markowitz, *Test of the independence postulate in the Bohr theory of compound-nucleus decay: ^{50}Cr* system*, Phys. Rev. C **7**, 1464 (1973).

[127] W. J. Zhao, Y. Q. Zhang, H. L. Wang, L. T. Song, and L. L. Li, *Production cross sections of the superheavy nucleus 117 based on the dinuclear system model*, Chinese Physics C **34**, 1609 (2010).

[128] M. Ohta and Y. Aritomo, *An idea for predicting the evaporation residue cross section in superheavy mass region*, Phys. Atom. Nuclei **66**, 1026 (2003).

[129] Y. Oganessian, V. Utyonkov, Y. Lobanov, F. Abdullin, A. Polyakov, R. Sagaidak, I. Shirokovsky, Y. Tsyganov, A. Voinov, A. Mezentsev, V. Subbotin, A. Sukhov, K. Subotic, V. Zagrebaev, S. Dmitriev, R. Henderson, K. Moody, J. Kenneally, J. Landrum, D. Shaughnessy, M. Stoyer, N. Stoyer, and P. Wilk, *Attempt to produce element 120 in the ^{244}Pu+^{58}Fe reaction*, Phys. Rev. C **79**, 024603 (2009).

[130] S. Hofmann, D. Ackermann, S. Antalic, V. F. Comas, S. Heinz, J. A. Heredia, F. Heßberger, J. Khuyagbaatar, B. Kindler, I. Kojouharov, M. Leino, B. Lommel, R. Mann, K. Nishio, A. G. Popeko, S. Saro, J. Uusitalo, M. Venhart, and A. Yeremin, *Probing shell effects at Z = 120 and N = 184*, GSI Scientific Report 2008 **NUSTAR-SHE-01**, 131 (2008).

[131] S. Hofmann, S. Heinz, D. Ackermann, S. Antalic, W. Barth, H. G. Burkhard, V. F. Comas, L. Dahl, K. Eberhardt, J. Gostic, R. Grzywacz, R. A. Henderson, J. A. Heredia, F. P. Heßberger, J. M. Kenneally, B. Kindler, I. Kojouharov, R. Lang, M. Leino, B. Lommel, R. Mann, J. Maurer, K. Miernik, D. Miller, K. J. Moody, G. Münzenberg, S. L. Nelson, K. Nishio, A. G. Popeko, J. B. Roberto, J. Runke, K. P. Rykaczewski, S. Saro, D. A. Shaughnessy, M. A. Stoyer, P. Thörle-Pospiech, K. Tinschert, N. Trautmann, J. Uusitalo, P. A. Wilk, and A. V. Yeremin, *Attempts for the synthesis of new elements at SHIP*, GSI Scientific Report 2011 **PHN-NUSTAR-SHE-01**, 205 (2011).

[132] J. Khuyagbaatar, A. Yakushev, C. E. Dullmann, H. Nitsche, J. Roberto, D. Ackermann, L.-L. Andersson, M. Asai, H. Brand, M. Block, D. M. Cox, M. Dasgupta, X. Derkx, A. Di Nitto, J. Dvorak, K. Eberhardt, P. A. Ellison, N. E. Esker, J. Even, M. Evers, C. Fahlander, J. H. Hamilton, D. Hinde, W. Hartmann, R.-D. Herzberg, F. Heßberger, J. Hoffmann, R. Hollinger, A. Hübner, E. Jäger, J. Jeppsson, B. Kindler, S. Klein, I. Kojouharov, J. V. Kratz, J. Krier, N. Kurz, S. Lahiri, B. Lommel, M. Maiti, K. Miernik, S. Minami, A. Mistry, C. Mokry, J. P. Omtvedt, G. Pang, P. Papadakis, I. Pysmenetska, D. Rensich, D. Rudolf, J. Runke, K. Rykaczewski, L. G. Sarmiento, M. Schadel, B. Schausten, D. Shaughnessy, A. Semchenkov, J. Steiner, P. Steinegger, P. Thorle-Pospiech, E. E. Tereshatov, T. Torres de Heidenreich, N. Trautmann, A. Turler, J. Uusitalo, D. Ward, N. Wiehl, M. Wegrzecki, and V. Yakusheva, *The superheavy element search campaigns at TASCA*, GSI Scientific Report 2012 **PHN-ENNA-EXP-01**, 131 (2012).

[133] J. J. Ressler, R. Krücken, C. W. Beausang, J. M. D'Auria, H. Amro, R. F. Casten, M. A. Caprio, G. Gürdal, C. Hutter, A. A. Hecht, D. Meyer, M. Sciacciatano, and N. V. Zamfir, *SASSYER: An old instrument for new physics at Yale*, Nucl. Instrum. Methods. Phys. Res., Sect. B **204**, 141 (2003).

[134] K. Hammerton, Z. Kohley, D. J. Hinde, M. Dasgupta, A. Wakhle, E. Williams, V. E. Oberacker, A. S. Umar, I. P. Carter, K. J. Cook, J. Greene, D. Y. Jeung, D. H. Luong, S. D. McNeil, C. S. Palshetkar, D. C. Rafferty, C. Simenel, and K. Stiefel, *Reduced quasifission competition in fusion reactions forming neutron-rich heavy elements*, Phys. Rev. C **91**, 041602(R) (2015).